Master's Thesis

Detecting Clouds in the Presence of Sunglint: An Approach Using Spectral Water Vapor Absorption

Master's Thesis at the faculty of physics,
Ludwig-Maximilians-University Munich

submitted by
Felix Simon Gödde

Munich, Germany, February 5th 2018

Supervisor:
Prof. Dr. Bernhard Mayer

Masterarbeit

Wolkenerkennung im Sunglint mit Hilfe von Wasserdampfabsorption

Masterarbeit an der Fakultät für Physik,
Ludwig-Maximilians-Universität München

vorgelegt von
Felix Simon Gödde

München, den 5. Februar 2018

Betreuer:
Prof. Dr. Bernhard Mayer

Abstract

Cloud fraction and cloud size distributions derived from measurements are crucial parameters in atmospheric research. Cloud fraction determines the influence of clouds on the energy budget, from a cloud size distribution mass and energy fluxes can be calculated. Furthermore, better knowledge about both, cloud fraction and cloud size distribution, helps to improve future climate projections, as clouds were identified as a major source of uncertainty. To derive these quantities from measurement data, it is necessary distinguish clear sky from clouds. For air and spaceborne imaging instruments this is commonly done using the contrast of bright clouds in front of a dark background. This approach fails over the ocean, when the bright reflection of sunlight on the water surface, referred to as sunglint, removes the contrast between clouds and background. To overcome this problem, a cloud detection algorithm based on water vapor absorption in the short wave infrared (SWIR) solar spectrum was developed. From the view of an air or spacecraft, SWIR radiation reflected on the ocean's surface experiences higher absorption than radiation reflected on top of a cloud, due to its longer path through the atmosphere and higher water vapor concentrations near the surface. This difference in absorption is most pronounced in the water vapor absorption band at 1125 nm and in the weak absorbing flanks of the strong absorption bands at 1375 and 1900 nm. The developed algorithm uses a least square fit of a reference transmission spectrum, calculated with radiative transfer model DISORT (conatined in libRadtran), to extract the absorption information from the measured spectrum. To assess the performance of the algorithm, it was validated against 3D radiative transfer simulations using the Monte Carlo model MYSTIC with a cloud field taken from a Large Eddy Simulation (LES) model. Furthermore, it was applied to measurement data collected by the imaging spectrometer specMACS during the NARVAL II field campaign. The algorithm showed good performance on model data. Depending on the wind speed, which determines the brightness of the sunglint, and the solar zenith angle, which influences absorption and cloud shading, the cloud fraction derived by the algorithm was 1.1 to 2.75 percentage points below the benchmark cloud fraction of 24.55%. For measurement data the algorithm also revealed good results. Additionally, the derived cloud size distribution agrees well with results from previous studies. In this thesis it could be shown for the first time, that water vapor absorption is a powerful tool to detect low clouds in sunglint contaminated data of air and spaceborne imaging spectrometers.

Contents

1 Introduction

Clouds play a crucial role in Earth's climate system (Siebesma et al., 2003). In particular, shallow cumulus clouds – especially those occurring in the trade wind region – are in the focus of recent research projects. The reasons therefore are strikingly simple. On the one hand, shallow cumulus clouds have negative net radiative effect on Earth's energy budget, which means that they cool Earth's climate. This effect originates from reflection of solar radiation back to space due to the high albedo of clouds. On the other hand, shallow cumulus clouds in the trade wind region play a key role in moisture transport towards the tropics and therefore influence deep convection in the ITCZ (Siebesma, 1998). As tropical deep convection is the major driver for the Hadley circulation, the impact of shallow cumulus convection reaches up to global scales.

To gain a better understanding of the most important processes controlling development and evolution of shallow cumulus convection in the trade wind region, the NARVAL II measurement campaign was carried out in August 2016 in the western tropical Atlantic ocean near Barbados. Remote sensing instruments such as RADAR, LIDAR and the hyperspectral imager specMACS (Ewald et al., 2016) were mounted on the DLR research aircraft HALO.

To obtain cloud statistics such as cloud fraction and a cloud size distribution, it is necessary to derive a cloud mask from the measurement data. For passive remote sensing instruments like specMACS, which measure reflected solar radiation, cloud masks are often obtained using the contrast of bright clouds in front of a dark background. At low latitudes however, the bright reflection of sunlight on the ocean's surface frequently disturbs measurements because of the high solar elevation. This reflection of solar radiation on rough water surfaces is known as sunglint. The extent and brightness of the sunglint depend on the slope of present waves and therefore on wind speed (Cox and Munk, 1954). The presence of sunglint, using the brightness contrast for cloud detection fails, because the reflectance of the ocean's surface reaches or even exceeds the one of clouds.

In this thesis an algorithm is developed to derive a cloud mask even in the presence of sunglint. The method uses the absorption by water vapor at wavelengths between 1 and 2 μm captured by the short wave infrared (SWIR) camera of the specMACS instrument. Water vapor absorption has previously been used to identify cirrus clouds in air and spaceborne measurements, because their signature in water vapor absorption bands is pronounced (Gao and Kaufman, 1995). In this work it has been shown, that the high sensitivity and the high spectral resolution of specMACS makes it possible to distinguish shallow clouds from the sunglint by their water vapor signature. The cloud mask obtained with the water vapor method is used to derive the cloud fraction and cloud size distribution for the data captured during NARVAL II.

This thesis is organized as follows: The second chapter explains the theoretical background of atmospheric radiative transfer and water vapor absorption. Additionally, common methods for cloud detection are reviewed. Chapter three characterizes the specMACS instrument as well as the developed cloud detection algorithm based on water vapor absorption. The fourth chapter shows the performance of the algorithm on model and measurement data. Chapter five summarizes the achievements of this thesis and provides an outlook of possible improvements and further applications of the developed algorithm.

2 Background

2.1 Radiative transfer

The propagation of electromagnetic radiation through a medium – referred to as radiative transfer – is a fundamental process in Earth's atmosphere. As the atmosphere itself consists of different gases, aerosols as well as water and ice clouds, the equation of radiative transfer has to be solved by complex numerical models. In the following section a short introduction is given to fundamental quantities and processes in radiative transfer, the radiative transfer equation and its simplest solution.

Information in this chapter is predominantly taken from Liou (2002) and Zdunkowski et al. (2007). Other sources are cited when appropriate.

2.1.1 Important quantities

For the physical description of radiation and its interaction with matter there are some important terms and quantities which will be defined subsequently:

- **Radiance** L : Describes the amount of incoming or outgoing radiant energy (dQ) within a time interval (dt), from or into a certain direction – given by the solid angle ($d\Omega$) – per unit area (dA):

$$L = \frac{dQ}{d\Omega\, dt \cos\theta\, dA} \tag{2.1}$$

  The cosine of the zenith angle θ accounts for cases in which dA is not perpendicular to the propagation direction of the radiation. Radiance is given in $Wm^{-2}sr^{-1}$.

- **Irradiance** E: Integrating the radiance over the half-space (2π) – either the upper or the lower hemisphere – weighted by the cosine of the zenith angle yields the energy flux of radiation per unit area. Equation 2.1 therefore reduces to

$$E = \frac{dQ}{dt\, dA} \tag{2.2}$$

  with the units of irradiance being Wm^{-2}.

- **Absorption cross section** σ_{abs}: A measure for the ability of a molecule or particle to absorb radiation. The absorption cross section can be larger than the geometrical cross section as the absorption can occur even if the photon does not directly hit the target. The SI unit is m^2, but cm^2 is also commonly used.

- **Scattering cross section** σ_{sca}: The Scattering cross section describes the ability of a particle or molecule to scatter radiation. It is analogous to the absorption cross section and has the same units.

- **Absorption coefficient** β_{abs}: This quantity is derived by multiplying the absorption cross section with the number density of absorbers n_{abs}. For instance the number of molecules in the volume considered: $\beta_{abs} = \sigma_{abs} \cdot n_{abs}$, resulting in units of m^{-1}. It describes how much radiation is absorbed when a beam of light propagates through a infinitesimally thin layer containing absorbing substances.

- **Scattering coefficient** β_{sca}: The scattering coefficient is derived analog to the absorption coefficient by multiplying the scattering cross section with the number density of the scattering agent: $\beta_{sca} = \sigma_{sca} \cdot n_{sca}$ which also yields the unit m^{-1}.

- **Extinction coefficient** β_{ext}: Adding up the scattering and absorption coefficient gives the Extinction coefficient: $\beta_{ext} = \beta_{abs} + \beta_{sca}$. Therefore it contains information about the over all attenuation of a light beam by absorbing and scattering molecules and particles.

- **Single scattering albedo** ω_0: The proportion of scattering on the total extinction: $\omega_0 = \frac{\beta_{sca}}{\beta_{ext}}$.

- **Optical thickness** τ: This quantity is generally defined as the integral of the extinction coefficient along the path of the light beam:

$$\tau = \int_a^b \beta_{ext}(s)\,\mathrm{d}s \tag{2.3}$$

  where a and b denote the start and endpoint. As β_{ext} is the sum of β_{abs} and β_{sca} one can also split up the optical thickness into absorbing and scattering parts: $\tau = \tau_{abs} + \tau_{sca}$.

- **Asymmetry parameter** g: This parameter describes the amount of radiation scattered in forward direction with respect to the total incoming radiation and therefore takes values between 0 and 1.

2.1.2 Radiative transfer equation

The equation describing the propagation of electromagnetic radiation in its full complexity was first formulated by Chandrasekhar (1950). The equation is often formulated using the single scattering albedo but in the following it is written in a more illustrative way:

$$\underbrace{\frac{dL\,(\Omega)}{ds}}_{(1)} = \underbrace{-\,\beta_{ext}\,L\,(\Omega)}_{(2)} + \underbrace{\frac{\beta_{sca}}{4\pi}\int_{4\pi} p\,(\Omega', \Omega)\,L\,(\Omega')\,\mathrm{d}\Omega'}_{(3)} + \underbrace{\beta_{abs}\,B\,(T)}_{(4)} \tag{2.4}$$

Starting on the left hand side, this equation describes the change of radiance in a light beam along the traveled path (1) is equal to the portion of the radiation leaving the beam through extinction (2), plus the radiance added by photons being scattered (3) or thermally emitted (4) into the direction of the beam.

The scattering phase function $p(\Omega', \Omega)$ denotes the probability of an approaching photon from an certain direction Ω' being scattered into the direction of the beam Ω. The incoming radiance from this direction is denoted as $L(\Omega')$. To take all photons from all directions into account it has to be integrated over the whole sphere (4π).

Term (4) consists of the absorption coefficient β_{abs} that according to Kirchoff's law, is equal to the emission coefficient. It is multiplied by the Planck function, which describes the spectral emission by a black body Planck (1901)

$$B_\lambda(T) = \frac{2hc^2}{\lambda^5} \frac{1}{e^{\frac{hc}{\lambda k T}} - 1} \tag{2.5}$$

The emitted radiance depends on the temperature T and the wavelength λ. An important property of black body radiation is isotropy, which means that the same amount of radiation is emitted in every direction. Black body radiation gives the upper limit of emitted radiance by a material of certain temperature. Materials emitting less radiation than a black body are referred to as gray bodies. Integrating Planck's law over all wavelengths and a half-space yields the Stefan-Boltzmann law:

$$E = \sigma T^4. \tag{2.6}$$

with the Stefan-Boltzmann constant $\sigma = 5.67 \cdot 10^{-8}\ Wm^{-2}K^{-4}$ This equation says, that the power emitted per unit area by a black body only depends on its temperature T in K. For a gray body equation (2.6) is multiplied by a factor ϵ which is smaller than one, depending on its emissivity.

As scattering, absorption and the black body emission highly depend on wavelength, the radiative transfer equation as a whole has a spectral dependency. Despite the complexity of the radiative transfer equation, under certain conditions, there are simple analytical solutions.

2.1.3 The Bouguer-Lambert-Beer law

The simplest solution results if one only considers the attenuation of a light beam by extinction during its propagation through a medium, such as an atmospheric layer with a certain vertical extension for instance. Thermal emission(4) and the scattering integral (3) in equation (2.4) are ignored which reduces the equation of radiative transfer to

$$\frac{dL}{ds} = -\beta_{ext} L. \tag{2.7}$$

Solving this equation for a defined path between two points and using the definition of optical thickness from equation (2.3) yields

$$L = L_0 e^{-\tau} \tag{2.8}$$

L_0 denotes the initial radiance and L the radiance left after propagation through a medium of optical thickness τ. For example, an optical thickness of $\tau = 1$ would mean that 37% of the initial radiance would pass the medium without being scattered or absorbed. Due to the spectral dependency of β_{ext}, τ is in generally different for every wavelength. In this context it is useful to define the term *transmittance* which will be used later

$$T = \frac{L}{L_0} = e^{-\tau} \tag{2.9}$$

Transmittance describes the fraction of light which is not absorbed or scattered and can therefore take values between 0 and 1.

2.1.4 The solar spectrum

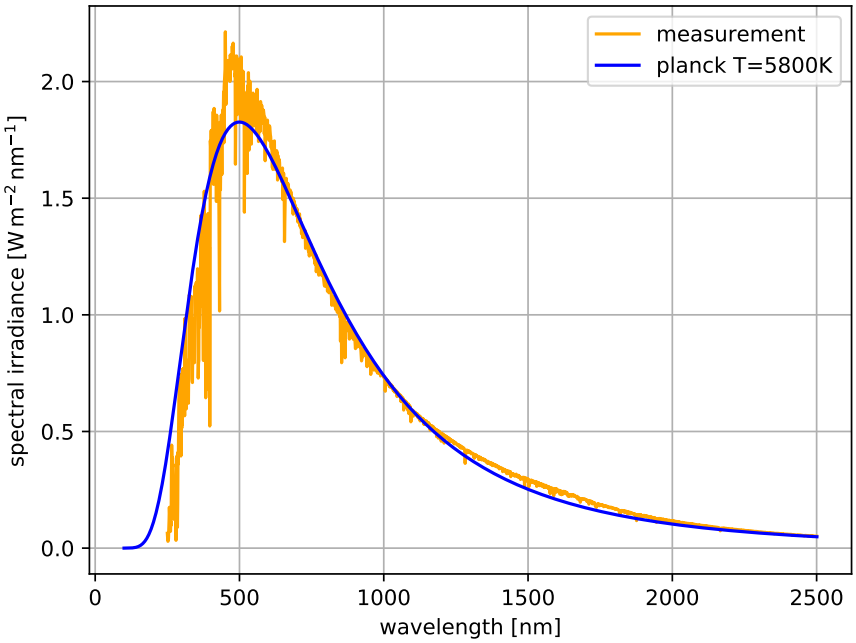

Figure 2.1: Measured solar spectrum with a resolution of 1 nm (Kurucz, 1992) at top of atmosphere (orange) compared to the spectrum of a black body with a temperature of 5800 K (blue) using Planck's law (eq. 2.5).

Solar radiation is by far the most important energy source for the Earths climate system. The current best estimate of top of the atmosphere (TOA) energy flux is 1360.8 $\pm$ 0.5 Wm^{-2}, with fluctuations of 1.6 Wm^{-2} between the recent minima and maxima of the 11-year solar cycle (Kopp and Lean, 2011). The radiation mainly originates from the Sun's *photosphere* which has an average temperature of 5800 K. Therefore, the spectrum of solar radiation can be described by Planck's law of black body radiation (see equation

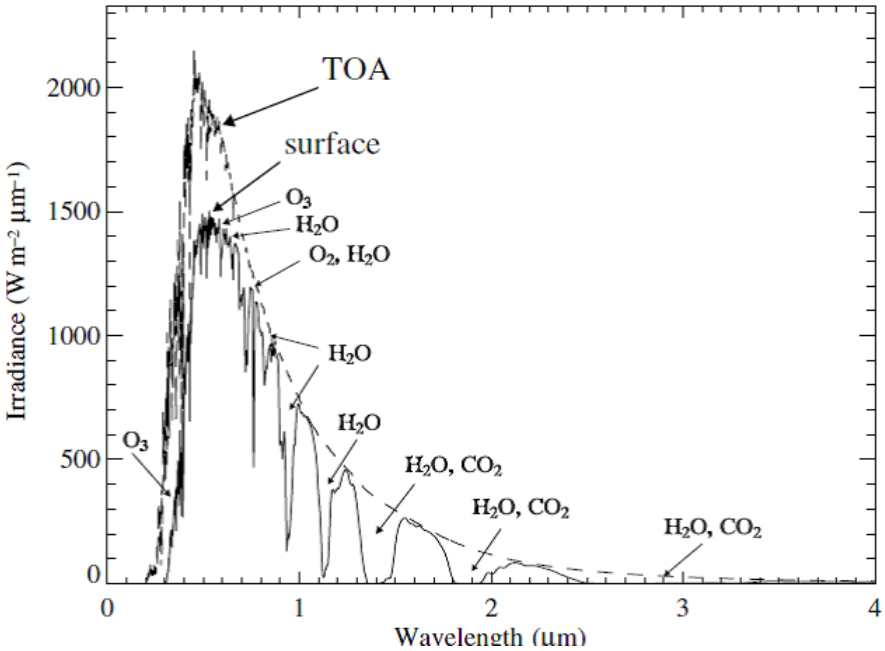

Figure 2.2: Comparison of the measuresd solar spectrum at TOA (dotted) and at the Earths surface (solid). Regions of high attenuation are marked by the responsible absorbing molecules. Figure from Zdunkowski et al. (2007)

2.5) at a temperature of 5800 K. Figure 2.1 shows the comparison of the spectral irradiance between a measured solar spectrum and the theoretical spectrum of a black body at TOA. In the ultra violet part of the spectrum below 185 nm the measured curve shows strong variability which is due to electronic emission lines of atoms located in regions of high temperature in the solar atmosphere. One of the most famous emission lines is the *Lyman-alpha* line of the hydrogen atom at 121.6 nm.

A second feature predominantly occurring in the visible and infrared region of the solar spectrum are absorption lines. They are named *Fraunhofer lines* after their explorer Joseph Fraunhofer and are caused by electronic absorption by atoms in a cooler layer above the photosphere also called *chromosphere*. One of the strongest absorption lines is found at 656.3 nm and caused by the *H-alpha* line of hydrogen.

After the solar radiation has reached TOA it penetrates the different layers of the Earth's atmosphere. A larger fraction of radiation is thereby absorbed by radiatively active gases like H_2O, O_3 and CO_2 or scattered by air molecules and aerosol particles. The the solar spectrum measured at sea level therefore significantly deviates from the one measured at TOA as shown in figure 2.2. The most important absorbing gas in the ultraviolet part of the spectrum is O_3 which is most abundant in the stratosphere. Beside H_2O, O_3 and O_2 are the most important absorbers of visible light. In the infrared spectrum H_2O and CO_2 contribute most to the attenuation of solar radiation.

These strong absorption features of water vapor in the infrared solar spectrum are important for Earth's energy budget and play a crucial role in the cloud detection algorithm

presented in this thesis. Therefore, the physical process of water vapor absorption is discussed in the next section.

2.1.5 Absorption lines of water vapor in the short wave infrared

Absorption of electromagnetic radiation by atmospheric gases is one of the most important process in the Earth's climate system. If there was no absorption there would be no greenhouse effect and the temperature on our planet would be as low as 255 Kelvin, which is about 33 Kelvin below present global mean temperature (Wallace and Hobbs, 2006).

One of the most important radiatively active gases is water vapor, which not only absorbs thermal infrared radiation emitted by the earths surface and atmosphere but also visible and shortwave infrared radiation (SWIR). In the following part a physical explanation for absorption of radiation by molecules and in particular for the absorption by water vapor is given.

When a molecule absorbs a photon, the energy is stored as *internal energy*. The molecule is then said to be in an *excited state*. There are three forms of internal energy in molecules: rotational, vibrational and electronic energy. One important property of all these energy forms is that they are quantized meaning that have discrete values. The energy differences between two rotational energy states appear to generally be the smallest of all three forms of internal energy. A typically energy difference between rotational energy states are a few hundredths of an electron volt ($1eV = 1.602 \cdot 10^{-19}\ J$) corresponding to a photon with wavelength (λ) on the order of millimeters. The energies of vibrational transitions have typically a few tenths of an electron volt which is equal to a photon of $\lambda \sim 10\ \mu m$ and electronic transitions occur at energies of a few electron volt ($\lambda < 1\ \mu m$).

These numbers show that for the solar infrared spectrum vibrational transitions are the ones of interest. Molecules are only able to absorb electromagnetic radiation if they have a permanent or induced electric dipole moment. This is necessary so that the radiation can excite the vibrational modes of the molecule. H_2O for instance has an asymmetrical charge distribution and therefore a permanent electric dipole moment. CO_2, however, can only have an induced electric dipole moment resulting from antisymmetric vibration. The general theoretical approach to determine the vibrational modes of a molecule is to treat it as a quantum mechanical harmonic oscillator with weightless springs connecting the individual atoms. As the energies required for vibrational transitions are considerably higher than for rotational transitions, vibrational transitions generally occur together with rotational transitions. Therefore the rotation is also considered as a rigid rotator in the harmonic oscillator model.

The solution of the Schrödinger equation for the hamonic oscillator rigid rotator model can be separated into rotational and vibrational energy states. The discrete rotation energy levels are described by

$$E_J = Bhc\, J\,(J+1) \tag{2.10}$$

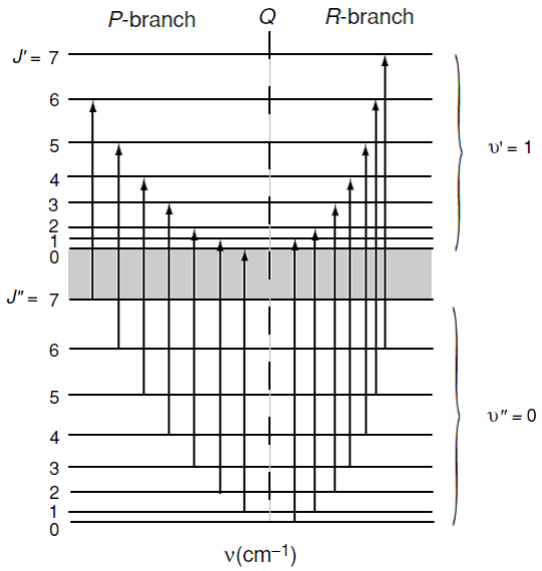

Figure 2.3: Vibrational transitions coupled with rotational transitions for the harmonic oscillator of a molecule. Transitions with $\Delta J = +1$ form the R-branch, $\Delta J = -1$ generates the P-branch. The Q-branch in the center belongs to $\Delta J = 0$ transitions which are nearly at the same wavenumber. Figure from Liou (2002).

where $B = h/8\pi^2 Ic$ is the *rotational constant*, $h = 6.62610^{-34}$ Js Planck's constant, c the speed of light and I the moment of inertia. J denotes the rotational quantum number, which is always an integer. For the harmonic oscillator rigid rotator model the *selection rules* determine the allowed transitions between values of J which are $\Delta J = \pm 1$. In some cases though, also the transition $\Delta J = 0$ is allowed, which will briefly be discussed later. The quantized energy levels for the vibrational modes are given by

$$E_\upsilon = h\nu_k \left(\upsilon_k + \frac{1}{2}\right) \tag{2.11}$$

with the frequency of vibration ν_k and the vibrational quantum number υ_k. The subscript k denotes the normal modes also called *fundamentals*. Triatomic molecules like H_2O have three fundamentals. The selection rules for the vibrational quantum number are $\Delta\upsilon_k = \pm 1$ except for the vibrational ground state $\upsilon_k = 0$ only $\Delta\upsilon_k = +1$ is possible. As vibrational transitions coincide with rotational transitions, the total energy is given by the sum of rotational and vibrational energy:

$$E_{\upsilon,J} = Bhc\, J\,(J+1) + h\nu_k \left(\upsilon_k + \frac{1}{2}\right). \tag{2.12}$$

An example of possible rotational-vibrational transitions is given in figure 2.3. Here ${\upsilon''}_k = 0$ denotes the vibrational ground state and $\upsilon'_k = 1$ the first excited state. Correspondingly J' are the rotational states of the excited vibrational state and J'' the ones of

the ground state. The horizontal axis indicates the wavenumber of the vibration, where higher wavenumbers correspond to higher energies and smaller wavelengths. The left side shows the transitions for $\Delta J = -1$. These transitions belong to the so called P-branch whereas the transitions with $\Delta J = +1$ on the right side of the plot form the R-branch. The Q-branch with $\Delta J = 0$ is only allowed for the ν_2 vibrational mode (bend mode) of linear triatomic molecules and for the three modes of bent triatomic molecules like H_2O. This branch originates from an oscillating dipole moment perpendicular to the internuclear axis. For a linear triatomic molecule, for instance CO_2, the internuclear axis is the line connecting all three atoms. If the molecules bend mode is excited the dipole moment oscillates perpendicular to this internuclear axis, whereas for the antisymmetric stretch mode (ν_3) the dipole moment would oscillate parallel to this axis. For vibrational modes of bent triatomic molecules there is always a component of the dipole moment oscillating perpendicular to this axis.

Calculating the energies of the three fundamental vibrational modes of water vapor, one finds them at the following wavenumbers:

- the symmetric stretch mode ν_1 at 3651 cm^{-1} ($\lambda \approx 2.74\ \mu m$),
- the bend mode ν_2 at 1595 cm^{-1} ($\lambda \approx 6.27\ \mu m$),
- and the antisymmetric stretch mode ν_3 at 3756 cm^{-1} ($\lambda \approx 2.66\ \mu m$)

Figure 2.4: Fundamental vibrational modes of water vapor: symmetric streching (left), bending (middle) and antisymmetric streching (right). Figure from Liou (2002).

Beside these fundamental modes many other absorption bands of water vapor are observed at shorter wavelength. These bands can be explained by the fact that molecules are *anharmonic* oscillators. Therefore, their potential is not parabola-shaped. The actual form of the potential can be approximated by the Morse potential. Using the Morse potential the Schrödinger equation can be solved analytically. The selection rules in this case not only allow for $\Delta v_k = \pm 1$ but also for $\Delta v_k = \pm 2, \pm 3, ..., n$. These transitions are the vibrational *overtones* of a molecule. Their frequencies are correspondingly two, three, ..., n-times the frequency of the fundamental modes. It is also possible for the vibrational quantum numbers of two fundamental modes to change simultaneously. If both quantum numbers increase, the energy of the resulting bands is the sum of the individual transition energies.

In this thesis, only the overtones of water vapor are of interest, because they are

located in the solar spectrum and captured by the SWIR camera of the specMACS instrument. Figure 2.5 shows the transmission of solar radiation through a layer of water vapor at wavelengths between 500 and 2000 nm, calculated using the libRary for radiative transfer (libRadtran) (Mayer and Kylling, 2005) with two different absorption parametrizations. The strongest and broadest absorption bands are located at about 1400 and 1900 nm, but absorption bands are also present at wavelengths as low as 600 nm.

The absorption by water vapor in the SWIR spectrum is used to discriminate clouds from the oceanic background. The reason why this is necessary is the presence of sunglint. Its properties are described in the next section.

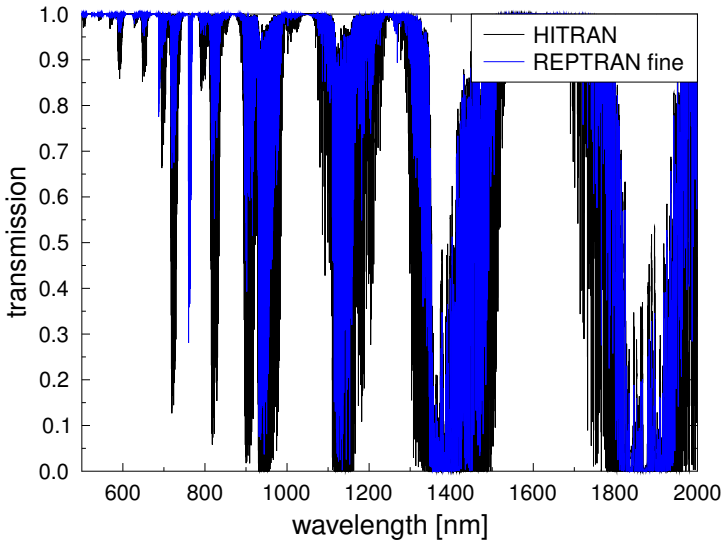

Figure 2.5: Water vapor absorption in the visible and short wave infrared solar spectrum calculated with libRadtran (Mayer and Kylling, 2005). The transmission through the atmospheric layer between surface and 1 km for the US Standard atmosphere is shown. The black curve was calculated using line-by-line absorption from HITRAN (Gordon et al., 2017), for the blue curve, the REPTRAN parameterization with fine resolution was used. Figure by Bernhard Mayer.

2.1.6 Sunglint

The term sunglint describes a common phenomenon occurring when the sunlight is reflected on a rough water surface as shown in figure 2.6. If the water surface is absolutely calm, one can only see the specular reflection of the Sun's disk. Most of the time wind generates a rough water surfaces, because the friction on the boundary between the atmosphere and the water leads to waves. The inclination angle of these waves makes it possible that sun-rays apart from the point of specular reflection are reflected towards

Figure 2.6: Sunglint on the ocean around New Zealand. Image was taken from the International Space Station (ISS). Image from NASA (2018).

the observer. The larger the inclination angle of the waves, the farther away from the specular point light can be reflected towards the observer. Therefore the width of the sunglint is a measure for existing wave slopes. The slope in turn depends on the wind speed, because higher wind speeds can form higher waves with steeper slopes (Cox and Munk, 1954).

These relations were empirically studied by Cox and Munk (1954). They used photographs of sunglint taken from a plane to derive a probability distribution of wave slopes as a function of wind speed. They found an approximately Gaussian and isotropic distribution of wave slopes. The mean square of the wave slope distribution increases linearly with wind speed. However, for high wind speeds the mean square slope in the along wind direction is larger than in the across wind direction. This introduces a skewness in the Gaussian distribution of wave slopes.

The reflectance of the water surface not only depends on the wave slope distribution but also on the refractive index of air and water, the wavelength of the electromagnetic radiation and its polarization. All these parameters are required to solve the Fresnel's equations, which describe the reflection of radiation on the interfaces of different media. Combining the distribution of wave slopes wit h the Fesnel's equations makes it possible to calculate the reflectance of water surfaces for arbitrary viewing geometries. Figure 2.7 shows the reflectance of a water surface for varying wind speeds and fixed solar zenith angle (SZA) of 0° as a function of viewing zenith angles (VZA).

The dotted vertical lines indicate the typical field of view of the specMACS instrument. This plot makes clear that for the data collected during the NARVAL II campaign, sunglint is a frequently occurring feature. Therefore it is necessary to develop retrievals – in this case a cloud detection algorithm – which are not affected by its effects.

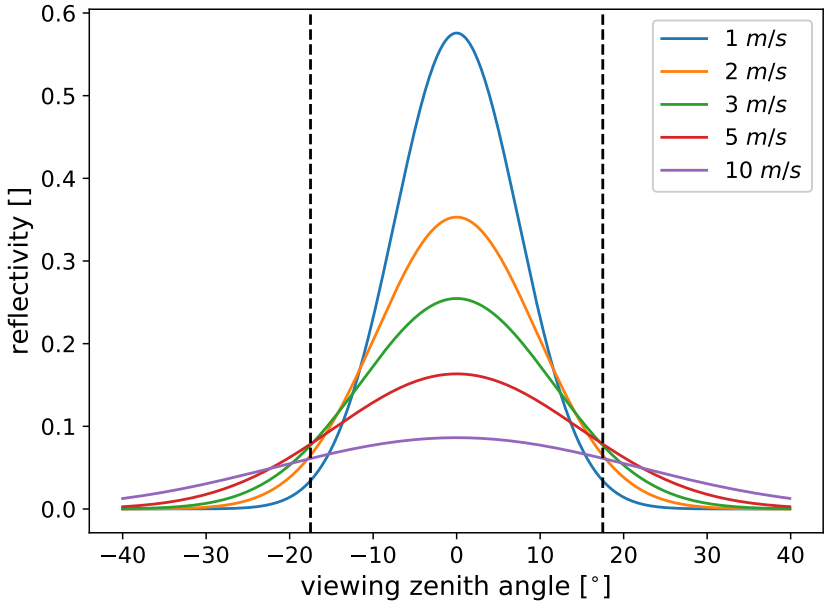

Figure 2.7: reflectance of the oceans surface using the parametrization by Tsang et al. (1985) for different viewing zenith anlgles (VZA) and selected wind speeds. The solar zenith angle (SZA) was set to 0°. The vertical dashed lines mark the typical field of view (FOV) of the specMACS instrument (±17.5°).

2.2 Clouds - properties on different scales

Clouds are a fundamental feature of the Earths atmosphere and occur in a great variety of shapes and sizes. They are an important field of research because they are involved in many different processes in the climate system. Clouds influence the Earths radiation budget by scattering and absorption of solar and terrestrial radiation, they keep the troposphere mixed by moist adiabatic convection and are the major driver of the global water cycle. Some of these micro- and macrophysical properties will be briefly described and discussed in the following sections.

2.2.1 Basics on clouds

Clouds form when warm air rises, cools adiabatically during ascent and at some point, when the air has cooled sufficiently to reach 100% relative humidity, the moisture condenses to form cloud droplets. Having a closer look at this process an important and necessary ingredient making cloud formation only possible, comes into play.

Cloud condensation nuclei (CCN) are hygroscopic aerosol particles. On their surface water molecules can accumulate instead of spontaneously forming a droplet by collision of many water molecules directly from the gas phase. The accumulation on the surface of a CCN has two advantages compared to droplet formation by pure water vapor:

1. The droplets radius starts at the size of the particle, which reduces the vapor pressure

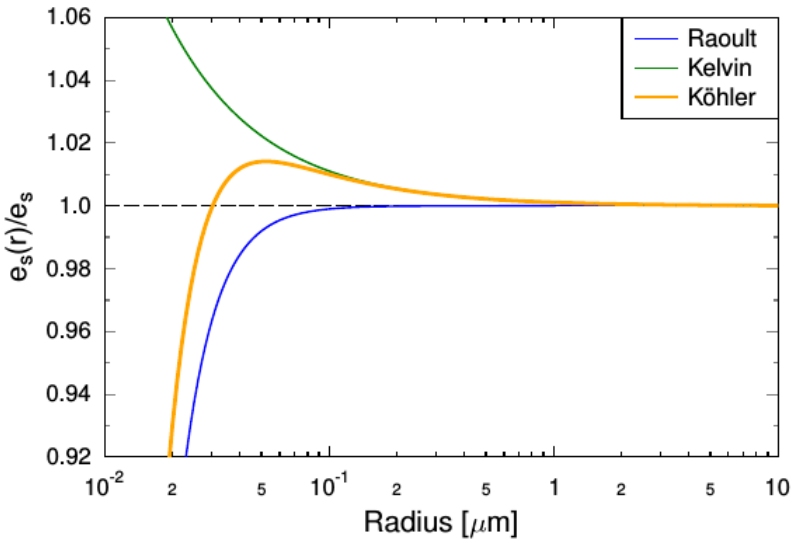

Figure 2.8: Raoult, Kelvin and Koehler-curves for a NaCl CCN with radius 0.01 μm. the Koehler-curve results from multiplication of Raoult and Kelvin curves. Figure from Gödde (2015).

at the droplets surface, due to the *Kelvin effect*, which states, that the vapor pressure rises with stronger curvature of the water surface.

2. In the case of a water soluble CCN like sea salt, ions are dissolved in the droplet which further reduces the vapor pressure of the droplet due to the *Raoult effect*.

Combining these two effects leads to the Koehler (Köhler, 1936) equation which describes the vapor pressure above a curved water surface containing dissolved aerosol. Figure 2.8 shows the result of the Koehler equation for a NaCl-salt CCN with a 0.01 μm radius as well as the contributions of the Raoult and the Kelvin effect. The vertical axis denotes the ratio of the vapor pressure above a curved water surface containing dissolved CCN and the vapor pressure above pure water with flat surface. In this case the Koehler curve shows a maximum value of 1.014 at a radius of roughly 0.05 μm. This means the air has to be supersaturated by more than 1.4% for the droplet to grow larger than this *critical radius*.

CCN significantly reduce the vapor pressure on a droplets surface by enhancing the droplet's radius. Without CCN a droplet consisting of 58 water molecules for instance has a five times higher vapor pressure compared to a flat water surface, which under realistic atmospheric conditions would cause its rapid evaporation(Rogers, 1975).

The largest climate impact of clouds is the modification of the global radiation budget. Clouds have different radiative properties depending on the wavelength of the radiation. For wavelength larger than about 5 μm (longwave radiation) clouds strongly absorb and emit radiation whereas they mainly scatter radiation in the visible and near infrared spectrum (shortwave radiation).

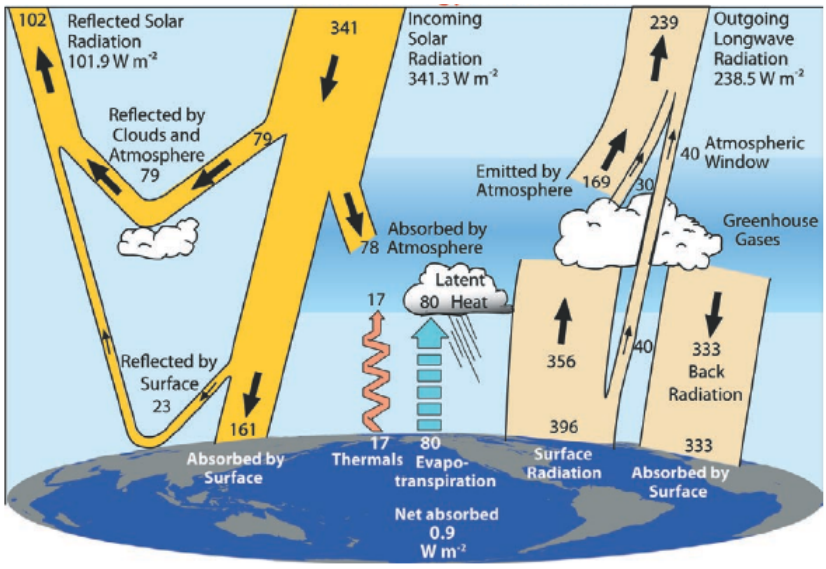

Figure 2.9: Global annual mean state Earth's energy budget from March 2000 to May 2004. Fluxes are given in Wm^{-2}. Figure from Trenberth et al. (2009).

These two properties lead to counteracting effects in the Earth's radiation budget. Incoming solar radiation is partially scattered back to space, which reduces the energy input. This effect is referred to as the shortwave cloud radiative effect (SWCRE). However, clouds absorb and re-emit thermal infrared radiation emitted by the surface, which traps part of the radiated energy from Earth's surface. This is called the longwave cloud radiative effect (LWCRE). A schematic sketch of these processes is shown in figure 2.9. According to studies by Chen et al. (2000), clouds reflect 53.5 Wm^{-2} of the solar shortwave radiation in the global annual mean. This amount is incorporated in the 79 Wm^{-2} of reflected solar radiation on the upper left side of figure 2.9. The figure shows the global energy budget and the involved fluxes of solar and thermal radiation as well as sensible and latent heat transport. The contribution of clouds to the planetary albedo can be estimated by taking the ratio between the flux of cloud-reflected and the total reflected solar radiation shown in top-left branch of figure 2.9 (102 Wm^{-2}). This calculation demonstrates that clouds are responsible for more than 50% of the planetary albedo, which emphasizes their importance for Earth's climate.

For the longwave effect Chen et al. (2000), calculated a positive effect of 20.1 Wm^{-2} on the global energy budget. This number cannot easily be assigned to a single branch in the right part of figure 2.9, because it is a net effect resulting from the difference between emitted downwelling and upwelling radiation. As the SWCRE dominates the LWCRE on the global average, clouds have a overall negative effect of -33.4 Wm^{-2} on the global energy budget (Chen et al., 2000).

In the following sections the optical properties of clouds leading to the above described effects and a explanation for the strong shortwave effect of clouds will be given.

2.2.2 Radiative properties

The optical properties of a cloud as a whole depend on the microphysical conditions like the cloud phase, the effective droplet radius and the number concentration of droplets within the cloud. For simplicity this section will only address liquid water droplets and omit the ice phase.

The theory describing the interaction between electromagnetic radiation and spherical particles is called *Mie theory* (Mie, 1908). With this tool the scattering by water droplets can be calculated in detail. Important quantities in this context are:

- **Size parameter** x: It is defined as $x = 2\pi r \lambda^{-1}$ where r denotes the radius of the particle and λ is the wavelength of the radiation. The scattering and absorption properties of a particle depend strongly on this relation.
- **Complex refractive index** $\mathcal{N}$: Consists of a real part (n_r) and a imaginary part (n_i) where the sum of both gives the complex refractive index: $\mathcal{N} = n_r + i\, n_i$. The real part describes the propagation of radiation in a medium and its behavior at interfaces of media with different indices. The imaginary part reveals information about the attenuation of the radiation or the absorption within a certain medium. Both parts depend on the wavelength of the electromagnetic radiation. in the visible spectrum their values for pure water are are $n_r \approx 1.33$ and $n_i \approx 10^{-8}$ (Segelstein, 1981)

In this thesis light scattered by clouds in the short wave infrared spectrum (SWIR) scattered is examined. To describe the scattering by clouds it is necessary to understand the the scattering behavior of individual droplets. There are two main quantities used to describe the scattering by cloud droplets. The first one is the scattering phase function which reveals information about the probability that a photon will be scattered into a certain direction relative to the incidence direction. The angle between the initial direction of the photon and the direction into which it is scattered is called the scattering angle Θ. A scattering angle of $\Theta = 180°$ means that the photon is scattered back into the direction it came from (reflection), whereas a scattering angle of $\Theta = 0°$ occurs if the photon*s direction remains unchanged (see figure 2.10). The phase function $\mathcal{P}$ expressed in terms of the cosine of the scattering angle: $\mathcal{P}(\cos\Theta)$.

The second quantity is the scattering efficiency Q_{sca}. It is related to the scattering cross section (σ_{sca}) defined in section 2.1.1 as the ratio of σ_{sca} and the geometrical cross section (σ_{geo}). A scattering efficiency of 1, means that the scattering cross section is equal to the geometrical cross section of the object. The value of Q_{sca} determines the optical thickness of a cloud and therefore its optical properties.

To calculate these two quantities using Mie theory, the complex refractive index as well as the size parameter of the particle must be known. A typical wavelength in the SWIR is 1.2 μm, and radii of cloud droplets are usually as large as 10 μm. The equation for the size parameter described above therefore yields a size parameter of $x \approx 50$. The real part of the refractive index is $n_r \approx 1.32$ and the imaginary part amounts $n_i \approx 10^{-5}$ (Segelstein, 1981). The value of n_r is close to the one given before for the visible spectrum, n_i is 10^3-times higher than in the visible spectral range, but still small.

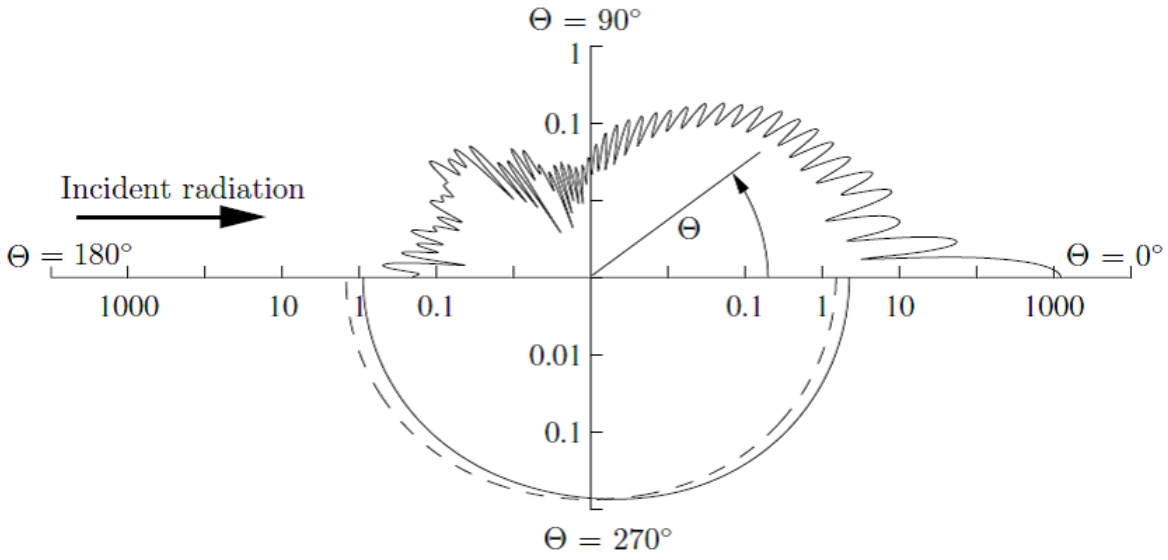

Figure 2.10: Polar plot of the scattering phase function $\mathcal{P}(\cos\Theta)$ for three different size parameters calculated with Mie theory. Dashed curve: $x = 0.01$, lower solid curve: $x = 1$, upper solid curve: $x = 50$. A complex refractive index of $\mathcal{N} = 1.33 + 0i$ was used. Figure form Zdunkowski et al. (2007).

Calculating the scattering phase function for different size parameters and a complex refractive index of $\mathcal{N} = 1.33 + 0i$ yields the result shown in figure 2.10. Mie phase functions are rotationally symmetric with respect to axis of the incident light. Therefore, the full phase function can be obtained by mirroring each curve on the horizontal axis. The distance between each point on the phase function and the origin is $\mathcal{P}(\cos\Theta)$. For SWIR radiation and cloud droplets, only the phase function for $x = 50$ is of interest. Compared to the smooth phase functions that occur in the rayleigh limit (for futher information see Zdunkowski et al. (2007)), the complexity of the structure increases due to the presence of smaller and larger ripples. Another important feature is the strong peak in the forward direction ($\Theta = 0$), whereby the logarithmic axes should be noted. The strong forward peak results in an asymmetry parameter close to unity. This is the reason why clouds with small optical thickness, appear very bright even if they reside between the sun and the observer.

Figure 2.11 shows the scattering efficiency as a function of the size parameter x, calculated with Mie theory. The plot contains curves for different values of the imaginary part of the refractive index, the real part is $n_r = 1.33$ as before. One prevalent feature is the strong oscillation of the scattering efficiency for spheres with small or zero complex refractive index. These maxima and minima are due to interference of light transmitted through and diffracted by the particle. The superimposed ripples are caused by light rays barely touching the edge of the particle and traveling around it whereby small amounts of energy are emitted in all directions. The fine structure as well as the large maxima and minima are reduced at larger values of n_i (κ) due to absorption. The larger the particles, the longer the absorption path of light propagating through the particle which leads to

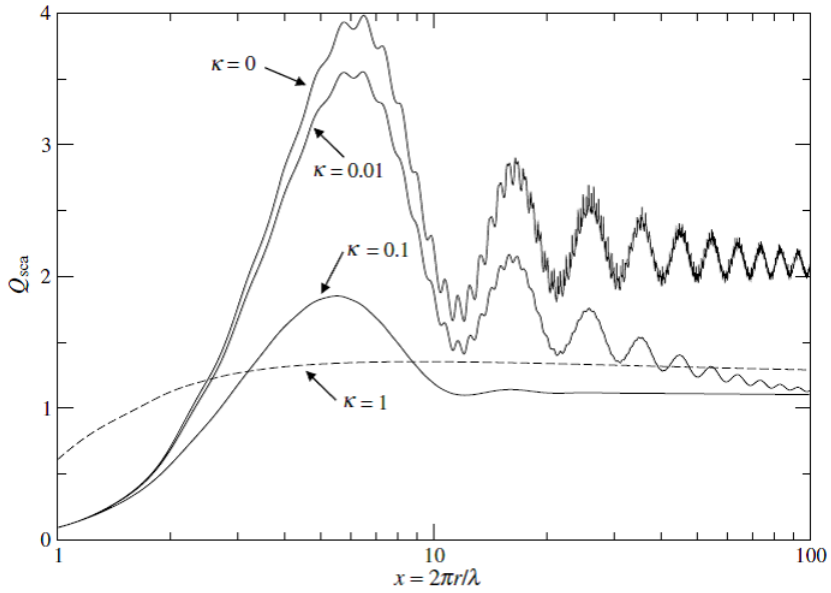

Figure 2.11: Scattering efficiency Q_{sca} as a function of size parameter x. Curves for different values of the imaginary part of the complex refractive index κ (denoted as n_i in the text) are shown. Figure form Zdunkowski et al. (2007).

smoother curves and reduces Q_{sca}. For scattering of SWIR radiation on cloud droplets, the curve for $n_i = 0$ in figure 2.11 is representative, as the imaginary part of the refractive index of ater is roughly 10^{-5}.

A remarkable property of the curve for $n_i = 0$ is that it oscillates around a value of $Q_{sca} = 2$, which means that the scattering cross section is twice the geometrical cross section. For a non absorbing particle ($n_i = 0$) $Q_{sca} = Q_{ext}$ wherefore also the extinction cross section is twice the geometrical one. This so called *extinction paradox* can be explained by light being diffracted by the edge of the particle without being in direct contact with it. Therefore, the particle also affects light rays apart from its geometrical surface. It should be noted that the small difference between the refractive index of the calculations presented and the one given as typical value for the SWIR spectrum does not change the result decisively. It may would slightly change the position of minima and maxima and the small ripples but the overall message of the figures 2.10 and 2.11 stays the same.

With the knowledge about the scattering properties of individual cloud droplets it is now possible to asses the scattering behavior of a cloud. As a first step a equation for the optical thickness of a cloud is derived according to equation (2.3).

The extinction coefficient β_{ext} was defined as the product of the extinction cross section σ_{ext} and the number density of scattering/absorbing particles n. The droplet number density within a cloud can be cvalculated from geometrical considerations as

$$n = \frac{3\,LWC}{4\pi\, r_{eff}^3\, \rho_w} \tag{2.13}$$

with the number density n in m^{-3}, the effective droplet radius r_{eff} in m, liquid water content LWC and the density of water ρ_w in units of $kg\,m^{-3}$. The effective droplet

radius of a cloud is calculated from the droplet size distribution and is representative for the optical properties of the whole distribution (see Liou (2002) for a definition). For spherical droplets also the extinction cross section can be defined in terms of r_{eff} and the extinction efficiency:

$$\sigma_{ext} = Q_{ext} \pi r_{eff}^2 \tag{2.14}$$

Q_{ext} is without units and σ_{ext} has units of m^2. As the absorption efficiency for the considered SWIR radiation is close to 0 for cloud droplets, Q_{ext} and Q_{sca} are approximately equal and are used interchangeably from now on. Assuming a homogeneous cloud with constant LWC and r_{eff} throughout the cloud, the path integral of the optical thickness in equation (2.3) reduces to a simple multiplication by the geometrical thickness Δz of the cloud, since β_{ext} is independent of the location within the cloud. Inspecting figure 2.11, $Q_{ext} \approx 2$ can be chosen as a good approximation. Using these simplifications together with equations (2.13) and (2.14) yields an approximate formula for the vertical optical thickness of the cloud

$$\tau_{cld} \approx \frac{3\, LWC}{2\, r_{eff}\, \rho_w} \Delta z \tag{2.15}$$

The vertical thickness Δz has unit of m, τ_{cld} is without units. This simple equation shows the dependence of the optical thickness of a cloud on the parameters: LWC, r_{eff} and Δz.

A larger LWC for fixed r_{eff} results in a larger number of cloud droplets that have a higher cumulative surface, which to higher τ_{cld}. Therefore, it is more probable that light entering the cloud is scattered. The opposite process occurs, when r_{eff} rises for fixed LWC. A smaller number of large droplets has a lower cumulative cross section than many small droplets for the same LWC, which decreases τ_{cld}. The variation of the geometrical thickness of the cloud Δz directly scales τ_{cld} by enlarging or reducing the light path through the cloud. A longer path enhances the probability of a scattering event an vice versa.

The property of interest for air or spaceborn observations, is cloud reflectance. To asses the reflectance of a cloud, the scattering phase function of a cloud droplet and the optical thickness of the cloud have to be related. On the one hand the phase function contains information about the probability that a single photon is scattered into a certain direction. On the other hand the optical thickness is a measure for the number of scattering events a photon encounters.

Considering an optically thin cloud of $\tau_{cld} = 3$ and the sun at a zenith angle of 0° (noon at the equator), it is quite probable that a photon will be scattered (95%) if it enters the cloud, but the number of scattering events will be 3 or less in most cases. As the scattering phase function has a strong forward peak (see fig. 2.10), only a small fraction of the photons will be scattered in backward direction ($90° < \Theta < 270°$) and leave the cloud in upward direction. Therefore the cloud appears relatively dark from above. For a cloud of $\tau_{cld} = 30$, each photon will encounter a large number of scattering events. This considerably enhances the probability for the photon to be scattered back towards space which makes the cloud look way brighter. Of course, this effect saturates for large optical thicknesses as transmission goes to zero.

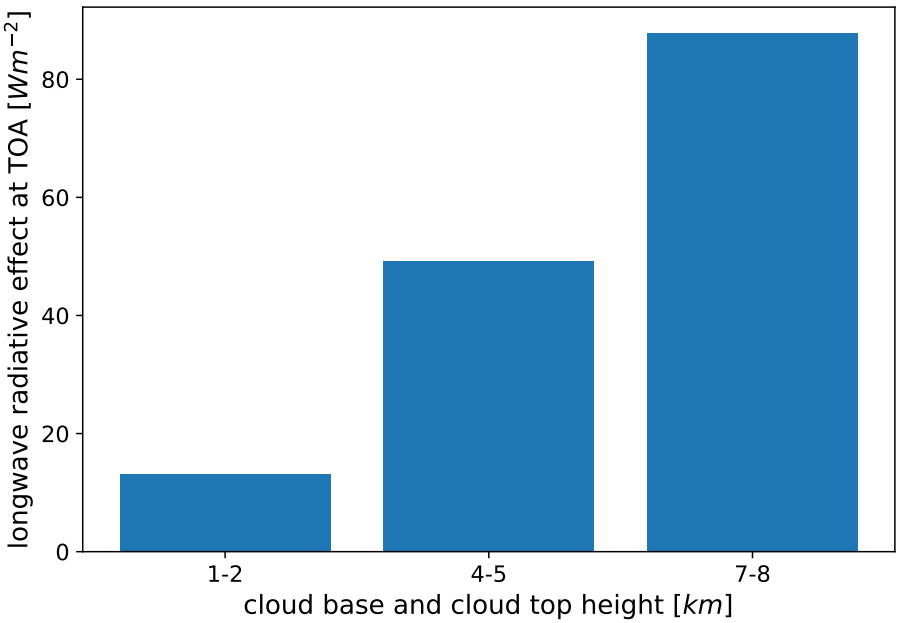

Figure 2.12: Net cloud radiative effect in the thermal infrared spectrum (LWCRE) for water clouds at three different altitudes. The radiative transfer calculations were performed using the DISORT solver from the libRadtran software package (Mayer and Kylling, 2005). The exact model-setup can be found in table 6.1 in the appendix.

Equipped with this micro- and macrophysical knowledge about clouds and their radiative properties, the global role of shallow cumulus clouds will be discussed

2.2.3 Clouds and energy budget – a closer look

In section 2.2.1 the globally averaged contribution of clouds to the Earth's energy budget was described. Looking at this effect in more detail, it turns out that the contribution of individual clouds to the global average, differs considerably. The magnitude of the longwave cloud radiative effect (LWCRE) for instance, highly depends on the clouds' temperature, because the amount of emitted radiation scales with its fourth power according to the Stefan-Boltzmann law (eq. 2.6). This means, that a cloud near the surface emits nearly as much longwave radiation as it absorbs, since surface and atmosphere below radiate at similar temperature. Therefore, the LWCRE is small. On the contrary, a high and cold cloud emits far less radiation than it absorbs, which leads to a high LWCRE as shown in figure 2.12.

The shortwave cloud radiatve effect (SWCRE) also depends on the specific properties and in particular on the optical thickness of the cloud. An optically thin cirrus cloud for instance, reflects less solar radiation than a optically thick cumulus cloud and therefore only has a small negative SWCRE.

The net radiative effect of a cloud on the radiation budget is ultimately the result of the sum of the shortwave and longwave effects at top-of-atmosphere (TOA). TOA defines the outer boundary of the Earth's atmosphere. If the climate system was in equilibrium, the net flux at TOA would be zero. Therefore, determining the instantaneous change in net radiation flux due to a certain disturbance – like for example a cloud – reveals information about the influence of the disturbance on climate. A negative net flux means that more energy leaves the Earth's system than enters it, which leads to a cooling and vice versa.

To assess the global cloud radiative effect, the contributions of all the different cloud types in Earth's atmosphere need to be taken into account.

2.2.4 Shallow cumulus convection

Shallow cumulus convection plays a crucial role in Earth's climate system (Siebesma et al., 2003). One important property of these clouds in the context of climate is their interaction with radiation. As described in section 2.2.1 clouds on average have a negative and therefore cooling effect on Earths climate, but the contribution to this negative effect differs significantly with the properties of clouds (see previous section).

(Chen et al., 2000) split the global cloud radiative effect into contributions from various cloud types. They found, that shallow cumulus clouds contribute significantly to the overall negative effect of clouds. There are two major reasons for this disproportionate influence. The first is that shallow cumulus clouds are located in the lower troposphere and are only slightly colder than the Earth's surface, which results in a small LWCRE (compare figure 2.12). At the same time they are often optically thick and therefore have a high reflectance (see section 2.2.2), yielding a high SWCRE. The second reason is their high frequency of occurrence in the tropics and mid-latitudes.

Chen et al. (2000) used a satellite cloud climatology from the International Cloud Climatology Project (ISCCP) and a radiative transfer model to investigate the radiative effect of different cloud types on a global scale. They estimated the LWCRE of shallow cumulus clouds to be 4 Wm^{-2}. Their result for the corresponding SWCRE was -33.8 Wm^{-2}. These numbers were derived by comparing the radiative fluxes for clear sky and cloudy sky for otherwise equal meteorological conditions. The globally averaged net effect of shallow cumulus clouds is -4.6 Wm^{-2}, which is roughly 14% of the overall cloud radiative effect.

Another important atmospheric process shallow cumulus clouds are involved in is the Hadley circulation. It is driven by deep convection in the tropics called the intertropical convergence zone (ITCZ). Shallow cumulus clouds that occur in the trade wind region north and south of the ITCZ are referred to as trade-wind cumulus clouds. The enhanced vertical transport of moisture by these clouds increases the evaporation from the oceans. The concentration of water vapor in the trade-wind boundary layer is therefore higher when convective clouds are present. The collected water vapor is then transported by the trade winds towards the ITCZ where it releases its latent heat in deep convective clouds. This process is illustrated in figure 2.13. The strength of convection depends on the buoyancy of air masses, which increases through release of latent heat. Consequently,

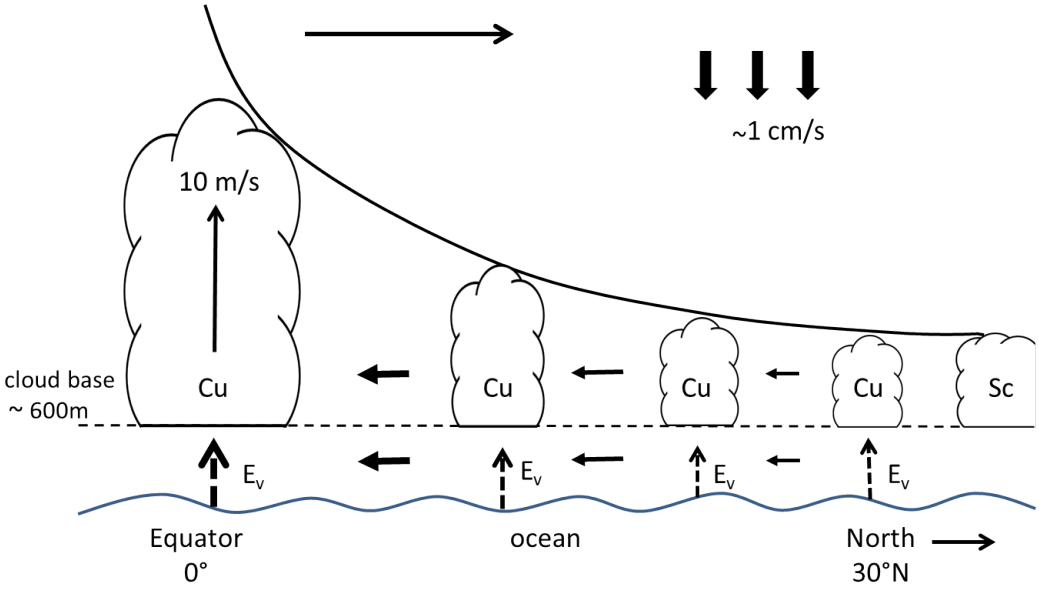

Figure 2.13: Sketch of the cross-section of the northern branch of the Hadley circulation. Illustration of the enhanced moisture convergence due to higher evaporation (E_v) in the presence of trade wind cumuli. Large scale subsidence north (and south) of the ITCZ creates an inversion which prevents the cumuli from growing to higher altitudes. Figure redrawn from Tiedtke (1987).

higher concentrations of water vapor lead to a stronger upwelling in the tropics and consequently to an enhanced circulation. Therefore, shallow cumulus clouds upstream of the ITCZ control the strength of the Hadley circulation and thereby influence the transport of air masses on a global scale (Siebesma, 1998).

2.2.5 Cloud size distribution

Deriving cloud size distributions from air and spaceborne imaging instruments is an important step in evaluating the quality of cloud resolving models. Cloud size distributions derived from measurements can not only directly be compared to the one occurring in the model simulation, but also mass and energy fluxes calculated based on the measured cloud size distribution serve as a proxy for model performance (Zhao and Di Girolamo, 2007).

According to the studies of Zhao and Di Girolamo (2007) the cloud size distribution of cumulus clouds can objectively be best represented by the following power law equation:

$$n\left(D\right) = aD^{-\lambda} \tag{2.16}$$

where $n(D)$ denotes the number of clouds with cloud area-equivalent diameter D. The constants a and λ have to be determined by regression. This regression is most convenient if one takes the natural logarithm of equation (2.16), which yields the linear function

$$\ln n\left(D\right) = a - \lambda \ln D \tag{2.17}$$

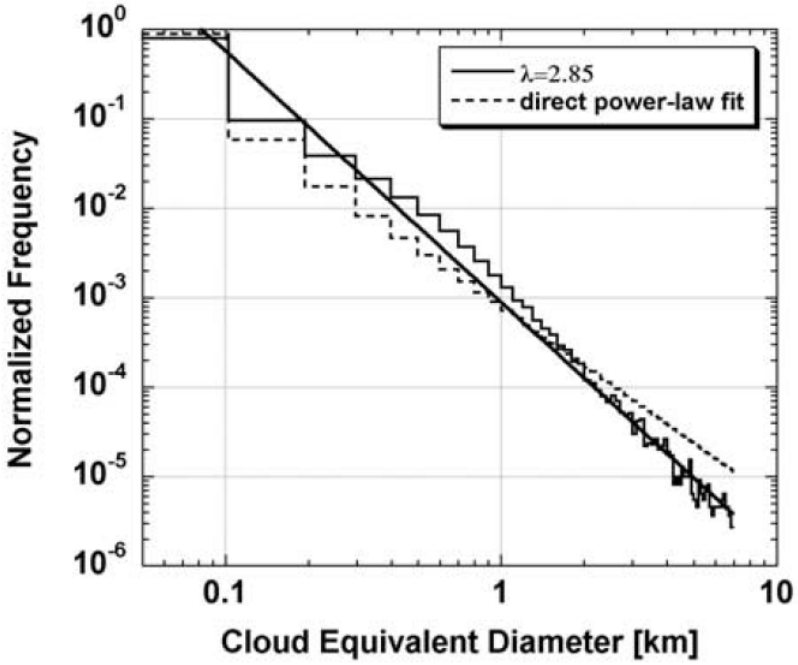

Figure 2.14: Cloud size distribution of cloud area-equivalent diameter D for data of all 152 examined ASTER satellite scenes. Clouds with $D < 7\ km$ are binned with a bin-width of 100 m (solid step line). The solid line shows power law fit according to equation (2.17) with $\lambda = 2.85$. The dotted step line represents a direct power law fit. Figure from Zhao and Di Girolamo (2007).

In this form the constants can be determined by a linear least square fit. Zhao and Di Girolamo (2007) applied this regression to 152 scenes captured by the ASTER (Advanced Spaceborne Thermal Emission and Reflection Radiometer) satellite instrument over the tropical western Atlantic. The cloud area-equivalent diameters were therefore binned with a bin-width of 100 m. Using all available data the least square fit for the cloud size distribution yields $\lambda = 2.85$. The histogram of this result is shown in figure 2.14. Investigating each day of data separately they find values for λ between 2.58 and 3.55.

It should be noted that the cloud size distribution, unlike the cloud fraction, does not heavily depend on the accuracy of the cloud mask. Clouds can for example be detected by using a brightness threshold to an image. A higher threshold in this case means that, clouds have to brighter and therefore optically thicker (compare section 2.2.2) to be detected. The smallest clouds may then not be detected anymore, but at the same time only the parts of larger clouds which are bright enough to surpass the threshold are labeled as cloudy. Increasing the threshold only removes the edges of larger clouds in the cloud mask, because the optical thickness of cumulus clouds is usually larger in their center where the strongest updrafts are present. Therefore λ will not change, but the whole distribution will shift towards smaller clouds, because clouds of all sizes are shrinking. Decreasing the threshold has the opposite effect: even smaller clouds will be

detected and the clouds which were also detected with a higher threshold will grow in size. This results in a shift of the cloud size distribution towards larger clouds and λ will still stay the same (Zhao and Di Girolamo, 2007).

Observing a power law cloud size distribution in measurements leads to the question of whether this natural behavior can be explained by a theoretical model. In the Phd thesis by Windmiller (2017), a simple model based on percolation theory was developed, which is able to predict observed cloud size distributions in the study of Zhao and Di Girolamo (2007). Percolation theory deals with the behavior of randomly distributed objects and the clusters which occur when individual objects overlap (Shante and Kirkpatrick, 1971) – in this context the objects are clouds. The standard percolation model was modified by enhancing the probability that clouds occur in the neighborhood of already existing clouds. In nature this tendency towards clustering can for instance be supported by cold pool cloud triggering (Windmiller, 2017).

To derive quantities like the cloud size distribution and cloud fraction it is necessary to detect the clouds in the investigated images and obtain a cloud mask. The following sections introduce common techniques for cloud detection and the error sources involved in the detection process and cloud fraction determination.

2.3 Cloud mask and cloud fraction

Detecting clouds is an important task in the field of remote sensing for numerous reasons. For example, if a retrieval for cloud microphysical properties (e.g. Nakajima and King (1990)) is applied to a measurement it will only yield physically useful results if a cloud is actually observed. Furthermore, the assessment of the Earths albedo is closely connected to the amount of clouds in the atmosphere. To retrieve a cloud climatology, satellite images are used to infer their global distribution by flagging individual measurements as cloudy or clear. This was done in the International Cloud Climatology Project (ISCCP). The classification of the data into "cloud" and "no cloud" results in a cloud mask.

This section presents common methods used to derive cloud masks and cloud fraction together with the associated error sources.

2.3.1 Common techniques used for cloud detection

The automation of cloud detection using computer algorithms has given rise to a variety of techniques that can be used to identify clouds in data of different imaging instruments. A common and simple group of approaches are*threshold techniques*. Thresholds are applied to many different measured quantities. The basic idea is that cloudy pixels differ systematically from clear pixels in one or more measured quantities or combinations of them.

One obvious feature of clouds is their high reflectance in the solar spectrum compared to water and most of the land surfaces. This means that a threshold can be set for the observed radiance. Pixels with radiances higher or equal to the threshold are assumed to be cloudy, radiances lower than the threshold are labeled as cloud free. The simple

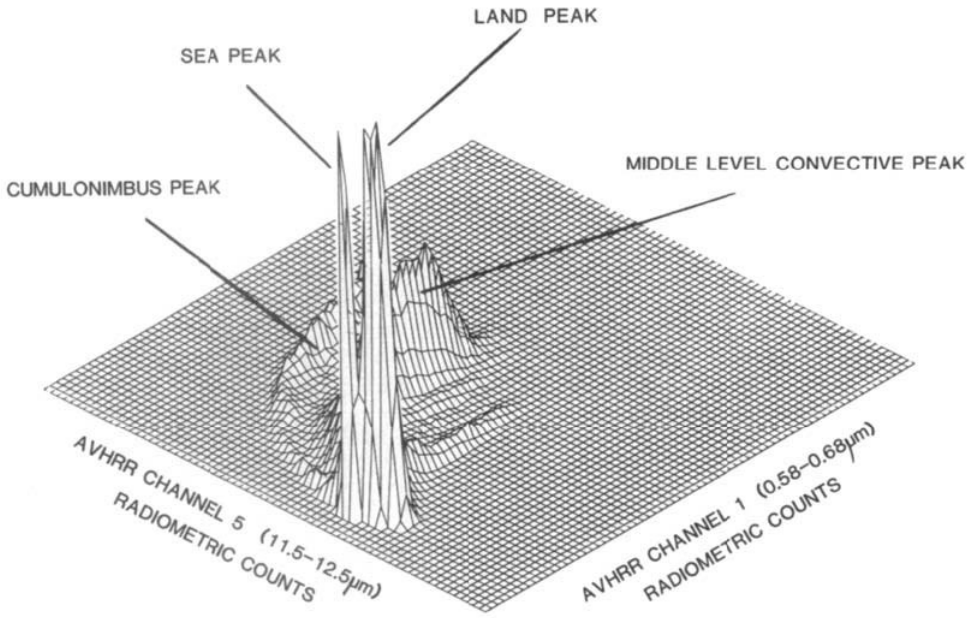

Figure 2.15: Two-dimensional histogram of infrared channel 5 (11.5-12.5 μm) and visible channel 1 (0.58-0.68 μm) for a scene captured by the AVHRR (Advanced Very High Resolution Radiometer) satellite instrument. The frequency is shown in the vertical (third) dimension. Figure from Goodman and Henderson-Sellers (1988).

reflectance approach fails though, as soon as snow or ice covered land and sea surfaces as well as bright deserts come into play. For these cases information from other spectral regions sensitive to the existing conditions is necessary. The exact determination of the threshold can be done either by visual inspection, the use of radiative transfer models or with the help of statistics.

A second group of methods for cloud detection are *statistical cloud retrievals*, whereby a large number of radiance measurements from one or more spectral channels is taken as a reference data set. These measurements are then plotted in one or multidimensional frequency histograms. Figure 2.15 shows a two-dimensional histogram using data of two wavelength channels from the Advanced Very High Resolution Radiometer (AVHRR) satellite instrument. In this plot several areas of high frequency form differently sharp peaks. These peaks can be assigned to different classes, like sea surface, land surface, cloud or even different cloud types. The major challenge using these statistical techniques is to isolate the classes (peaks) from each other and in particular to separate cloud peaks from all others.

This can for example be done by fitting a Gaussian distribution to each peak (Simmer et al., 1982) or using dynamic clustering algorithms. The clustering algorithm developed by Desbois et al. (1982) (adapted from Diday E. (1976)) iteratively identifies classes together with their center of gravity and the variance in a three dimensional histogram.

Another statistical approach is given by spatial coherence algorithms. This method was especially brought forward by Coakley and Bretherton (1982). They used the 11 μm brightness temperatures from the AVHRR instrument and plotted the local standard deviation as a function of the local mean brightness temperature for an array of 8x8 pixels respectively. The result of this procedure is shown in figure 2.16. Three categories can

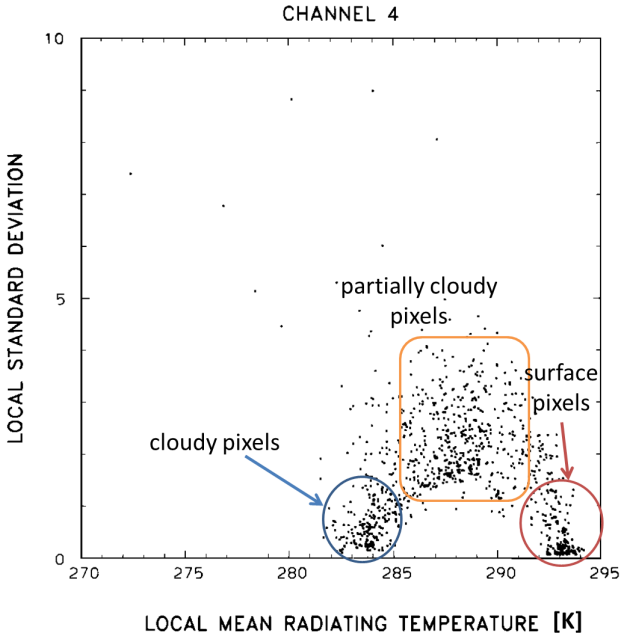

Figure 2.16: Scatterplot of the local mean 11 μm brightness temperature against the local standard deviation calculated from arrays of 8x8 pixels ($\approx 32km^2$). The brightness temperatures are taken from the AVHRR satellite instrument. Points on the lower right side (red circle) belong to cloud free regions, points clustered on the lower left side of the plot represent cloudy pixel arrays (blue circle). Points in between at high standard deviations (orange rectangle) result from partially cloudy pixel arrays. Figure adapted from Coakley and Bretherton (1982).

be identified in this plot: cloudy, partially cloudy and surface. Points accumulated at high brightness temperatures on the right hand side belong to cloud free surface pixel arrays whereas the high density of points at lower temperatures of around 284 Kelvin is due to cloudy pixel arrays. The points between these two boundaries with high standard deviations, belong to partially cloudy pixel arrays and give the plot a arc shaped form. The advantage of this method against all methods presented so far lies in its ability to identify partially cloudy pixel arrays. For simple one-layer cloud decks even the sub-grid scale cloud fraction can be estimated from the superposition of cloudy and clear sky radiances. This method works well for surfaces with homogeneous temperature fields like sea surfaces. Higher temperature variances over land distort the clear separation encountered in figure 2.16 and therefore may introduce ambiguities.

These statistical methods differ from threshold techniques in that features like clouds arise from the analysis itself and are not the result of a priori assumptions about their properties. Additionally, statistical techniques implicitly define thresholds by separating classes in histograms. Therefore they can be used to interactively set thresholds for the above described threshold techniques, because the statistics may change with time and conditions.

A third class of cloud detection and retrieval methods involves the use of radiative transfer models. Reynolds and Vonder Haar (1977) developed a set of simple equations which make it possible to estimate the subgrid scale cloud cover of a single pixel or an array of pixels from spectral radiance measurements in the visible and thermal infrared spectrum at wavelengths of 0.6 and 11 μm respectively. This retrieval is based on the assumption that bidirectional reflectance of the surface and clouds, the infrared emissivity, the solar irradiance and the infrared emitted radiance of the surface are known. The measured visible and infrared radiance is then reconstructed assuming a superposition of radiances from cloud and clearsky visible reflection and infrared emissions. The contribution of the cloudy radiance to the measured radiance then provides the estimate of the cloud fraction.

Rossow et al. (1985) presented a more complex radiative transfer approach which was part of the ISCCP cloud algorithm intercomparison. Compared to Reynolds and Vonder Haar (1977) they included for example absorption by ozone, rayleigh scattering and multiple scattering as well as varying surface reflectivty - in particular enhanced reflectance due to snow and reflectiviy of water surfaces. In a first step they used the model to retrieve cloud optical thickness and cloud top height from visible (0.6 μm) and infrared (11 μm) radiances assuming each pixel is entirely cloud covered. Pixels with an optical thickness smaller than 0.4 or a cloud top altitude lower than 0.5 km were flagged cloud free.

With the fast improvements in radiative transfer modeling in the last decades, these two methods are of course far away from state-of-the-art radiative transfer methods but their simplicity makes it possible to get a flavor of the ideas behind these methods without having to go into to much detail.

A problem with all methods is that each one is only suitable for very specific environmental conditions. Therefore, it is necessary to combine multiple of these methods to obtain cloud detection algorithms applicable for a larger set of locations and conditions. Additionally, information about the climatological mean state, surface properties and even data from numerical weather prediction models (NWP) are used to develop universal cloud detection algorithms.

One general cloud detection and classification algorithm was presented by Derrien and Le Gléau (2005). This algorithm was designed for the Spinning Enhanced Visible and Infrared Imager (SEVIRI) aboard the first Meteosat Second Generation (MSG) satellite. The SEVIRI instrument measures 12 spectral bands located in the visible, near infrared and thermal infrared. This large variety of available measurements across many different spectral regions makes it possible to develop such a general cloud detection algorithm.

This algorithm uses a multispectral thresholding technique whereby the applied tests depend on conditions like illumination and geographical location. A great part of the thresholds is computed interactively using radiative transfer models. The input data for the computations are taken for instance from NWP forecasts and climatology maps. In total 13 different test are used, which make use of the different spectral properties of clouds, land and sea surfaces.

One interesting aspect of this algorithm is that it contains a test designed to detect low clouds in the presence of sunglint. The reflectance of clouds at 3.9 μm compared to the 0.6 μm is lower than for light scattered on the ocean's surface, which makes it possible to detect the clouds in this complicated situation. This spectral property of clouds can not be used for the data used in this thesis, because only radiance at wavelengths between 0.4 and 2.5 μm are available.

After all cloud test have been applied, clouds are separated into 21 different cloud types using spectral features already examined in the cloud detection step as well as through comparison of the 10.8 μm brightness temperature to NWP forecast air temperatures.

This example shows that also recent highly complex cloud detection and classification algorithms predominantly use rather simple threshold techniques together with statistical approaches. The greatest challenge remains the determination of the optimal thresholds for every test at every location for all possible meteorological conditions.

A rather simple sounding task, after cloudy pixels have been successfully separated from clear ones, is to determine the cloud fraction of an image. The next sections a general definition for cloud fraction is given and difficulties as well as sources of error involved in its determination are discussed. Great part of the information in this sections is taken from Di Girolamo and Davies (1997)

2.3.2 Definition of cloud fraction

Cloud fraction is in general defined as the fractional area coverage of cloud over a particular background domain (Di Girolamo and Davies, 1997; Henderson-Sellers and McGuffie, 1990). This variable is an important parameter in atmospheric science. For example, the quality of model simulations can be evaluated by comparing the cloud fraction of the model to the cloud fraction derived from observations. Furthermore, cloud parameters in climate models like cloud fraction are tuned to obtain the correct radiation balance for the current climate Golaz et al. (2013). In the field of remote sensing and in particular for satellite observations, the above definition is approached by computing the fraction of pixels that contain clouds and are therefore flagged as cloudy. Even if this approach seems reasonable and straight forward, it contains a large number of potentially detrimental error sources.

2.3.3 Sources of error

Following Di Girolamo and Davies (1997), the problems associated with determining the cloud fraction can be put into four main categories: cloud definition, cloud fraction def-

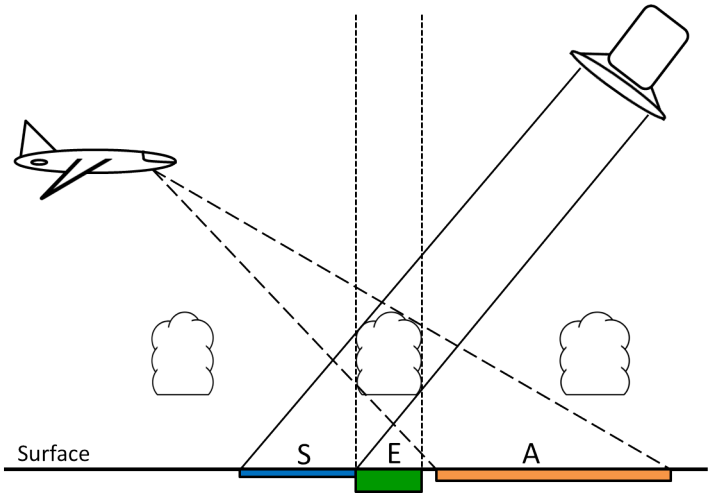

Figure 2.17: Sketch illustrating the projection error in cloud remote sensing depending on distance to the clouds and viewing zenith angle (VZA). Figure redrawn and adapted from Henderson-Sellers and McGuffie (1990).

inition, resolution effects and threshold effects. The most fundamental issue of these, is the actual definition of "what is a cloud". An important characteristic defining a cloud is the presence of liquid water or ice particles, but there is no quantitative boundary for the spatial extent or for the concentration of particles. The lack of a precise cloud definition implicates the absence of a true cloud fraction. This fact makes it difficult to validate any observational estimate of cloud fraction.

Choosing the correct threshold for the algorithm to separate cloudy from clear sky is also linked to the problem of cloud definition. In addition, the threshold itself may needs to be adapted depending on environmental conditions. The method used for adaptation again potentially introduces errors which that can lead to an artificial variation of cloud fraction in space and time.

The last source of error mentioned by Di Girolamo and Davies (1997) is the resolution effect. The size of this error strongly depends on the ratio between the resolution of the instrument and the typical extent of the observed clouds. For example, a resolution of 1 kilometer would be sufficient to get decent results for the cloud fraction in an environment of large stratiform clouds like they appear in the vicinity of a mid-latitude warm front. On the contrary, observing shallow cumulus clouds with diameters of a few hundred meters with the same resolution leads to a significant over-estimation of the cloud fraction. This is due to the fact that pixels are flagged as cloudy even if the subpixel cloud cover is lower than 1. There is a possibility to account for these partially cloudy pixels by making assumptions about the observed clouds such as their size distribution (Coakley and Bretherton, 1982).

A source of error not addressed by Di Girolamo and Davies (1997), originates from the viewing geometry of the instrument. In the case of broken cloud cover the cloud fraction enhances significantly with rising viewing zenith angle (VZA). This effect is illustrated in figure 2.17. For large VZA illustrated by the field of view (FOV) of the aircraft

(A) not only the projected area of the observed cloud increases (orange box) but the sky may seems to be fully overcast because the cloud sides obscure the clear sky between two neighboring clouds. Snow et al. (1985) showed that cloud fraction derived from satellites (S) may also overestimate the earth view cloud fraction (E) due to cloud side effects (Henderson-Sellers and McGuffie, 1990).

In the light of these many possible errors it seems problematic to tackle the task of cloud detection at all, but the importance of clouds for weather and climate on Earth makes it necessary.

3 Methods

3.1 The NARVAL II campaign

The Next generation Aircraft Remote-sensing for VALidation studies (NARVAL II) measurement campaign was carried out in the western tropical Atlantic near Barbados from the 8th to the 31st August 2016. The campaign was lead by the Max Planck Institute for Meteorology (MPI-M) and the University of Hamburg, supported among others by Ludwig-Maximilians-University (LMU) Munich. The goal of the campaign was to get better insight into the physical processes supporting convective self-aggregation. Therefore the contribution of shallow convection and water vapor concentration to low level radiative cooling was examined using remote sensing instruments and dropsondes. The instruments were deployed aboard the research aircraft HALO (High Altitude and LOng range research aircraft) operated by the German Aerospace Center. The instrumentation included for example HAMP (HALO Microwave Package), WALES (Water Vapor Differential Absorption LIDAR) and specMACS (spectrometer of the Munich Aerosol and Cloud Scanner). The data captured by specMACS during the campaign are the basis for this thesis. Therefore, characteristics and specifications of the instrument, which are essential for the correct interpretation of the measurement data will be introduced in the next section.

3.2 Hyperspectral observations with specMACS

Remote sensing is an important tool in atmospheric research for many decades. It provides the possibility to retrieve information about distant objects without being in direct contact with them. One advantage of remote sensing systems is their aerial and temporal coverage. There are a variety of remote sensing methods, which can be grouped into active and passive techniques.

Using an active method means that electromagnetic radiation of a specified wavelength is emitted by the instrument and the backscattered signal is detected by a sensor. Examples for active techniques are LIDAR (Light Detection And Ranging) and RADAR (RAdio Detection And Ranging). Passive methods only measure scattered solar radiation or thermal infrared radiation emitted by objects under investigation.

The specMACS instrument (spectrometer of the Munich Aerosol and Cloud Scanner), operated by the Meteorological Institute of LMU Munich (MIM), is a hyperspectral imaginging spectrometer and therefore a passive remote sensing system. In the following sections the basic principle of hyperspectral imaging is explained and the specMACS instrument is characterized. The generall information about hyperspectral imaging in this

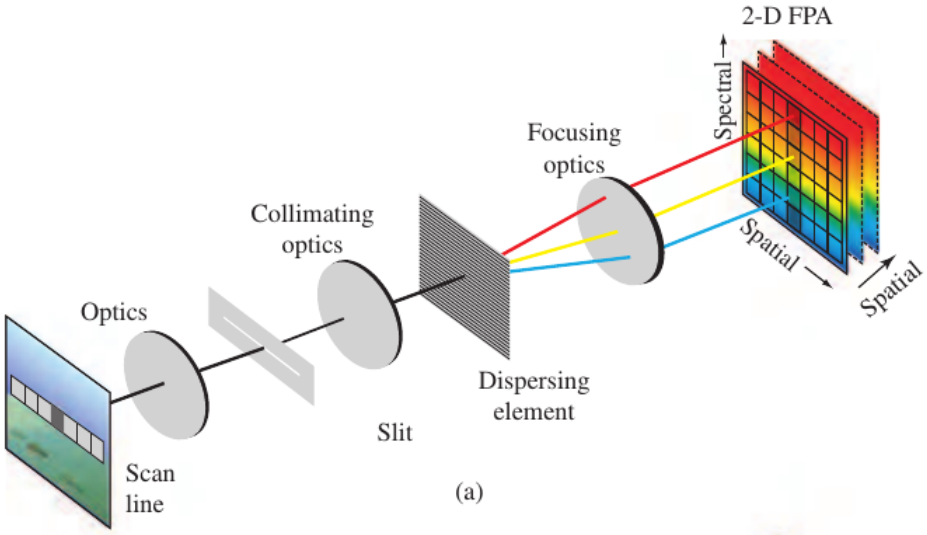

Figure 3.1: Illustration of a slit spectrometer similar to specMACS. Each data frame is composed of one spatial and one spectral dimension. The second spatial dimension can be obtained by scanning the object under investigation. Figure from Manolakis et al. (2016).

section is taken from Manolakis et al. (2016), and details about the specMACS instrument are from Ewald et al. (2016).

3.2.1 Hyperspectral imaging

In a hyperspectral imaging system the incoming radiation is dispersed into the different wavelengths it consists of and projected onto a sensor, which measures the energy for each wavelength band. Therefore, each image captured with a 2D sensor consist of one spatial and one spectral dimension. To get the second spatial dimension the system has to scan the object of interest. This can for example be done by mounting the instrument on an airplane and scaning the ground below by continuously taking images during the airplane moves. The instrument design and the measurement principle as described above is illustrated in figure 3.1.

The spectral information gained by these kind of measurements can then be used to characterize the observed object. A common application is the classification of the Earth's surface. The Normalized Difference Vegetation Index (NDVI) can be used to identify vegetation due to the different reflection of visible and near infrared radiation by chlorophyll. It is also possible to detect man-made materials, like polyester, plastics and building materials, which have a specific spectral signature.

In atmospheric science, hyperspectral imaging is used to retrieve trace gas concentrations, optical thickness clouds and aerosols, cloud phase and effective particle radius (Ewald et al., 2013; Marion et al., 2004). The retrievals for these quantities are generally more complex than for example the classification of vegetation using the NDVI. Lookupt-

	VNIR	SWIR
Detector	SiO2 CMOS	HgCdTe CMOS
Spectral range	417–1016 nm	1015–2496 nm
Spectral bandwidth	typ. 2.5–4 nm	typ. 7.5–12 nm
FOV	32.7°	35.5°
IFOV (across-track)	typ. 1.4 mrad	typ. 3.8 mrad
IFOV (along-track)	typ. 2.0 mrad	typ. 1.8 mrad
Spatial pixels	1312	320
Spectral channels	800	256
Radiometric quantization	12 bit	14 bit
Usable dynamic range	9.5 bit	typ. 11–11.6 bit
Max. frame rate	145 Hz	103 Hz
Temp. control	uncooled	200 K

Figure 3.2: Technical specification of the VNIR and SWIR camera of the specMACS instrument. Figure from Ewald et al. (2016)

abels have to be calculated using radiative transfer simulations, where different parameters like solar zenith angle or cloud optical thickness are varied. The masurements are then compared to the simulations to obtain the investigated quantity. A famous retrieval for optical thickness and effective droplet radius of stratiform clouds was developed by Nakajima and King (1990) comparing the cloud reflectance at 0.75 and 2.16 μm wavelength. This approach works well for scenes, that can be approximated well as a one-dimensional problem, such as optically thick stratiform clouds. However, as soon as three dimensional effects like shadows are involved, the retrieval delivers ambiguous results (Ewald et al., 2013). This example shows the advantages as well as the challenges associated with the use of hyperspectral imaging techniques in the field of atmospheric research.

3.2.2 Instrument characterization

The specMACS instrument is a hyperspecrtal imager, which consists of two spectral cameras, covering a wavelength range from 400 to 2500 nm. One camera covers the visible and near infrared part of the spectrum (VNIR) from 400 to 1000 nm, and the second measures in the shortwave infrared spectrum (SWIR) from 1000 to 2500 nm. The spectral bandwidth of the VNIR camera has a typical range between 2.5 and 4 nm, and the bandwidth of the SWIR camera is typically 7.5 to 12 nm. Further specifications of the instrument can be found in the table 3.2, and an image of both cameras during ground-based operation is shown in figure 3.3.

The sensor of the SWIR camera, which is most relevant for this thesis, has 320 spatial and 256 spectral pixel. It has a field of view (FOV) of 35.5° which corresponds to a swath of 6.4 km at a vertical distance of 10 km. The resolution of a single pixel at the same distance is 18 m in along-track and 38 m in across-track direction. A typical spectrum measured by the SWIR camera is shown in figure 3.4.

Figure 3.3: Picture of the specMACS instrument consisting of the VNIR and SWIR camera during ground-based operation. Figure from Ewald et al. (2016)

A common measure of the technical quality of a measurement is the signal-to-noise ratio (SNR). This quantity is used in this thesis to flag measurements, that are of too low quality to be interpreted properly. The SNR of the SWIR camera refers to the dark-current-corrected signal S_0. S_0 is obtained by subtracting the dark-current signal S_d from the raw signal S ($S_0 = S - S_d$) which is the output of each pixel in form of a digital number (DN). The noise $\sigma_{\mathcal{N}}$ of the SWIR camera signal is defined as the standard deviation of 500 consecutive measurements (camera frames) and follows the empirical relation

$$\sigma_{\mathcal{N}} = \sqrt{0.015\, S_0 + 4.77^2} \tag{3.1}$$

Using the so defined standard deviation, the SNR is calculated like

$$SNR = \frac{S_0}{\sigma_{\mathcal{N}}} \tag{3.2}$$

This equation can be applied to every spectral channel of each spatial camera pixel. Spectral channels in regions of strong atmospheric absorption or at large wavelengths (i.e. $> 2\ \mu m$) receive less radiation than other channels and have therefore generally lower SNR.

specMACS has been operated during ground based campaigns like ML-CIRRUS as well as aboard the HALO research aircraft during airborne campaigns like ACRIDICON-CHUVA, NARVAL II and NAWDEX. During NARVAL II and NAWDEX specMACS was mounted at the rear of HALO viewing vertically downward to observe clouds from above.

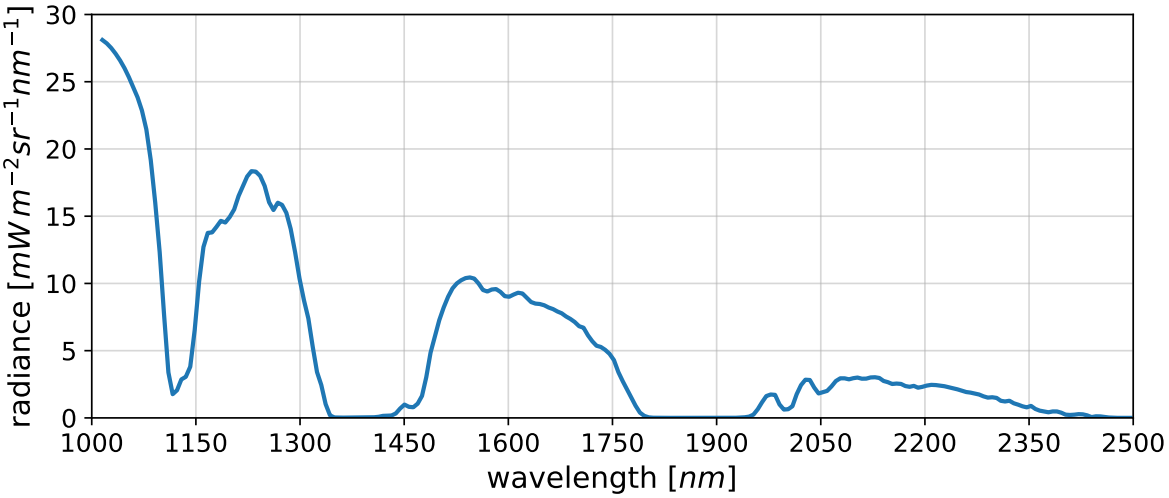

Figure 3.4: Typical spectrum measured by the SWIR camera. The strong absorption bands at 1125 nm, 1375 nm and 1900 nm are due to water vapor absorption. The spectrum was simulated with libRadtran (Mayer and Kylling, 2005). For the exact setup see table 6.2.

3.3 Radiative transfer simulations with libRadtran

In this thesis a large number of radiative transfer calculations was performed using the library for Radiative transfer (libRadtran) (Mayer and Kylling, 2005). The calculations were used to simulate the influence of water vapor concentration on the spectrum measured by the SWIR camera and to validate the developed algorithm against model data. The basic setup for these calculations and methods for simulating the spectra measured by the SWIR camera are presented in this section.

3.3.1 Basic setup

For the case of optically thick clouds with a horizontal extend of a few kilometers a one dimensional solution of the radiative transfer yields decent results. To model these cases the 1D Discrete Ordinate Radiative Transfer solver (DISORT) (Stamnes et al., 1988; Buras et al., 2011) from libRadtran was used together with the REPTRAN (representative wavelength approach) band parametrization for molecular absorption and its coarse resolution option. DISORT solves the radiative transfer equation under the assumption that variation of atmospheric constituents and cloud properties only occur in the vertical direction. As the measurements during NARVAL II exclusively took place over the Atlantic ocean, the BRDF (Bidirectional Reflectance Distribution Function) of the ocean surface was parameterized using the method described by Cox and Munk (1954). The calculated spectrum ranges from 1000 to 2500 nm with a spectral resolution of 15 cm^{-1} equidistant in wavenumber, corresponding to a wavelength resolution of $1.5 - 9.34$ nm within the used wavelength range.

Clouds were assumed to be homogeneous, meaning effective radius (r_{eff}) and liquid water content (LWC) are constant throughout the cloud. The cloud base was set to 600 m – a typical value for trade wind cumuli according to Siebesma (1998) – and the vertical extent to 200 m. Together with a LWC of 1 gm^{-3} and an effective radius of 10 μm the model cloud has an approximate optical thickness of $\tau = 30$ following equation (2.15). To model the geometry during NARVAL II the virtual sensor was placed at an altitude of 10 km looking vertically downward onto the cloud and the solar zenith angle (SZA) was set to 0°. The different input parameters and settings for these 1D calculations are summarized in tabular form in the appendix (see chapter 6).

Beside the 1D simulations also 3D radiative transfer simulations were conducted, to obtain a data set to validate the performance of the developed cloud detection algorithm. For this purpose the 3D solver MYSTIC (Monte Carlo code for the physically correct tracing of photons in cloudy atmospheres) (Mayer, B., 2009) was used with input of realistic clouds from a large eddy simulation (LES) model. The MYSTIC and LES simulations were conducted by Fabian Jakub. MYSTIC solves the radiative transfer equation (2.4) exactly without any further assumptions, by tracing each photon on its way through the atmosphere. The detailed setup for the MYSTIC simulations can be found in table 6.4 in the appendix.

3.3.2 Simulating specMACS

To explicitly simulate the specMACS instrument the spectra calculated with libRadtran are convolved with a slit function for the respective sensor. Ewald et al. (2016) characterized the spectral response function for each spectral channel and calculated full width half maximum (FWHM) values for a representative Gaussian-shaped function. These FWHM values where used to set up a Gaussian spectral response function for each of the 256 spectral channels of the SWIR camera yielding the needed slit function.

This method was used to simulate reference spectra for the cloud retrieval, investigate the sensitivity to water vapor concentration, and validate the retrieval against model data as described in following sections.

3.4 Cloud detection using absorption by water vapor

The main goal of this thesis was to develop an efficient and reliable algorithm to detect clouds in the data captured by the specMACS instrument during the NARVAL II campaign. The major challenge was to detect the clouds even in the presence of sunglint, where brightness can not be used to distinguish cloudy from clear sky pixels. Depending on the wind speed the reflectance of the oceans surface can be significantly higher as the one of clouds. If only a brightness threshold is used, the cloud detection will not yield decent result. Either a great part of sunglint contaminated clear pixels is classified as cloud when the threshold is set too low, or the amount of clouds is dramatically underestimated if the threshold is set too high, to make sure that the sunglint is masked out. This

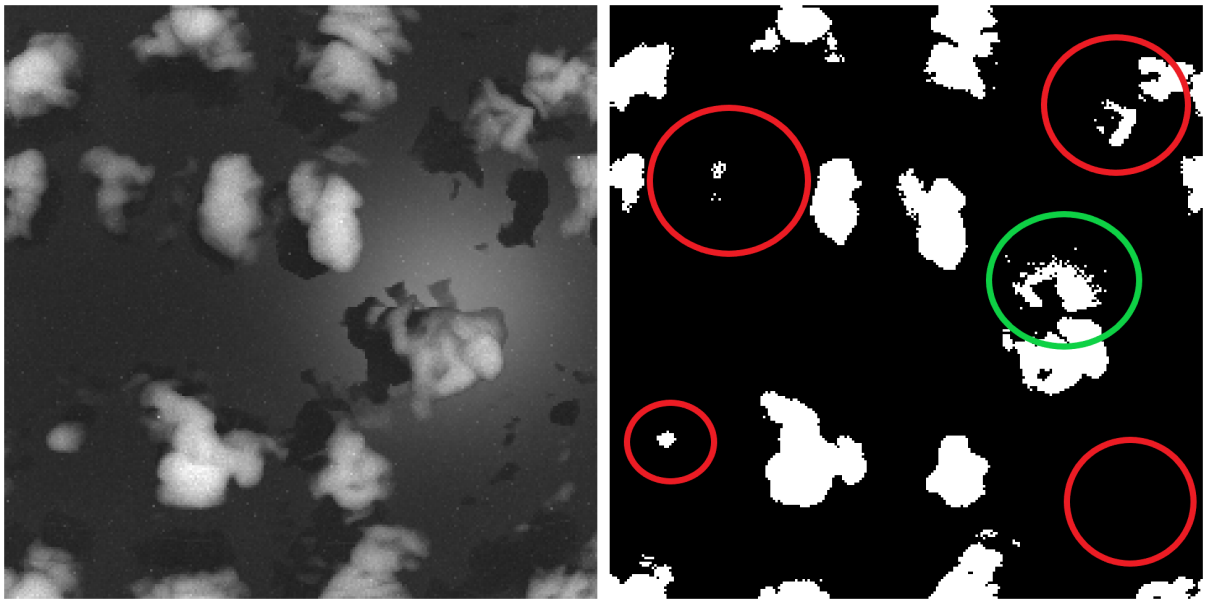

Figure 3.5: Left: Image of 3D MYSTIC panorama simulation using ocean BRDF by Cox and Munk (1954) with a wind speed of 2 ms^{-1}. The clouds were taken from a LES (Large Eddy Simulation) model. Right: Brightness threshold applied to the left image to distinguish surface and cloud pixel. Location of sunglint is highlighted by the green circle, areas where cloud detection obviously fails are marked by red circles. MYSTIC simulation and figure by Bernhard Mayer.

threshold problem is shown in figure 3.5. Here the threshold is still chosen too low (green circle), but several cloud areas are already wrongly classified as clear (red circles). Due to the measurement geometry – specMACS was pointed nearly vertically downward from the plane – and the low solar zenith angle (SZA) in the tropics, a significant fraction of measurements during NARVAL II are contaminated with sunglint in each research flight (RF). To overcome this problem a method based on the absorption of water vapor was developed which is described in the following sections.

3.4.1 Basic concept

The concept of using water vapor absorption to detect clouds was already proposed by Gao and Kaufman (1995). They used the strong short wave infrared (SWIR) absorption of water vapor to detect cirrus clouds from satellites. In an environment without cirrus clouds, solar radiation reaches the low regions of the troposphere before it is reflected by low-level clouds or Earth's surface. It then travels back through the entire atmosphere before it is detected by the satellite. In the presence of cirrus clouds a considerable amount of the solar radiation is already reflected in the upper troposphere. Due to the significantly shorter light path, and therefore lower optical thickness of water vapor, there is less absorption in the presence of cirrus clouds. This difference is further enhanced by the much higher concentrations of water vapor near the surface, which results in even lower

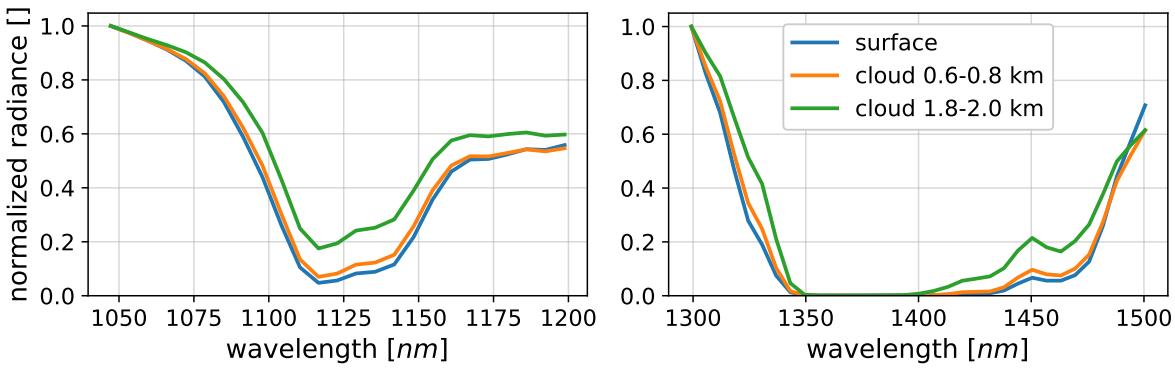

Figure 3.6: Simulated spectra of the SWIR camera using libRadtran DISORT solver. The figure shows the water vapor absorption bands at 1125 (left) and 1375 nm (right) for three cases: surface without cloud (blue), cloud at $0.6 - 0.8$ km (orange) and cloud at $1.8 - 2.0$ km (green). The spectra are normalized to their respective maximum within the shown wavelength intervals to make the difference in absorption visible.

radiance measurements when no cirrus clouds are present.

So far this method was exclusively used to detect high clouds like cirrus, but it is possible to apply the basic idea of this concept for the detection of shallow cumulus clouds above the tropical ocean. When the sunlight is scattered at ocean's surface it travels a longer path and penetrates the atmosphere close to the surface with higher water vapor concentrations than light scattered by clouds a few hundred meters above. Nevertheless the path difference is significantly lower than between cirrus and no-cirrus scenes, leading to smaller radiance differences. Additionally only the weak absorbing wings of the strong water vapor bands can be used, as nearly all the radiation is absorbed in their center. To detect the small radiance difference between cloudy and clear sky pixels, high resolution and high precision measurements like provided by specMACS are necessary.

Figure 3.6 shows two details from three simulated spectra for the SWIR camera in regions of strong water vapor absorption, centered at roughly 1125 and 1375 nm. The spectra are normalized to their respective maximum radiance within the considered wavelength interval, because the relative difference between the maximum radiance and the radiance within the absorption band provides information about the amount of absorption. As expected, the highest absorption occurs if no cloud is present (blue) and the light is scattered on the oceans surface. The absorption for a very low cloud (orange) is slightly smaller than for the clear sky case, whereas the absorption reduces significantly if the cloud is located at higher levels (green).

The basic approach to evaluate the absorption by water vapor from spectral radiances measured by the SWIR camera and the manner in which this information is used to identify clouds, is described in the following section.

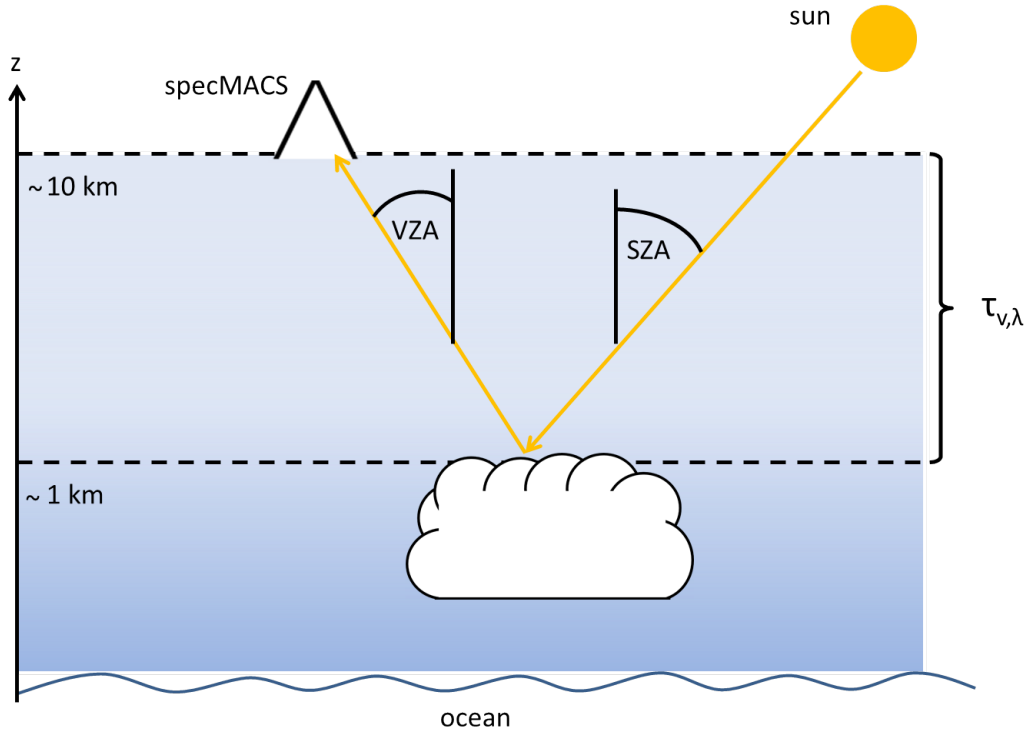

Figure 3.7: Sketch of measurement geometry during Narval II campaign. Solar radiation enters atmosphere under solar zenith angle (SZA) is reflected on top of a cloud and received by specMACS under a viewing zenith angle (VZA). the blue shading illustrates the presence of water vapor and its vertical gradient. $\tau_{v,\lambda}$ denotes the vertical optical thickness of water vapor at a certain wavelength (λ) between cloud top and the elevation of the instrument.

3.4.2 Implementation and its physical basis

As explained before the differences in absorption between light scattered by a low-level cloud or by the oceans surface is small. Therefore a reference is needed to compare the measured spectra to and then decide whether the spectrum belongs to a cloud or the surface. This comparison is set up as follows: First a reference SWIR camera spectrum is simulated with libRadtran for the geometry shown in figure 3.7. The sensor is placed at an altitude of 10 km, which is a typical cruise altitude of the research aircraft. Viewing zenith angle (VZA) and solar zenith angle (SZA) are chosen to be zero degrees. Pressure, temperature and trace gas concentrations were taken from the tropical standard atmosphere (Anderson et al., 1986). One spectrum is simulated with molecular absorption and a second, switching off molecular absorption. These spectra are convolved with the slit function of the SWIR camera to explicitly simulate the instrument as described in section 3.3.2. The result of these simulations is shown in the upper panel of figure 3.8. Further details about the calculation of the reference spectra can be found in table 6.2 in the appendix.

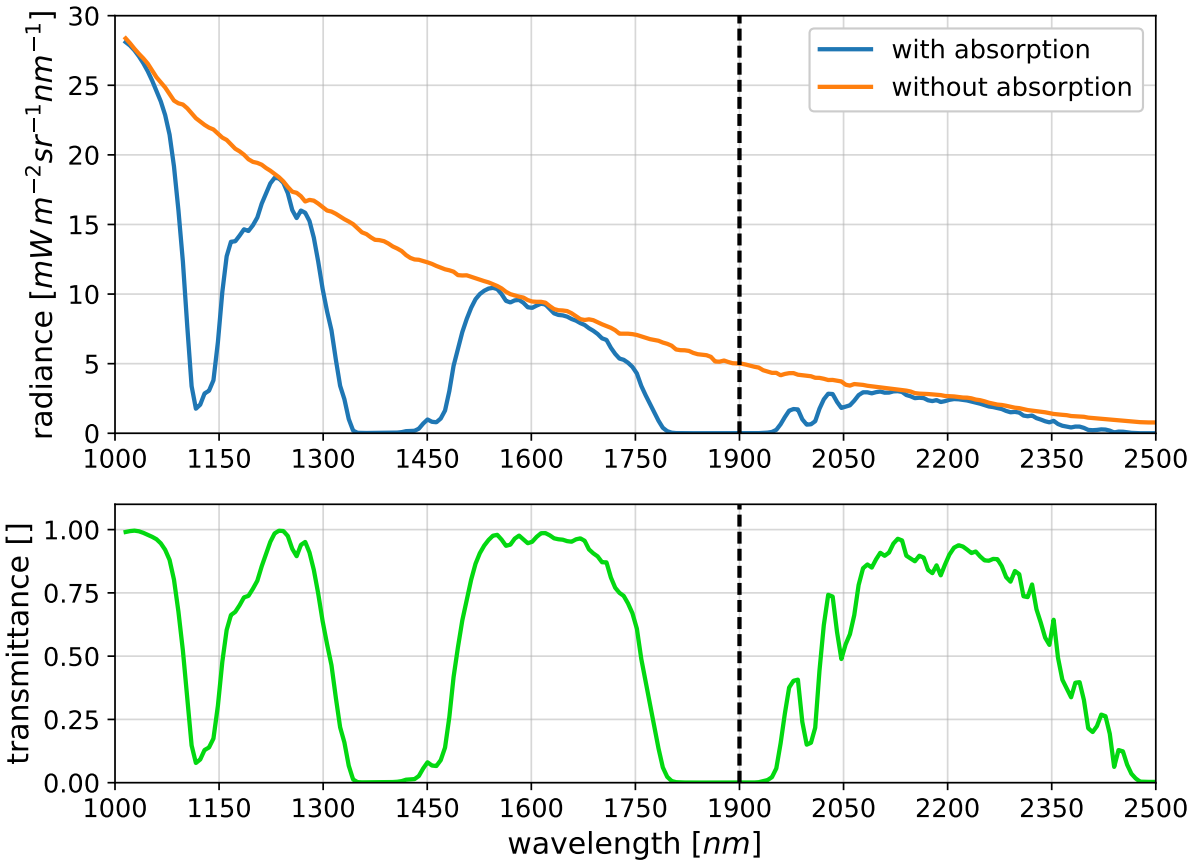

Figure 3.8: Upper panel: Simulated reference spectra with (blue) and without molecular absorption (orange). Lower panel: Reference spectral transmission obtained using equation (3.3) with the spectra in the upper panel. Only wavelengths lower than indicated by the dotted vertical line are used in th cloud retrieval.

From these two spectra the spectral transmittance $T(\lambda)$ of the reference spectrum can be calculated following equation (2.9)

$$T(\lambda) = \frac{L_{abs,\lambda}}{L_{noabs,\lambda}} = \exp\left[-\tau_{path,\lambda}\right] = \exp\left[-\left(\frac{\tau_{v,\lambda}}{\cos(sza)} + \frac{\tau_{v,\lambda}}{\cos(vza)}\right)\right] \tag{3.3}$$

$L_{abs,\lambda}$ denotes the spectral radiance simulated with molecular absorption, $L_{noabs,\lambda}$ the one without molecular absorption. $\tau_{path,\lambda}$ represents the spectral optical thickness along the light path. $\tau_{v,\lambda}$ is the vertical optical thickness of water vapor between the scattering cloud/surface and the altitude of the sensor illustrated in figure 3.7. As SZA and VZA were set to zero in the reference simulation and $\cos(0) = 1$, the total optical thickness along the light path is simply two times the vertical optical thickness ($\tau_{path,\lambda} = 2\,\tau_{v,\lambda}$). This formulation contains the assumption that the optical thickness of water vapor above the cruise altitude of the plane is small for the flanks of the water vapor vapor bands and the relatively weak band at 1125 nm (see figure 3.6). The center of the strong

absorption bands at 1375 and 1900 nm are not of interest as they do not contain any information because all the radiation is absorbed (see figures 3.6 and 3.8). Furthermore it is important to mention that τ_λ is not the true monochromatic optical thickness. The reference spectrum was calculated at a certain resolution, which yields averaged radiances over spectral intervals. Additionally this spectrum is convolved with a Gaussian slit function, which again averages the radiances. Therefore τ_λ should be seen as an weighted average optical thickness over irregular wavelength intervals $\Delta\lambda$.

The result of this transmittance calculation is shown in the lower panel of figure 3.8. The strong absorption bands due to the vibrational overtones of water vapor can be identified at roughly 1125, 1375 and 1900 nm wavelength. The two consecutive dips above 2000 nm are due to absorption by CO_2. This transmission spectrum serves as a reference for the spectra measured by the SWIR camera of specMACS. As the presented cloud detection approach only uses absorption by water vapor, wavelength above 1900 nm are excluded from further considerations.

The comparison between the simulated reference spectra and the measurements is realized in form of a least square fit. This fit is intended to reconstruct the measured spectra from the simulated reference spectrum without absorption and the corresponding transmittance. The multiplication of those yields the reference spectrum with molecular absorption. To reconstruct spectra with arbitrary brightness and transmittance two fit parameter are introduced in the following way

$$L_{meas,\lambda} = a \cdot L_{ref,noabs,\lambda} \cdot (T_{ref,\lambda})^x \tag{3.4}$$

$L_{meas,\lambda}$ denotes the measured radiance at wavelength λ, $L_{ref,noabs,\lambda}$ the spectral reference radiance without absorption and $T_{ref,\lambda}$ the spectral reference transmittance. The parameter a scales with the brightness of the measured spectrum. The exponential fit parameter x scales the transmittance and is a measure of absorption. This scaling can be related to the optical thickness along the light path

$$(T(\lambda))^x = (\exp[-\tau_{path,\lambda}])^x = \exp[-\tau_{path,\lambda} \cdot x] \tag{3.5}$$

Therefore x directly scales the optical thickness. For $x > 1$ the absorption in the measured spectrum is larger than in the reference spectrum, whereas the opposite is true for $x < 1$. Figure 3.9 shows the variation of the reference transmittance for different values of x. In fact equation (3.5) is only physically correct if $x = x(\lambda)$ because the change in optical thickness is generally different for each wavelength. This dependence on wavelength of both, x and a, is not considered in the fit. Therefore both quantities rather represent average measures for the brightness and optical thickness – in the way that they minimize the deviation between reference and measurement – relative to the reference spectrum than solid physical quantities.

The fitting algorithm was implemented using the Python library Theano. To save computational time and exclude the absorption by CO_2 as mentioned before, only wavelength between 1015 and 1900 nm are included in the fit. The wavelength channels between 1000 and 1015 nm are excluded due to higher instrument inaccuracy in this region. Before the fit was applied, the measurement data had been smoothed using a 3x3

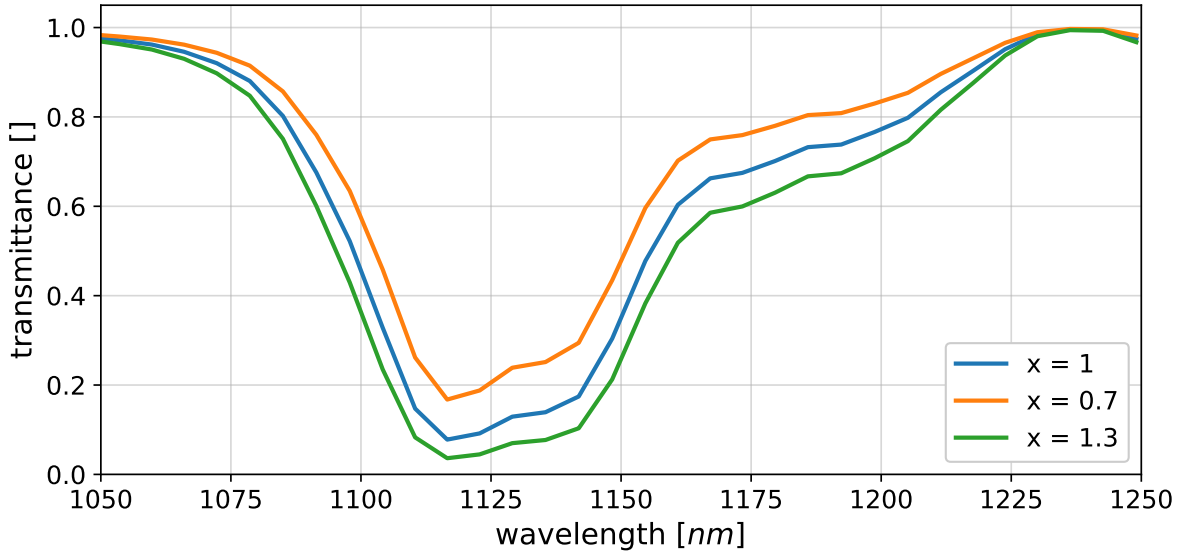

Figure 3.9: Variation of the reference spectral transmission applying values of the fit parameter x according to (3.5). The wavelength interval between 1050 and 1250 nm is shown for $x = 1.3$ (green) $x = 1$ (blue) and $x = 0.7$ (orange).

Gaussian smoothing kernel. This was done to reduce irregularities in the measured spectra and receive consistent results. In the next section the determination of the threshold using the fit parameter x will be described. Hereafter x will also be referred to as *path parameter* as it is related to the length of the light path.

3.4.3 Threshold determination

To use the fit parameter x as a measure for the presence of clouds a threshold has to be defined. For values of x larger than the threshold the measurement is assumed to originate from light reflected at the surface and is therefore classified as clear sky or non-cloudy. For $x \leq$ threshold, it is assumed that the light was scattered somewhere above the surface, due to the presence of a cloud. Those pixels are therefore classified as cloudy. The concentration and vertical distribution of water vapor in the tropical standard atmosphere, which was used to calculate the reference spectrum (see previous section), does not represent the actual environment during the measurement. Therefore, the threshold can in general not be determined exactly by radiative transfer simulations but has to be manually tuned using a partly cloud covered scene from the measurements.

An undesirable property of the measurements is, that there is no "truth" to compare the retrieved cloud mask to, like it is possible for model data. The best estimate for the threshold is therefore generated by visual inspection of the camera images and contour plots of the cloud mask drawn onto the camera image. The determined threshold is no constant value but depends on SZA and VZA because the light path and therefore the optical thickness increases with increasing SZA and VZA. Combining equations (3.5) and

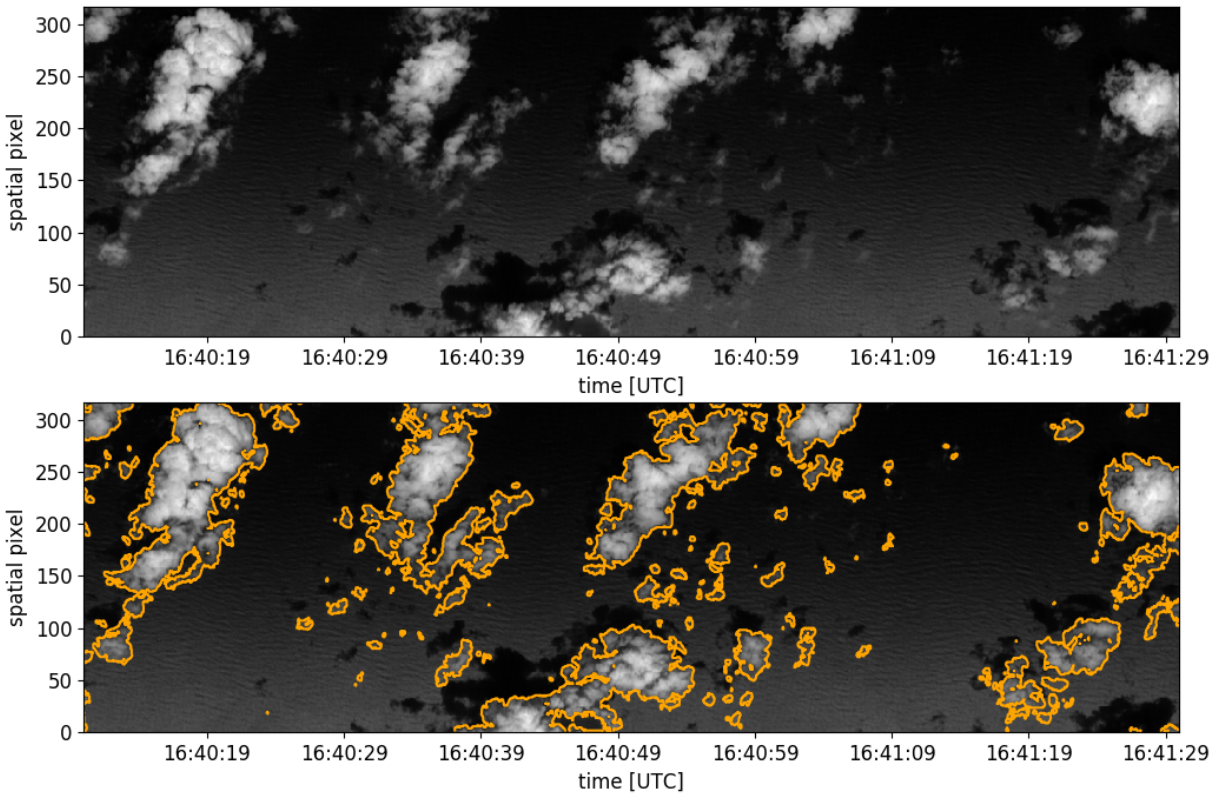

Figure 3.10: Scene used to tune the threshold captured by the SWIR camera during RF6 starting at 16:40 UTC. Upper panel: Grayscale image of the 1600 *nm* radiance. Lower panel: Contour plot using the cloud mask obtained by applying the tuned threshold to the fit result for the parameter x. The SZA for this scene is approximately 20°.

(3.3), the threshold transmittance can be written as

$$\exp\left[-\tau_{thres}(sza, vza, \lambda)\right] = \exp\left[-\left(\frac{\tau_{v,\lambda,ref}}{\cos(sza)} + \frac{\tau_{v,\lambda,ref}}{\cos(vza)}\right) \cdot x_{thres,std}\right] \tag{3.6}$$

$\tau_{thres}(sza, vza, \lambda)$ denotes the threshold optical thickness as a function of SZA, VZA and wavelength λ. Its value is obtained by weighting the reference vertical spectral optical thickness $\tau_{v,\lambda,ref}$ by the cosine of the SZA and VZA, and multiplying it by the reference threshold fit parameter $x_{thres,std}$. In this context the subscript *std* stands for the threshold at $sza = vza = 0$. As mentioned before, the fit parameter x does not depend on wavelength. Therefore, all $\tau_{v,\lambda,ref}$ are scaled by the same value. In a next step the goal is to determine the relation between the standard threshold and the threshold of the fit parameter x for arbitrary SZA and VZA. Taking the natural logarithm of equation (3.6) yields

$$\tau_{thres}(sza, vza, \lambda) = \left(\frac{\tau_{v,\lambda,ref}}{\cos(sza)} + \frac{\tau_{v,\lambda,ref}}{\cos(vza)}\right) \cdot x_{thres,std} \tag{3.7}$$

Dividing equation (3.7) by $2\,\tau_{v,\lambda,ref}$, which is equal to the total optical thickness along the light path for $sza = vza = 0$, gives the threshold for the fit parameter x depending on SZA and VZA

$$\underbrace{\frac{\tau_{thres}(sza, vza, \lambda)}{2\,\tau_{v,\lambda,ref}}}_{=: x_{thres}(sza,vza)} = \frac{1}{2}\left(\frac{1}{\cos(sza)} + \frac{1}{\cos(vza)}\right) \cdot x_{thres,std}$$

$$\boxed{x_{thres}(sza, vza) = \frac{1}{2}\left(\frac{1}{\cos(sza)} + \frac{1}{\cos(vza)}\right) \cdot x_{thres,std}} \tag{3.8}$$

$x_{thres}(sza, vza)$ denotes the threshold for x for arbitrary SZA and VZA. Although the ratio of threshold and reference optical thickness depends on wavelength, $x_{thres}(sza, vza)$ does not. The reason is again, that the fit parameter x does not depend on wavelength but scales all wavelengths equally. Therefore, also the threshold can and must not depend on wavelength. The boxed result of equation (3.8) is important, as it defines how the threshold for the actual conditions can be calculated from the standard threshold $x_{thres,std}$.

As described above, the standard threshold is set by visual inspection. This is realized by selecting an appropriate scene, which contains clouds of different sizes and structures as well as sunglint. Of course this selected scene does in general not fulfill the requirement $sza = vza = 0$ of the standard threshold. This is also the case for the scene shown in figure 3.10, which was selected selected to tune the threshold for the NARVAL II specMACS data. Here the SZA is roughly 20°. Therefore, equation (3.8) has to be rearranged to calculate the standard threshold from the threshold tuned to the selected scene

$$x_{thres,std} = 2\left(\frac{\cos(sza_t)\,\cos(vza_t)}{\cos(sza_t) + \cos(vza_t)}\right) x_{thres}(sza_t, vza_t) \tag{3.9}$$

The index t denotes the respective values of SZA and VZA for the tuned threshold. To be able to calculate the threshold for each measurement, SZA and VZA have to be known. The BAHAMAS instrument aboard the HALO research aircraft provides data on aircraft position, altitude and flight geometry (e.g pitch and roll angle) at a frequency of 100 Hz. These data can be used calculate the VZA of the SWIR camera as well as the local SZA. To calculate the SZA from position, altitude and time, the Python library PyEphem was used, which provides high precision astronomical computations.

For the scene shown in figure 3.10 the threshold was tuned in following way: First the least square fit with the fit function (3.4) was applied to the scene, to retrieve the fit parameter a and x. In a second step the dark regions of the scene were masked using a threshold for the brightness parameter a. The reasoning for this will be given in the next section. Now different thresholds for x were tested. Thereby the value of the threshold was corrected for the VZA of each pixel before it was applied to the image. The optimal threshold was determined to be $x_{thres}(sza_t, vza_t = 0) = 0.8358$. This value was corrected according to equation (3.9) with $sza_t = 20.6°$ yielding a standard threshold of $x_{thres,std} = 0.81$. This threshold will be slightly changed in section 3.4.6.

3.4.4 Brightness and noise mask

In cases where the sunglint does not enhance the reflectance of the oceans surface within the field of view (FOV) of the SWIR camera or clouds shade the surface, the fitting approach presented in the previous section fails. It was observed that the fit parameter x was generally underestimated in those underexposed regions leading to a considerably high false detection rate for clouds. The cause for this failure is on the one hand that the signal-to-noise ratio (SNR) for dark regions is small and the measurements are possibly of to low quality to be interpreted properly. On the other hand the light received by the camera in regions with low surface reflection is due to light scattered between the instrument and the surface. As the scattering by air molecules is very small for SWIR radiation, scattering is only efficient in the presence of aerosol. In fact considerable amounts of aerosol where observed during NARVAL II, which originated for instance from Saharan-dust transported over the Atlantic. To overcome this problem, dark regions need to be masked out to avoid false detection.

The first measure to identify dark regions is the signal-to-noise ratio (SNR) of the SWIR camera, which was described in section 3.2.2. For each measurement an average SNR is calculated for the flanks of the water vapor absorption bands and compared to a threshold. This threshold was set to 40 which is a rather low value. The reason for this choice is the dependence of the SNR on the integration time (exposure time) of the camera. For the same scene but different exposure times the SNR fluctuates significantly which could result in wrongly masking a cloudy pixel as noise if the threshold is set to high. This would mean that the retrieved cloud mask potentially depends on the exposure time which would be a undesirable issue. Additionally it turned out that the SNR mask does not perform well for cloud shadows.

Therefore, the brightness fit parameter a obtained from the fit, is used as a second measure mask dark pixels. This value is based on the actual brightness of the measured spectrum and independent of integration time. The threshold was also estimated by visual inspection and set to $a = 0.62$. It was payed great attention to set the threshold low enough to avoid masking of clouds and high enough to reliably mask shadows and dark regions. As brightness is also a simple but effective measure to detect clouds in front of a dark background, this brightness mask is used as a cloud mask when no sunglint is present. How sunglint contaminated measurements are separated from dark background will be explained in the next section.

3.4.5 Sunglint simulation

Although a large fraction of the specMACS data collected during NARVAL II campaign is contaminated by sunglint, for large SZA in the morning and evening hours the reflectance of the ocean surface is small. In these cases it is possible to use the above described brightness cloud mask instead the approach using water vapor absorption. It is useful to do so, as the water vapor cloud mask loses accuracy for large SZA due to 3D effects in the radiative transfer. If the sun is at low elevation clouds can throw shadows on themselves or neighboring clouds. Radiation from these shaded regions reaching the camera sensor

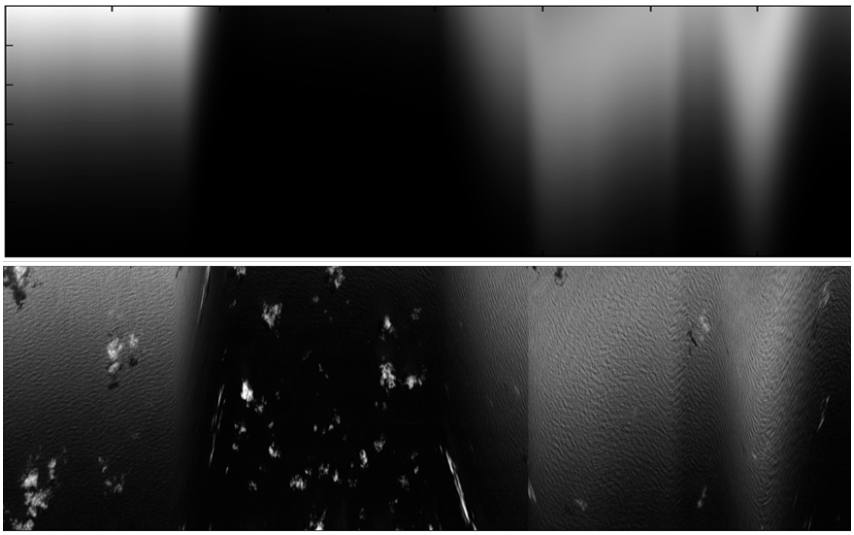

Figure 3.11: Comparison of the sunglint simulation (upper panel) with the radiance at 1600 nm measured by the SWIR camera (lower panel). The scene was captured during research flight 6 between 17:07 and 17:09 UTC.

traveled a longer path than illuminated cloud regions, which is due to multiple scattering. Therefore, the threshold adaptation which assumes 1D clouds and simple reflection at cloud top, can not account for these cases. As a result shaded cloud regions are possibly labeled as non-cloudy because of the higher absorption resulting from the longer light path.

To be able to decide which cloud mask approach is appropriate for each camera frame, the ocean reflectance was simulated using the BRDF parametrization by Tsang et al. (1985). A required input parameter for this simulation is the relative azimuth angle between the viewing direction of each pixel of the SWIR camera and the solar azimuth angle. For this purpose the viewing vector of each pixel and each measurement is transformed to a local horizon coordinate system in the following way

$$\vec{p} = (\sin(act),\, \sin(alt)\cos(act),\, \cos(alt)\sin(act)) \tag{3.10}$$

$\vec{p}$ denotes the viewing vector in the local horizon coordinate system, act the across-track viewing angle of the pixel, and alt the along-track angle. The vector $\vec{s}$ of the sun's position is determined by

$$\vec{s} = (\sin(sza)\cos(azi),\, \sin(sza)\sin(azi),\, -\cos(sza)) \tag{3.11}$$

SZA describes the solar zenith angle as before and AZI the solar azimuth angle. The three entries of the local horizon coordinate system are [north, east, down], whereby the down component is similar to a $-z$-axis. The position of the sun for the respective measurement has been calculated using BAHAMAS position data together with the PyEphem library.

These two vectors of the sun's position and the viewing direction of the camera pixels are then projected on the north-east-plane to calculate the relative azimuth angle between

them. Together with the VZA and SZA all input parameter are available except the wind speed. As the wind speed is an unknown variable it introduces an uncertainty in the reflectance calculation. Having a look at figure 2.7, it is useful to choose a high wind speed to make sure that the reflectance at high relative azimuth angles is not underestimated. Several test calculations revealed that a wind speed of 5 $m\,s^{-1}$ is a good approximation for many research flights, especially for RF6 which will be further examined at a later stage.

The BRDF parametrization by Tsang et al. (1985) is contained in liRadtran package as C-code. This function was incorporated in a Python program with the help of a C-Wrapper. The final result is the ocean reflectance for each pixel and each measurement during a whole research flight. The result of such a simulation is shown in figure 3.11, where the ocean's reflectance changes rapidly due to course corrections of th aircraft. These data are subsequently used to evaluate a sunglint mask which discriminates the measurements in sunglint contaminated and dark background. This is done by applying a reflectance threshold of 0.005, meaning that pixels with surface relectance higher than 0.5% are labeled as sunglint contaminated. Choosing a low threshold is necessary to prevent errors due to the uncertainty in wind speed and make sure that regions classified as dark are actually dark in the measurements. The best estimation for the cloud mask is finally generated by merging the brightness and water vapor cloud mask according to the sunglint mask.

3.4.6 Water vapor variability and threshold adaptation

A big challenge in using water vapor absorption for cloud detection arises from the high temporal and spatial variability of water vapor concentration. From one research flight (RF) to the next or even during one RF, the water vapor concentration can vary significantly as the flight time amounts up to 10 hours and distances of nearly 10000 km are traveled. Figures 3.12 and 3.13 show the integrated column water vapor concentration for RF6 and RF7 respectively. During RF6 the concentration shows rather low variability along the flight track and amounts roughly $1.2 \cdot 10^{23}\ cm^{-2}$. For RF7 the situation is considerably different. The water vapor concentration along the flight track is more variable and reaches values as large as $2 \cdot 10^{23}\ cm^{-2}$, which is nearly twice the concentration during RF6.

A strong change in water vapor concentration implicates a strong change in absorption, which can cause a failure of the cloud mask. When the water vapor concentration is lower than in the scene used to tune the threshold, light reflected on the ocean's surface may experience less absorption than light scattered by a low cloud in the reference environment. This means, that clear pixels would be classified as cloudy using the reference threshold. Reversely, water vapor concentrations higher than the reference would lead to a underestimation of the cloud amount, as light scattered by a cloud would have experienced more absorption than in the reference scene and would therefore be classified as non-cloudy.

To overcome the problem of the the water vapor variability the threshold needs to be adapted according to the actual concentration of the environment at the place and time

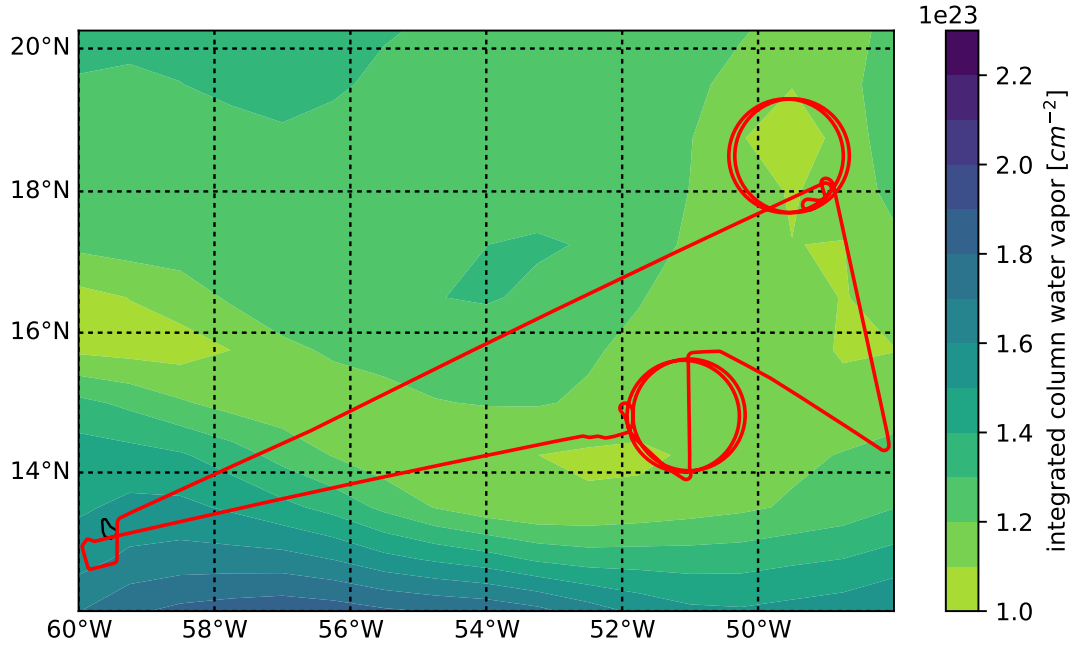

Figure 3.12: Integrated column water vapor number density between 0 and 10 km for reasearch flight 6. Water vapor concentration was calculated from ECMWF ERA-Interim data (Dee et al., 2011) from 12 UTC reanalysis on 19. August 2016. The red line indicates the flight track of the HALO research aircraft.

of the measurement. To do so the water vapor concentration needs to be known. For this purpose, meteorological data from the European Center for Medium-Range Weather Forecasts (ECMWF) ERA-Interim reanalysis (Dee et al., 2011) were used to calculate the number density of water vapor. ERA-Interim data are freely available with a horizontal resolution of ∼80 km and 60 vertical levels up to a pressure of 0.1 hPa. Reanalysis are available in steps of 6 hours starting from 00 UTC. Forecasts with time steps of 3 hours are available starting at 00 and 12 UTC every day. In this thesis only reanalysis data were used. Surface and pressure level data were combined to be able to calculate profiles of water vapor number density. ERA-Interim reanalysis were downloaded for each RF, spanning its entire spatial and temporal extension as can be seen in figures 3.12 and 3.13.

To evaluate the dependency of the threshold on water vapor concentration, a large number of ERA-Interim water vapor profiles from selected RFs was calculated. The chosen RFs span a large range of water vapor concentrations to cover all possible situations. Beside these profiles, also a profile for the scene used for threshold tuning was computed by interpolation in space and time. All profiles were then used as input for radiative transfer simulations. The libRadtran DISORT solver, together with a model cloud between 0.6 and 0.8 km, was used to simulate the SWIR camera measurements for the different profiles (see table 6.3 for the complete setup). To these simulated spectra, the least square fit according to equation (3.4) was applied, to model the response of the threshold due to water vapor variation. The resulting fit parameter x was then plotted

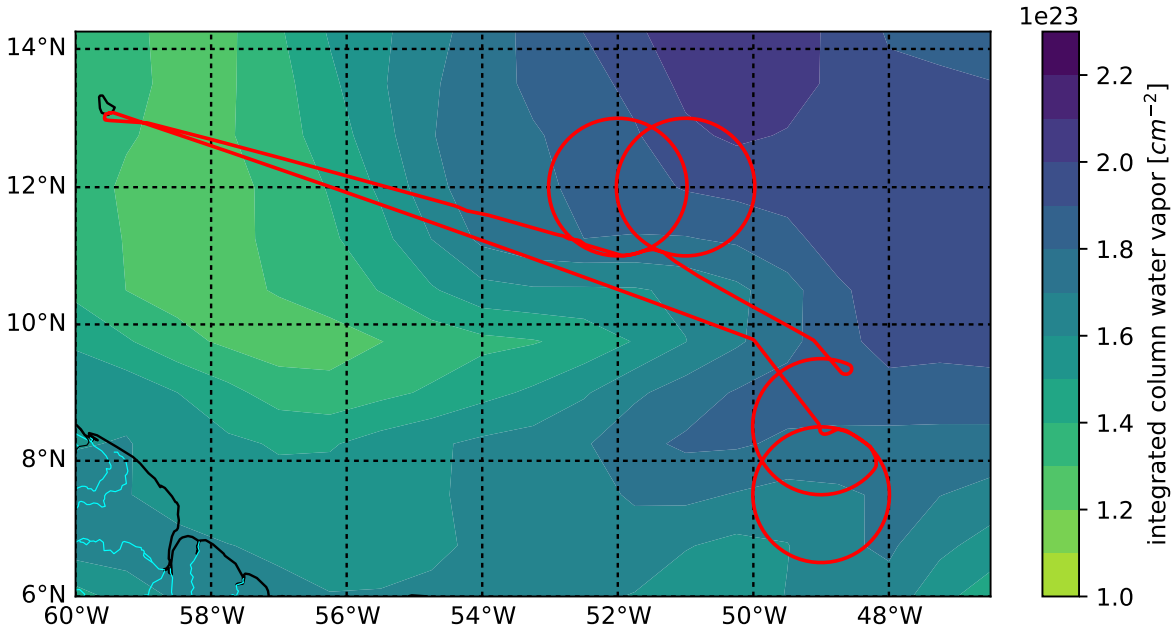

Figure 3.13: Integrated column water vapor number density between 0 and 10 km for reasearch flight 7. Water vapor concentration was calculated from ECMWF ERA-Interim data (Dee et al., 2011) from 12 UTC reanalysis on 22. August 2016. The red line indicates the flight track of the HALO research aircraft.

against the integrated column water vapor number density between cloud top at 0.8 km and 10 km which was already mentioned to be a typical cruise altitude. This was done to relate the variation of the threshold to a single quantity describing the amount of water vapor.

Figure 3.14 shows the plot of the fit parameter x as a function of the integrated column water vapor concentration (blue dots). The distribution agrees well with a quadratic fit function (orange). The spread of the points is due to the dependence of absorption efficiency on temperature. Two profiles with equal amount of column water vapor can deviate in their absorption properties, because of a different vertical water vapor distribution. To adapt the threshold correctly, the quadratic fit needs to be normalized to 1 for an integrated water vapor equal to the reference scene, to keep the initial threshold unchanged. For the general form of the quadratic function depending on integrated water vapor (iwv)

$$g(iwv) = \alpha \cdot iwv^2 + \beta \cdot iwv + \gamma \tag{3.12}$$

where α, β and γ are the fit parameter, the normalization is achieved by recalculating the constant γ for the reference integrated water vapor iwv_{ref}

$$\begin{aligned} g(iwv_{ref}) = 1 &= \alpha_{fit} \cdot iwv_{ref}^2 + \beta_{fit} \cdot iwv_{ref} + \gamma_{new} \\ \gamma_{new} &= 1 - \alpha_{fit} \cdot iwv_{ref}^2 - \beta_{fit} \cdot iwv_{ref} \end{aligned} \tag{3.13}$$

Applying this normalization to the fit parameter yields the function:

$$\boxed{g(iwv) = -1.150 \cdot 10^{-47}\, iwv^2 + 7.682 \cdot 10^{-24}\, iwv + 0.5614} \tag{3.14}$$

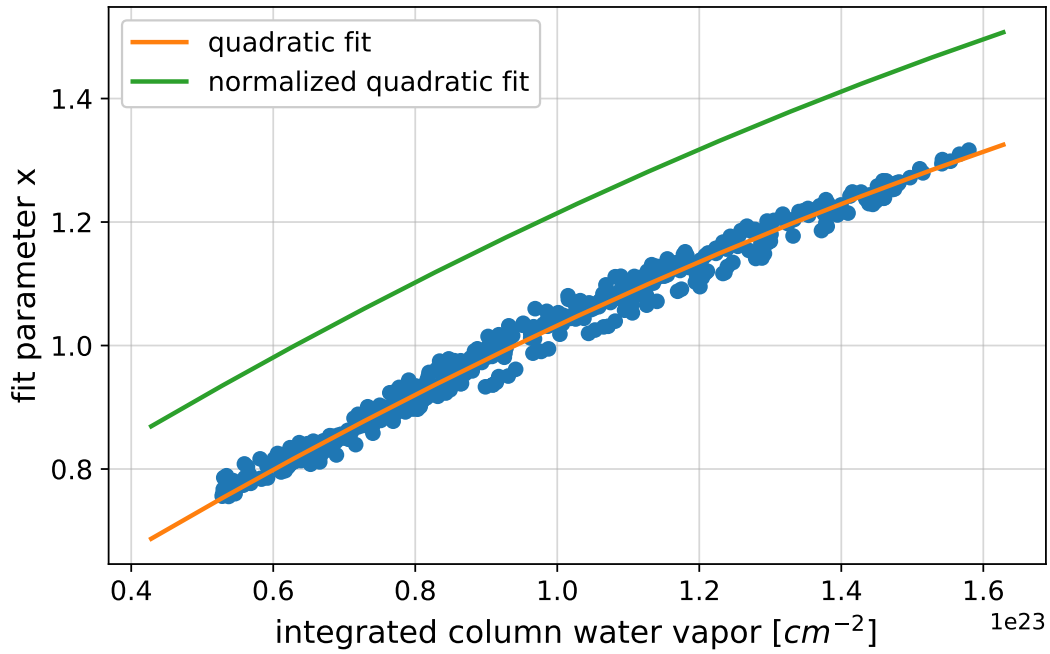

Figure 3.14: Simulated variation of the water vapor fit parameter x as a function of integrated column water vapor between 0.8 and 10 km. The orange curve shows a quadratic least square fit applied to the data. The fit function was normalized to the integrated water vapor of the scene used for threshold tuning ($0.6 \cdot 10^{23}$ cm^{-2}) (green curve)

which is represented by the green curve in figure 3.14. Now the adaptation has to be incorporated in the threshold calculation introduced in equation (3.8), as $x_{thres}(sza, vza)$ is now also a function of integrated water vapor concentration $g(iwv)$

$$x_{thres}(sza, vza, iwv) = \frac{1}{2}\left(\frac{1}{\cos(sza)} + \frac{1}{\cos(vza)}\right) \cdot g(iwv) \cdot x_{thres,std} \tag{3.15}$$

Abbreviating the viewing and sun geometry term on the right hand side of the equation by $f(sza, vza)$

$$f(sza, vza) = \frac{1}{2}\left(\frac{1}{\cos(sza)} + \frac{1}{\cos(vza)}\right) \tag{3.16}$$

the new relation for the cloud detection threshold reads

$$\boxed{x_{thres}(sza, vza, iwv) = f(sza, vza) \cdot g(iwv) \cdot x_{thres,std}} \tag{3.17}$$

Using this equation it is possible to receive a decent estimate of the threshold for variations of SZA, VZA as well as water vapor concentrations. Nevertheless the reanalysis data with low spatial and temporal resolution are may not precise enough in some situations. Therefore it is possible that if the water vapor concentration obtained by the model is

lower than in reality the threshold adaptation according to equation (3.14) is to weak and small clouds or cloud edges are not detected properly. The other possible error is an over estimation of the actual water vapor concentration, which can cause high false detection rates. Classifying clear pixels as cloudy is a more serious error than detecting less clouds than actually present, especially for deriving a cloud size distribution. Therefore, the focus is rather on reliably detecting cloudy pixels and accept to classify some cloudy pixels as clear sky, than taking the risk to eventually classify a large number of clear pixels as cloudy. This is achieved by slightly enhancing the tuned threshold in section 3.4.3 from 0.81 to 0.82.

3.4.7 Binary operations

Even if the threshold is chosen carefully there are certain situations where the the cloud mask fails. In these cases a large number of circumstances act together. It was observed that for some scenes with strong sunglint during research flight (RF) 6, a large number of pixels was classified as cloudy, although visual inspection did not reveal any evidence for the presence of clouds. The wrongly detected clouds were not larger than about two pixels and coincided with dark regions on the ocean's surface. These dark regions were due to high waves traveling perpendicular to the direction of the Sun's position, which caused a shading of the wave areas facing away from the sun. These areas are shown in figure 3.15. Some of these dark regions within the bright sunglint were not masked by the brightness or noise mask.

A possible explanation that these regions in were identified as cloudy by the water vapor cloud mask, is a high concentration of aerosol particles. Aerosols scatter short wave infrared radiation way more efficient than air molecules which has two effects. First, more radiation is scattered towards the camera than in a clean atmosphere which prevents the apparently dark pixels from being identified as "dark" by the noise or brightness mask. The second effect is that the scattered light received by the camera originates from regions way above the surface and has therefore an absorption signature similar to a cloud. Additionally, to high water vapor concentrations from the ECMWF data could contribute to this failure.

As several thousand of these small wrongly detected cloud pixels occur in the cloud mask this problem can not be ignored, especially as it has great influence on the cloud size distribution derived from the cloud mask. Therefore it was decided to apply a binary opening operation on the cloud mask with a 3x3 kernel. A opening is a erosion followed by a dilation. The erosion eliminates all clouds smaller than the kernel, which is in this case 3x3 pixel. As also larger clouds loose area by the erosion the subsequent dilation adds the previously lost pixels. For a mathematical definition of these operations see JI et al. (1989).

In the algorithm the binary opening is applied in the post processing after the the water vapor and the brightness cloud masks were merged according to the sunglint mask.

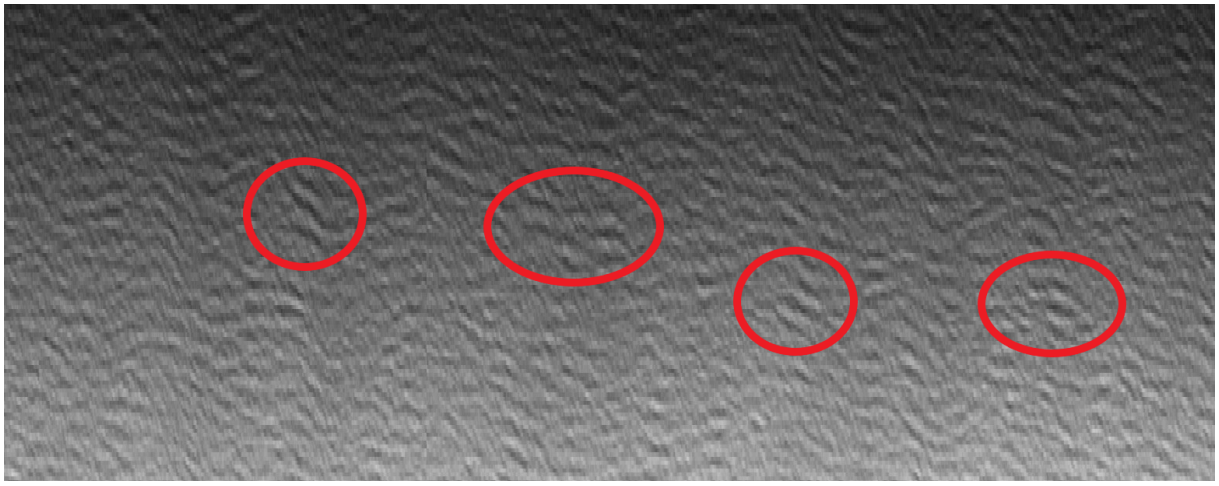

Figure 3.15: Detail of the 1600 nm radiance measured by the SWIR camera during research flight 6 at 16:30 UTC. Dark regions within the bright sunglint are indicated by red circles.

3.4.8 Cloud detection workflow

Figure 3.16 summarizes all the aspects of the cloud detection algorithm presented in the previous sections. It is divided in a center branch, which contains the fundamental steps to obtain the final cloud mask and two side branches, where additional input parameters and information about the procedures leading to consecutive results in the center branch is provided.

The processing starts with the raw data measured by the SWIR camera in form of digital numbers (DN) for each sensor pixel. In the calibration step the DN has to be translated to radiance. Thereby corrections for the dark signal (ds), the spectral transmittance of the window in front of the camera (wc), damaged sensor pixels (bp) and the exposure time of the camera (dt) are applied. To erase irregularities and obtain consistent fit result, the calibrated data are subsequently smoothed by a 3x3 Gaussian kernel. Now the least square fit of the reference spectrum is applied to the camera spectrum of each spatial pixel according to equation (3.4), which yields the fit parameter a, a measure for the brightness of the spectrum, and x, which provides information about the degree of absorption in the respective spectrum. From the fit parameter a the brightness cloud mask is derived applying a constant threshold of 0.62. This cloud mask, together with the noise mask, is used to exclude dark and noisy pixels from further processing in the water vapor cloud mask (masked x parameter).

To create the noise mask, the dark signal correction is applied to the raw data. From the dark corrected signal the signal-to-noise ratio (SNR) of the SWIR camera can be calculated according to equation (3.2). Subsequently, a threshold of 40 is applied to the average SNR for the spectral channels located on the flanks of the water vapor absorption bands (see section 3.4.4), which yields the noise mask. Now the masked results for the fit parameter x are used to create a second cloud mask. Therefore, the tuned standard threshold for $sza = vza = 0$ (0.82) is corrected for the SZA in each camera frame and

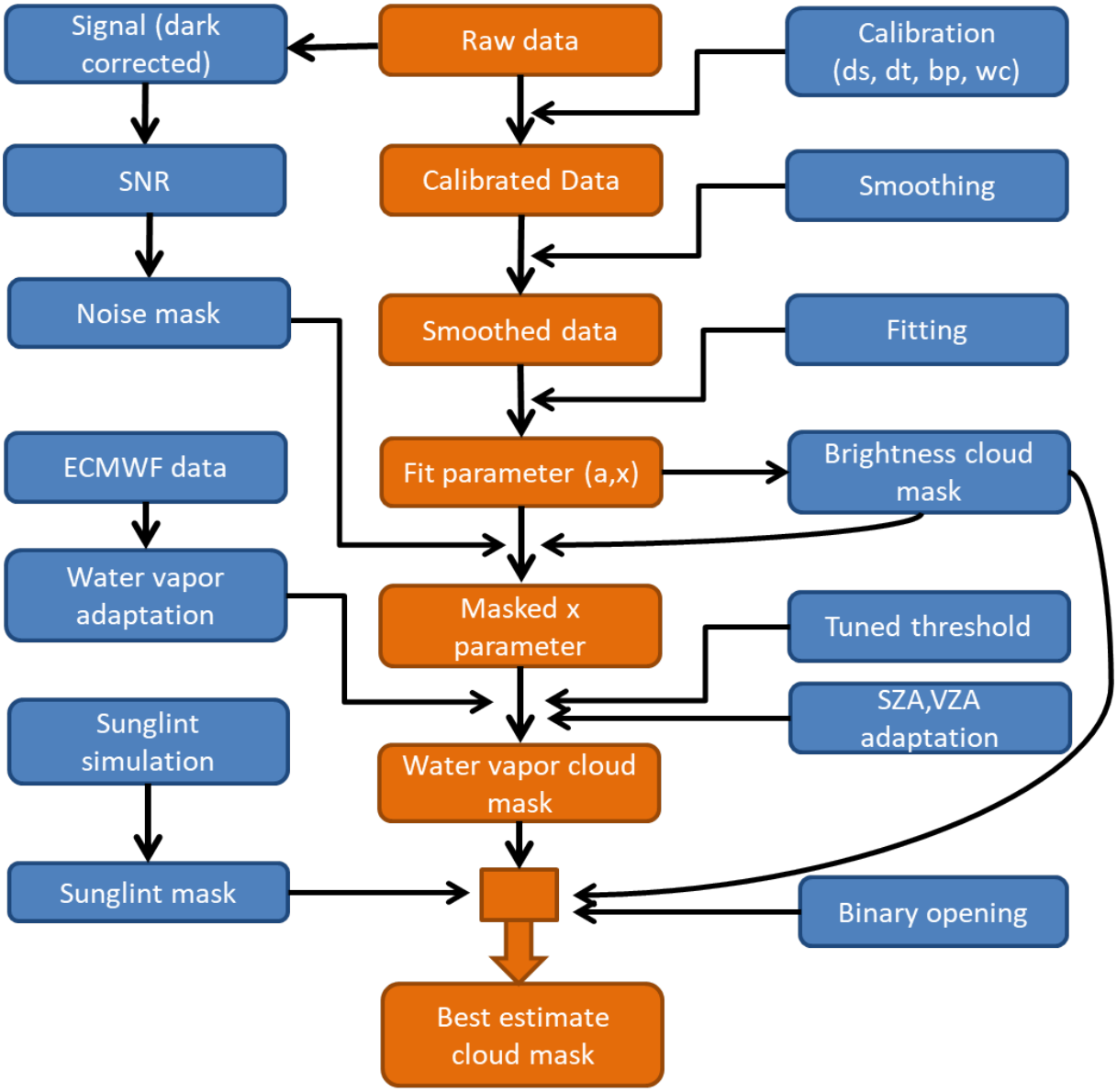

Figure 3.16: Sketch of the process steps and necessary ingredients of the combined water vapor absorption and brightness cloud mask.

the VZA for each pixel within the frame (see eq. 3.8). Additionally the water vapor adaptation factor for each frame is calculated. Thereby, the integrated column water vapor number density between 0.8 and 10 km is interpolated from ECMWF ERA-Interim reanalysis (Dee et al., 2011) for each frame (see section 3.4.6). The column water vapor is then plugged into the the fit function (3.14), which models the dependency of the tuned threshold on water vapor concentration and yields the needed adaptation factor. Applying these thresholds to each individual pixel gives the water vapor cloud mask.

In a last step the brightness and the water vapor cloud mask are merged according to a simulated sunglint mask. The sunglint is simulated by calculating the ocean's

reflectance for each pixel in every camera frame, assuming a wind speed of 5 ms^{-1}. A reflectance threshold of 0.005 is then applied to discriminate between sunglint contaminated and dark surface (see section 3.4.5). For bright frames the water vapor cloud mask is preferred, whereas in dark regions the brightness cloud mask is chosen. Finally a binary opening is applied to eliminate eventually false detected cloud pixels (see section 3.4.7).

The result of all these steps is the best estimate for the cloud mask derived from the SWIR camera data. From this cloud mask other quantities like cloud fraction or a cloud size distribution can be derived.

3.5 Treatment of corrupt data

The data captured by specMACS during NARVAL II sometimes suffer from problems like window icing and missing dark signal measurements. When the aircraft was flying at high altitudes with cold temperatures, the water vapor in the housing of the specMACS instrument froze onto the window of the housing. Therefore, these data have to be rejected. It also happened that the control software of the instrument missed to measure the dark signal of the sensor, when the camera settings changed. If no dark signal measurement is available for a specific setup, these data can not be calibrated and also have to be rejected.

Currently these corrupt data have to be found by visual inspection and excluded manually as no automatic algorithm exists, which is able to detect these errors at present.

3.6 Cloud fraction

From the cloud mask, derived using the previously described method, the cloud fraction can be calculated for defined scenes or whole research flights (RFs). The cloud fraction was calculated taking the fraction of cloudy pixels divided by the number of all pixels. This approach is a standard method for deriving cloud fraction and is commonly used for satellite data (see section 2.3.2). One aspect, which is not explicitly considered in this approach, is the difference in pixel size between pixels pointing vertically downward and those at viewing zenith angles (VZA) larger than zero degree. This variation is neglected for two reasons: First, at larger VZA it is more probable to observe cloud sides rather than cloud tops. Therefore, a weighting of pixels according to their size would introduce an error if cloud sides are observed instead of the clear sky behind the cloud tower (see figure 2.17). The second and more important reason is that – assuming that clouds are randomly distributed over different VZAs – the error averages out to some extent. If clouds would always be located in the center of the camera image (low VZA) or always on the edges (high VZA), which is not observed in the data, the error might become significant.

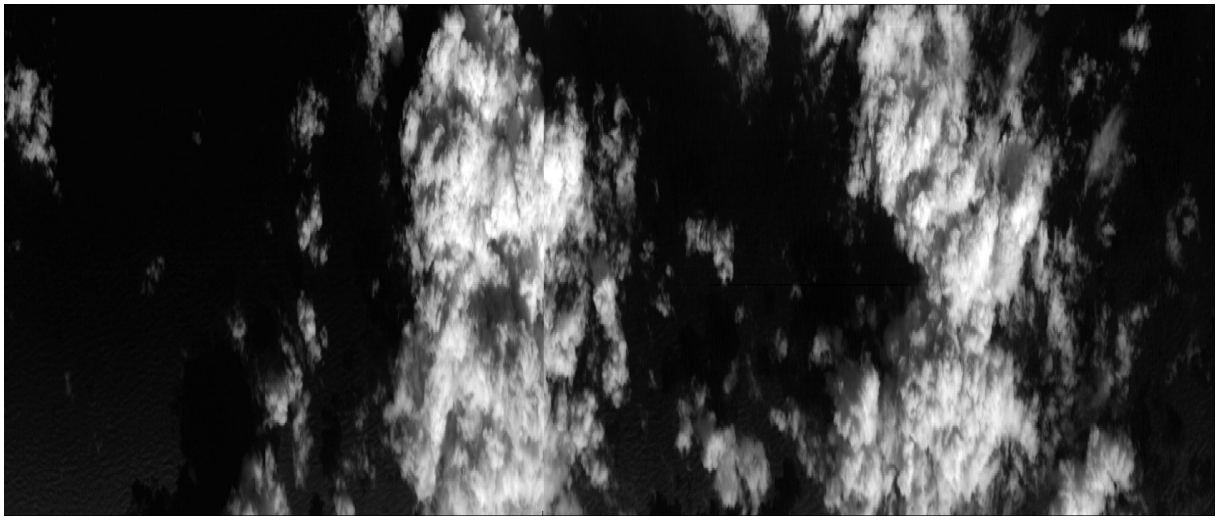

Figure 3.17: Image captured by the SWIR camera from 18:11-18:13 UTC during research flight 6. The measured radiance at 1600 nm is shown.

3.7 Cloud size distribution

From the cloud mask obtained by the approach described in the previous sections, it is now possible to derive the cloud size distribution. In this section the method used to derive the along-track cloud size distribution will be described in detail. The reason why only the along-track size distribution is considered, is that the entire extension of large clouds can only be captured in the along-track direction. The field of view (FOV) in the across-track direction of the specMACS instruments amounts about 6.4 km for a cruise altitude of 10 km. This fact causes two major problems. First, the maximum cloud size in the across-track direction is limited by the FOV, which means that no clouds larger than about 6.4 km can be detected at all. Second, clouds of this size can only be detected if they are perfectly centered within the FOV otherwise they are cut off. Following the results of Zhao and Di Girolamo (2007), shallow cumulus clouds of this size are the ones occurring most infrequent, which leads to a significant undersampling of the largest clouds if they are not properly detected and results in bad statistics. This problem is shown in figure 3.17. The two large clouds in the scene are cut off by the limited FOV in across-track direction but their extension in the along-track direction is captured properly.

During the NARVAL II campaign, the SWIR camera was operated with a constant frame rate of 30 Hz. For a typical cruise speed of the HALO aircraft of 200 ms^{-1} the horizontal distance between two consecutive camera frames amounts 6.7 m. The along-track FOV of 1.8 $mrad$ corresponds to a pixel size of 18 m assuming a cruise altitude of 10 km. Therefore, the pixel size is larger by nearly a factor of 3 compared to the horizontal distance of consecutive frames. This leads to a strong overlap of the FOV of consecutive frames. Therefore, the along-track pixel size is rather determined by frame rate and aircraft speed, than by the along-track FOV of the camera. Hence, the size of clouds can be determined independently of assumptions over the distance between the observed cloud and the aircraft, which would be necessary to determine the pixel size corresponding

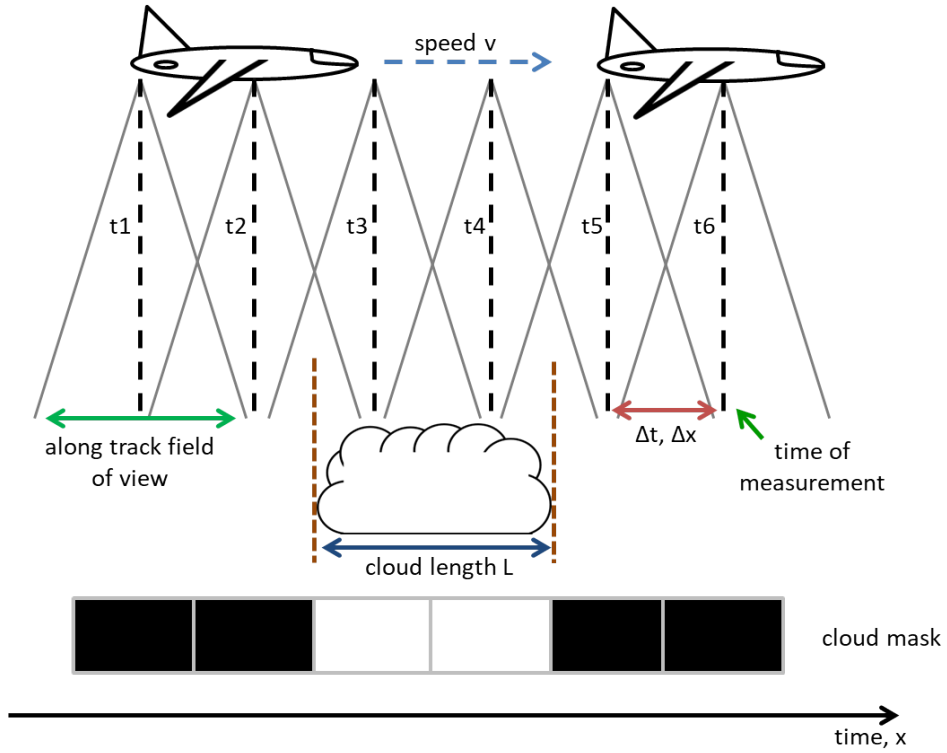

Figure 3.18: Sketch of a SWIR camera measurement time series along the flight track. Vertical dashed lines (black) indicate the time and location a measurement took place, the diverging gay lines show the field of view (FOV) of the camera. The black and white boxes represent a possible cloud mask for the sketched scene.

to its FOV. The situation sketched in figure 3.18 nicely shows the previously described overlap of the along-track FOV indicated by the slant gray lines. The black dashed lines in the vertical, denote the time the measurement took place, which corresponds to the time-stamp of each frame. As the aircraft moves at speed v, the time between consecutive frames Δt corresponds to a distance $\Delta x = v\Delta t$. The observed cloud of length L fills the two consecutive FOVs (t_3, t_4) to a large extent. Therefore, these pixels are labeled cloudy in the cloud mask. The neighboring FOVs (t_2, t_5) are only slightly covered by the cloud edges and are not detected as cloudy. In a first approximation the length of the cloud can be estimated to $L = v(t_5 - t_4) = v\Delta t_{5,4}$. Actually, the cloud is larger, which can be seen in the figure. To account for this, it is assumed that each cloud extends to about half the distance to the previous and following non-cloudy pixel, which is indicated by the vertical dashed lines on the cloud edges in figure 3.18. This might not be true for all clouds but this approximation is closer to the real cloud size, as the first approximation systematically underestimates the cloud length. Compared to the errors introduced by the cloud detection itself, this uncertainty in the cloud size is small, especially for large clouds. Furthermore, this assumption will not influence the slope of the derived cloud size distribution as long as it is applied consistently, because it has the same effect like

a change of the threshold (compare section 2.2.5). Applying this now to the discussed example reads:

$$L = v \left(\frac{t_4 - t_3}{2} + t_5 - t_4 + \frac{t_6 - t_5}{2} \right) \tag{3.18}$$

To give a more general formulation for the calculation of the along-track cloud length, variations of the aircraft speed have to be taken into account. Therefore, v is replaced by the mean speed $\bar{v}$ of the aircraft while it crosses the cloud. Additionally, the time-stamp of the first cloudy pixel is denoted by t_{in} and the one of the last cloudy pixel by t_{end}, where *in* and *end* are the corresponding indices of the time array. Using these definitions, gives the general form of the cloud length calculation:

$$L = \bar{v} \left(\frac{t_{in} - t_{in-1}}{2} + t_{end} - t_{in} + \frac{t_{end+1} - t_{end}}{2} \right) \tag{3.19}$$

This equation also works in the case of single pixel clouds, which are assumed to be of the same extent like two consecutive camera frames.

Equation (3.19) depends on the first and last time index of each cloud, wherefore they have to be extracted from the cloud mask. This is done using the ndimage.measurements module from SciPy Python library. All clouds in the cloud mask are labeled, before the time index of the first and last cloudy pixel of each cloud is extracted. The average speed of HALO for the time indices of each cloud, is calculated using the ground speed data from the BAHAMAS instrument. From the time indices and the average aircraft speed the cloud length can be calculated according to equation (3.19).

To derive a cloud size distribution, the clouds are binned with intervals of 200 m. The number of clouds in each bin is then plotted in a histogram. Additionally, a power law fit according to equation (2.17) is applied, whereby the frequency in each bin is assigned to the center size of each bin. To obtain better statistics and avoid undersampling of large clouds, the cloud size distributions of research flights 3 and 6 are merged.

3.8 Validation

A great challenge for all kinds of retrieval methods applied to measurement data is, to assess the quality of the results. For cloud detection methods it is important that only cloudy pixels are labeled as such and that the cloud fraction estimated from the retrieved cloud mask agrees well with the "true" cloud fraction. As there is no truth available for measurement data, the only possibility to estimate the quality of retrievals is to apply them to model data, where the measured and retrieved quantities are known.

To investigate the performance of the cloud detection algorithm developed in this thesis, a cloud field from a large eddy simulation (LES) was used as a input for 3D radiative transfer simulations with MYSTIC (Monte carlo code for the physically correct tracing of photons in cloudy atmospheres) (Mayer, B., 2009). MYSTIC was used to realistically simulate a measurement with the SWIR camera mounted on an aircraft and observing the ocean and clouds below from an altitude of 10 km. Therefore, the simulation is as close as possible to the real measurement situation during NARVAL II. Simulations were

carried out for different sunglint situations (varying wind speed) and solar zenith angles to obtain information about the methods performance under various conditions. The LES as well as the radiative transfer simulations with MYSTIC were performed by Fabian Jakub. Further information on MYSTIC and the exact model setup can be found in section 3.3 and in table 6.4 in the appendix.

Before the cloud detection algorithm was applied, the spectra simulated with MYSTIC were convolved with the spectral response function (slit function) of the SWIR camera (see section 3.3.2). The signal-to-noise ratio (SNR) of the SWIR camera is a quantity characteristic for this specific instrument and can not be calculated from the model output. Therefore, the noise mask derived from the SNR of the SWIR camera is excluded from the cloud detection. The binary opening operation was introduced in the retrieval, to reduce errors due to high aerosol concentrations and inaccurate water vapor data derived from the ECMWF reanalysis (see section 3.4.7). As the validation is intended to assess the general performance of the cloud detection method, given the necessary parameters are known, the binary opening is also not applied to the model scenes. The integrated water vapor for the MYSTIC simulations was calculated from the used atmosphere file, the viewing zenith angles and the solar zenith angle were also taken from the model input. These are required input parameter for the calculation of the threshold according to equation (3.17).

The cloud mask derived using the water vapor approach, was compared to the cloud mask from the liquid water path (LWP) of the LES output with a threshold of LWP > 0 gcm^{-2}, which serves as a benchmark. The quality of the cloud mask obtained by the water vapor approach, is evaluated by comparing it to the benchmark cloud mask.

4 Results

In this chapter the performance of the developed cloud detection algorithm is investigated. The results for the validation data set is discussed quantitatively, whereas the performance on measurement data can only be assessed qualitatively as the truth is unknown. Hereafter, the cloud detection algorithm is also referred to as water vapor cloud mask or water vapor algorithm.

4.1 Validation

For the simulated validation data, a cloud mask was derived by applying a threshold to the liquid water path (LWP) from the large eddy simulation (LES). The threshold was set to LWP > 0, which means that each pixel, which contains any amount of liquid water is classified as cloudy. This benchmark cloud mask is compared to the cloud masks derived by the water vapor algorithm for varying wind speed and solar zenith angle.

The first comparison is shown in figure 4.1. Here the simulation with a solar zenith angle (SZA) of 10° and a wind speed of 5 ms^{-1} is compared to the benchmark cloud mask. The upper panel shows the simulated radiance at a wavelength of 1600 nm, the bottom panel the corresponding water vapor cloud mask. The image in the center depicts the LWP cloud mask, which has a cloud fraction 24.55%. This value is 1.1% larger, than the cloud fraction of the water vapor cloud mask with 23.45%. Red circles in the center image indicate regions where the two cloud masks differ. The difference is due to optically thin edge pixels, which can barely be seen by eye in the radiance image. Most of the cloud pixels, which were not detected by the water vapor cloud mask, are located in the lower part of the image, where the sunglint is strongest. Therefore, they are illuminated by light reflected on the ocean's surface, which results in higher water vapor absorption, as the measured light is a superposition of light reflected on top of the cloud and light reflected on the surface. Beside the discrepancy for edge pixels, the two cloud masks agree well.

4.1.1 Variation of the solar zenith angle

To examine the influence of variations in solar zenith angle, the above described simulation was performed with a SZA of 30° and same wind speed. The simulated radiance and the water vapor cloud mask for this simulation are shown in figure 4.2. As the sun's azimuth is 180° (points towards the bottom of the page) only a small strip of sunglint can be identified on the lower boundary of the radiance image. Nevertheless, the surface is too bright to use a brightness cloud mask. The cloud fraction for the water vapor cloud mask in this scene is 21.7%, which is 2.85% below the benchmark LWP cloud mask and 1.75%

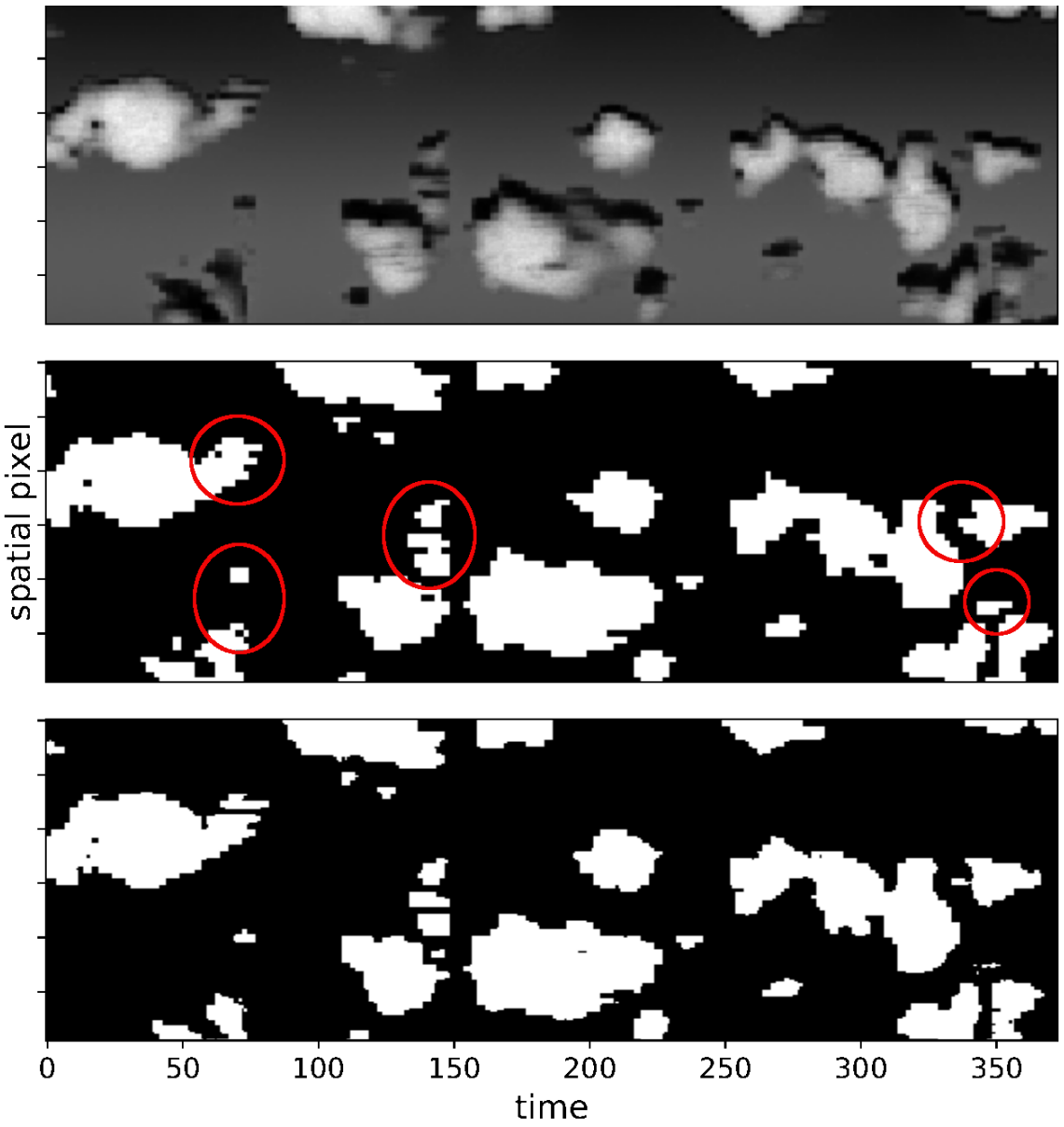

Figure 4.1: Cloud mask of simulated validation scene for a solar zenith angle (SZA) of 10° and a wind speed of 5 ms^{-1}. Upper panel: simulated radiance at 1600 nm. Center panel: cloud mask derived from LES liquid water path (LWP) with a threshold of LWP > 0 $g\,cm^{-2}$ and a cloud fraction of 24.55%. Bottom panel: cloud mask derived by the water vapor algorithm with a cloud fraction of 23.45%. Red circles indicate regions, where the LWP cloud mask detects more clouds than the water vapor cloud mask.

less than for the simulation with a SZA of 10°. To identify the differences in the water vapor cloud masks due to the SZA variation, the contours of the cloud mask for SZA = 10° (orange) is plotted onto the SZA = 30° cloud mask in figure 4.2.

Two features can be observed comparing the two cloud mask. The first one is, that

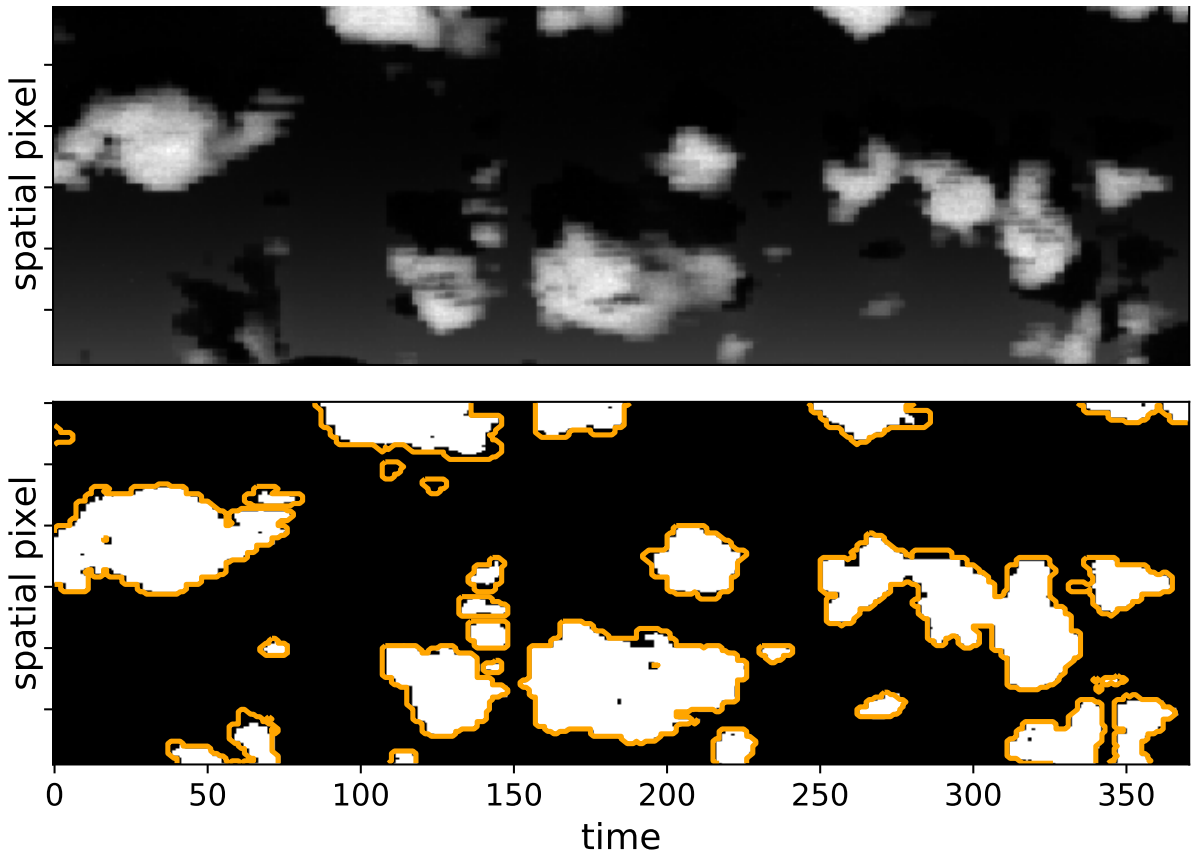

Figure 4.2: Cloud mask of simulated validation scene for a solar zenith angle of 30° and a wind speed of 5 ms^{-1}. Upper panel: simulated radiance at 1600 nm. Bottom panel: cloud mask derived by the water vapor algorithm with a cloud fraction of 21.7%. Orange contours indicate the water vapor cloud mask for a SZA of 10° and a wind speed of 5 ms^{-1}.

on the cloud sides facing away from the sun, less cloudy pixels are detected for the larger SZA. These regions are shaded by the higher cloud tops in the center of the clouds. In the previous chapter it was already mentioned, that these 3D effects enhance the absorption because of multiple scattering. The threshold adaptation according to equation (3.8), is based on 1D considerations and does not account for such 3D effects. The second feature can be identified in the upper part of the cloud mask. Here also the edge pixels on the cloud side facing towards the sun get lost for larger SZA. Especially the two small clouds on the upper left side disappear completely. The major cause of this cloud mask failure is the brightness mask. Looking at the radiance image the clouds are considerably darker for the SZA of 30° than for 10°. Therefore, they do not surpass the constant brightness threshold and are labeled non-cloudy.

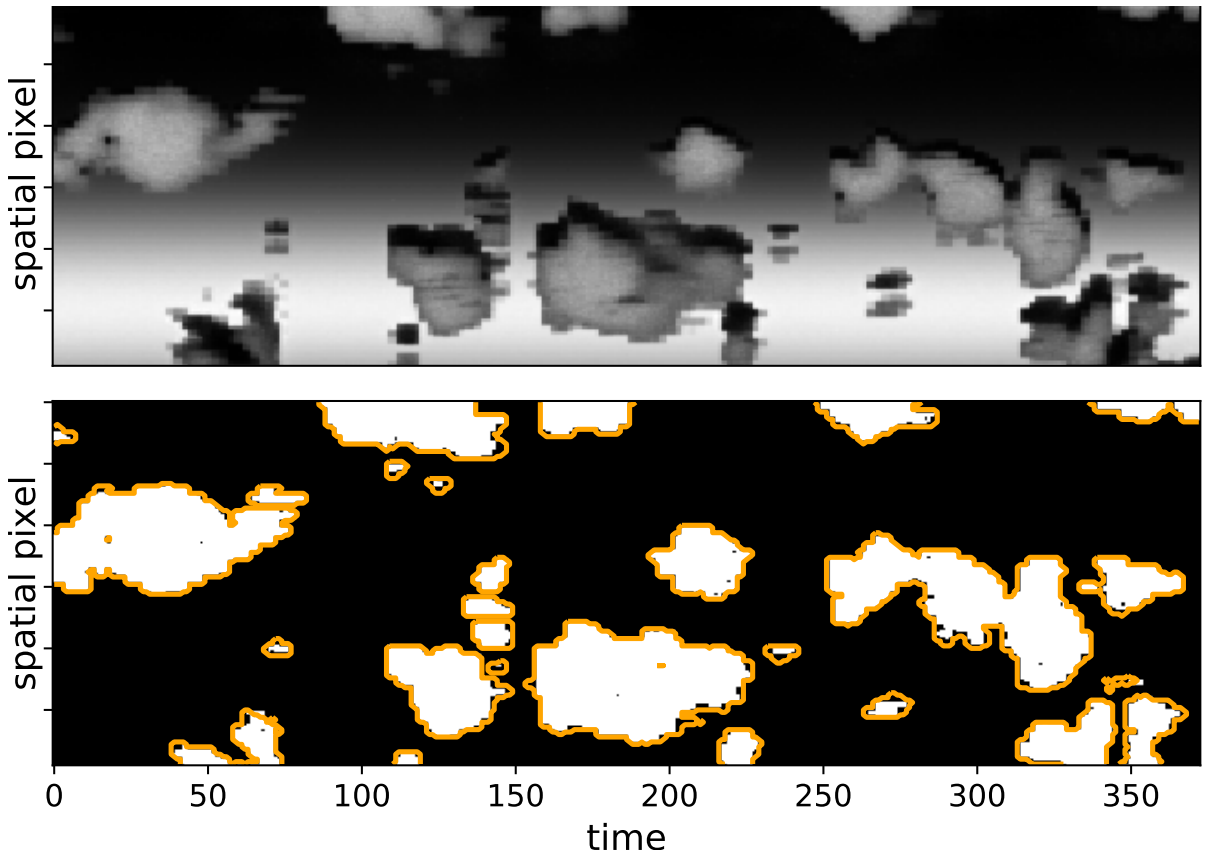

Figure 4.3: Cloud mask of simulated validation scene for a solar zenith angle of 10° and a wind speed of 1 ms^{-1}. Upper panel: simulated radiance at 1600 nm. Bottom panel: cloud mask derived by the water vapor algorithm with a cloud fraction of 22.37%. Orange contours indicate the water vapor cloud mask for a SZA of 10° and a wind speed of 5 ms^{-1}.

4.1.2 Variation of wind speed

The wind speed significantly influences the ocean's reflectance (see figure 2.7). For low wind speeds the sunglint is brighter and has a smaller spatial extent. This may has influences the performance of the water vapor cloud mask. Therefore, a simulation for a SZA of 10° an a wind speed of 1 ms^{-1} was conducted, which is shown in figure 4.3. The very bright strip of the sunglint can nicely be seen in the simulated radiance image in the upper panel of the figure. Here, the clouds are rather dark features in front of a bright background than vice versa. But also in this complex situation, the water vapor cloud mask performs well with a cloud fraction of 22.37%. Compared to the simulation for same SZA, but a wind speed of 5 ms^{-1}, – shown as orange contours as before – cloudy edge pixels right above the sunglint are not detected. This feature can also be referred to the light, which is reflected on the surface and penetrates the optically thin cloud pixels from below and thereby enhances the measured absorption.

4.1.3 Discussion

The examination of the water vapor cloud mask shows an overall good agreement with the cloud fraction of the benchmark cloud mask. The loss in accuracy for larger SZA can possibly be reduced by parameterizing the 3D effects in the threshold adaptation and adapt the brightness threshold according to the solar zenith angle. Another possible source of error originates from the assumption, that water vapor absorption above the cruise altitude of the aircraft can be neglected. This works for small SZA, but becomes more inaccurate for larger SZA. This problem could be solved by weighting the SZA adaptation higher than the VZA adaptation and do not weight them equally by a factor of 0.5, as shown in equation (3.8).

The loss of optically thin cloud pixels for small wind speeds can not be improved, but shows the limitation of the method itself and the instruments accuracy. The water vapor absorption signature of these pixels is to close to the one of clear sky pixels to be distinguished. A question, which was already asked by Di Girolamo and Davies (1997) and which is still unresolved, is how the true cloud fraction is actually defined? As there is no definition, also the benchmark cloud mask with a LWP threshold value of zero could be inaccurate, because one droplet in the entire atmospheric column might not be called a cloud. If the LWP threshold is for example set to 0.67 gcm^{-2} the cloud fraction is the same like for the simulation with a SZA of 10° and a wind speed of 5 ms^{-1}. With this in mind the validation of the water vapor cloud mask was successful.

4.2 Performance on measurement data

In contrast to the previously described model data, the performance of the water vapor cloud mask on measurement data, can only be assessed by visual inspection. Figure 4.4 shows a sunglint affected scene captured by the SWIR camera during research flight (RF) 6. In the upper panel the measured radiance at a wavelength of 1600 nm is shown, the center image depicts the corresponding water vapor cloud mask. In the bottom panel the contours of the cloud mask (orange) are plotted onto the camera image for better comparison.

The large and optically thick clouds are well detected by the algorithm over both, bright sunglint and dark ocean surface. In the center and on the left side, the smaller and darker clouds, which are not surrounded by the cloud mask contours stand out. These clouds appear to be very close to the surface and are optically thin. Some of the clouds could maybe be detected, if the the threshold for the water vapor cloud mask was set lower, but due to the coarsely resolved and at times not perfectly accurate ECMWF reanalysis water vapor information, this would cause failure of the cloud mask in other scenes. Additionally, clouds smaller than 3x3 pixel were removed by the binary opening operation. The smallest and thinnest clouds though, suffer from the problem of transmitted light which was reflected on the surface, as already described in the previous section. To overcome this problem, the cloud masks as well as the instruments accuracy would need to be improved.

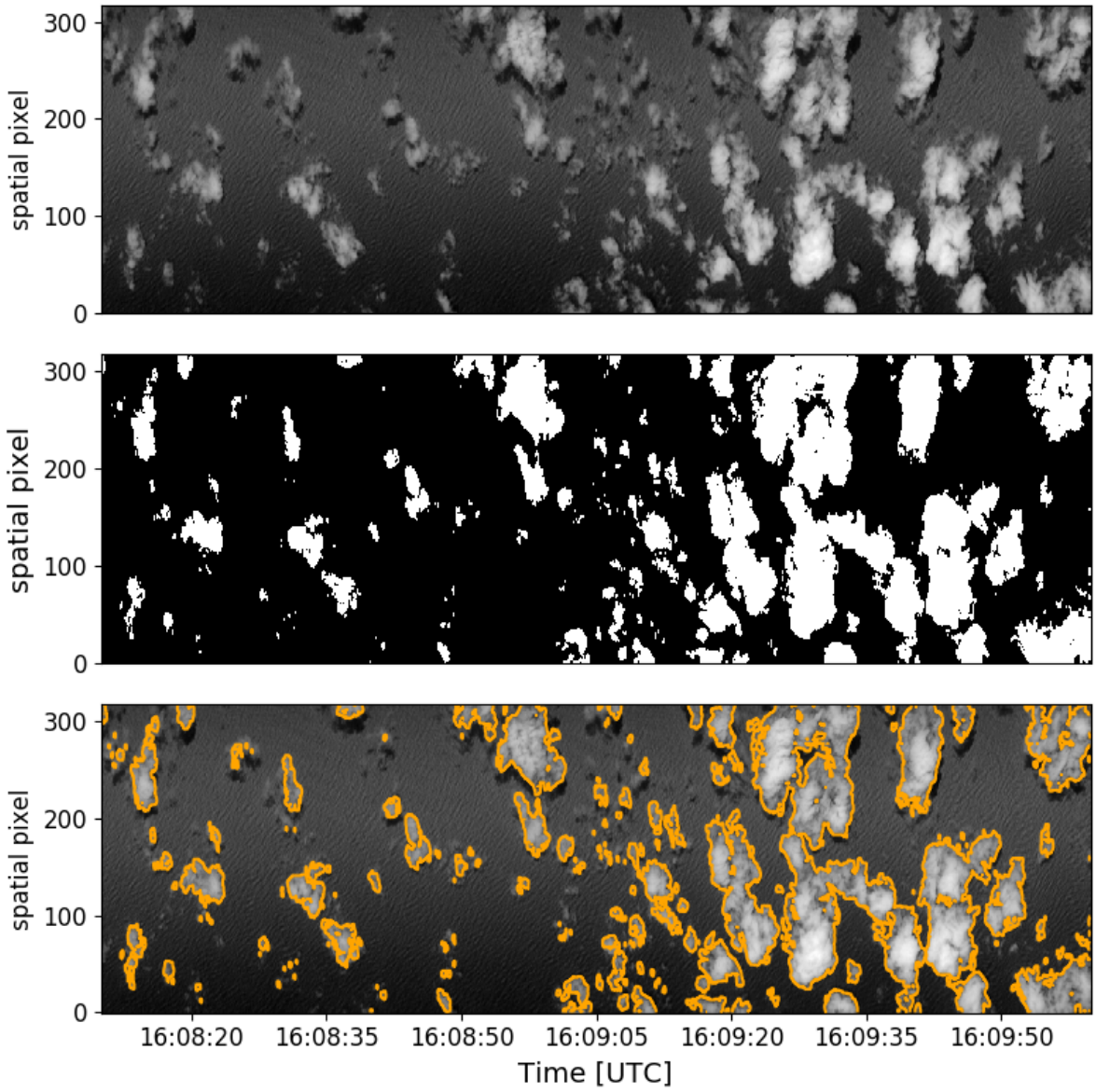

Figure 4.4: Cloud mask for a scene during research flight 6 at 16:09 UTC. Upper panel: SWIR camera image of measured radiance at 1600 *nm*. Center panel: cloud mask derived by the water vapor algorithm with a cloud fraction of 22.34%. Bottom panel: contours of the cloud mask mapped onto the SWIR camera image.

During RF7 the meteorological situation was significantly different. As already shown in figure 3.13, the water vapor concentration was nearly twice the one during RF6. Furthermore, the cloud structures were more complex. Shallow cumulus clouds were obscured by mid-level stratus cloud fields and high cirrus clouds. Such a multi-layer cloud scene is shown in figure 4.5. A large fraction of the scene is covered by high cirrus clouds,

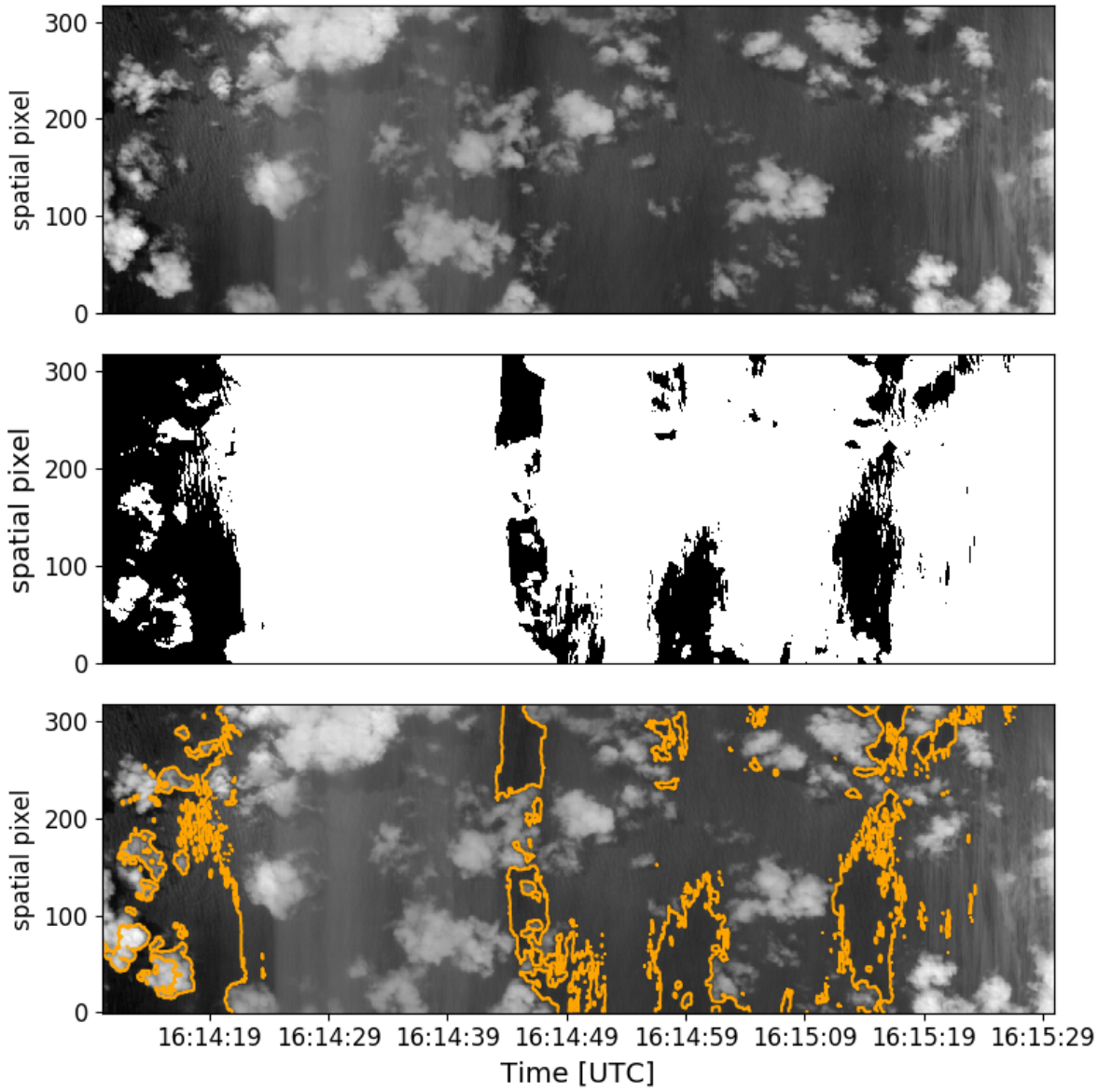

Figure 4.5: Cloud mask for a scene during research flight 7 at 16:14 UTC. Upper panel: SWIR camera image of measured radiance at 1600 *nm*. Center panel: cloud mask derived by the water vapor algorithm with a cloud fraction of 79.06%. Bottom panel: contours of the cloud mask mapped onto the SWIR camera image.

which are thin enough to see the shallow cumulus clouds below. For these cirrus clouds the water vapor cloud mask works excellent, because the water vapor absorption is very small. On the left edge of the camera image a small area without cirrus clouds can be identified. The shallow cumulus clouds in this region are not detected accurately. This can have many causes. The presence of cirrus clouds enhances the amount of diffuse solar

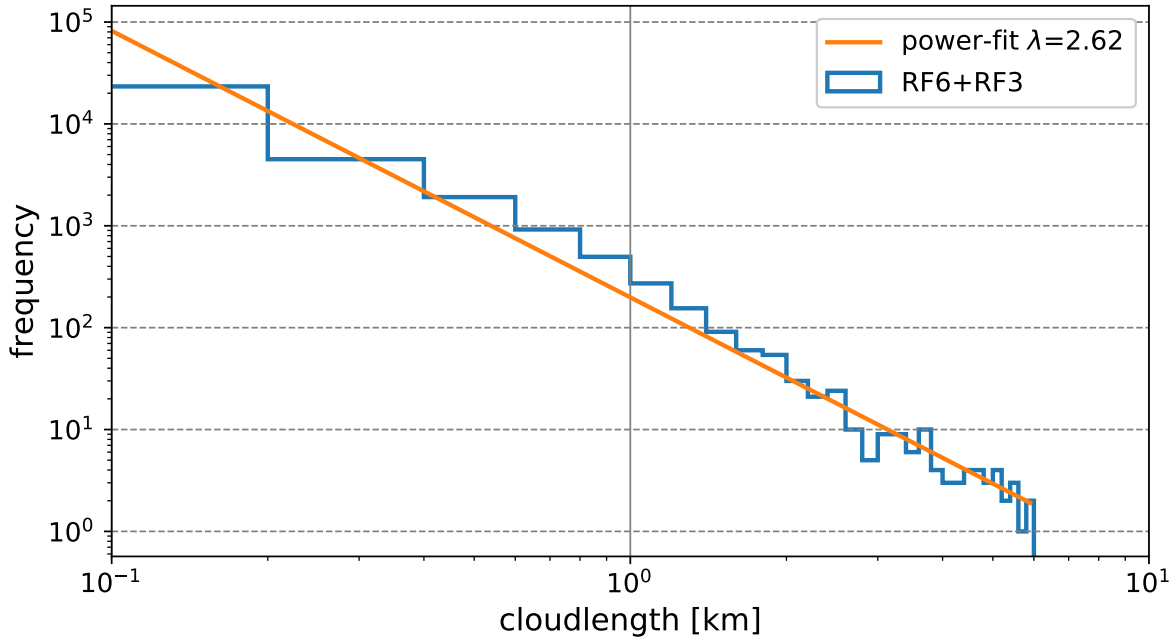

Figure 4.6: Histogram of along-track cloud size distribution combing results for research flights 3 and 6 (RF3, RF6). A bin-width of 200 m was used for all clouds smaller than 7 km. A power-law was fitted according to equation (2.17) yielding an exponent of $\lambda = 2.62$.

radiation, which increases the light path and therefore the absorption. Additionally, the flight track of RF7 was close to deep convection of the ITCZ. For this reason it is likely, that the water vapor concentrations derived from the ECMWF data were to low, due to the coarse resolution in space and time. Such complex cloud scenes are not of high value for remote sensing retrievals, because no reasonable conclusions can be drawn from the cloud fraction or cloud size distribution of a mixture of cirrus and shallow cumulus clouds. Therefore, inaccuracies in the cloud mask are of minor importance.

4.2.1 Discussion

The two scenes from RF6 and RF7 show the two to typical regimes encountered during NARVAL II campaign. Shallow cumulus convection in the trade wind region with similar meteorological conditions throughout a whole research flight and the highly variable and complex cloud structures in the vicinity of deep convective clouds. For these complex cloud scenes the algorithm shows inaccuracies, which are due to diffuse radiation caused by thin cirrus clouds and insufficient knowledge about the water vapor concentrations in the vicinity of deep convection. For shallow cumulus cases the water vapor cloud detection algorithm reveals good performance, which can also be seen in figure 6.1 in the appendix, depicting a scene during RF3. Even if the very low and optically thin cumulus clouds could not be detected this cloud mask gives the possibility to estimate representative values for cloud fraction and cloud size distribution.

4.3 Cloud size distribution

The cloud mask investigated in the previous sections can be used to derive a cloud size distribution. The method used to derive the cloud size distribution from the SWIR camera cloud mask, is described in section 3.7. Figure 4.6 shows the along-track cloud size distribution derived from a combined data set of RF3 and RF6, which both represent a shallow cumulus regime. The data were merged to obtain more accurate statitics and avoid undersampling of large clouds. Fitting a power law according to equation (2.17) yields a exponent of $\lambda = 2.62$. Furthermore, a scale break as described by Zhao and Di Girolamo (2007) can be found. For clouds smaller than about 1 km the slope of the size distribution is smaller than for larger clouds. This cloud size distribution can serve as a validation quantity for model studies of shallow cumulus convection.

4.3.1 Discussion

The cloud size distribution derived from RF3 and RF6 show good agreeement with the results of Zhao and Di Girolamo (2007), who found values for the fit paramter λ between 2.58 and 3.55 in the tropical western Atlantic. The statistics cloud be improved by adding cloud size distributions from other research flights.

5 Summary and outlook

In this thesis a cloud detection algorithm was developed, which uses the absorption by water vapor in the short wave infrared solar spectrum (SWIR) to identify clouds in the presence of sunglint. The algorithm was applied to data collected by the SWIR camera of the hyperspectral imager specMACS during NARVAL II measurement campaign. To extract the information about water vapor absorption from measured spectra, two reference spectra were calculated using the 1D DISORT solver from libRadtran (Mayer and Kylling, 2005): one with was calculated with and one without molecular absorption. The reference spectrum without absorption multiplied by the derived reference transmittance, was then fitted to each camera spectrum, after they were convolved with the spectral response function of the instrument. Thereby, the fit parameter a scales the brightness of the spectrum and the fit parameter x exponentially scales the reference transmittance and contains information about water vapor absorption. Subsequently thresholds for both parameters were derived. The threshold for x is scaled according to the solar zenith angle (SZA), the viewing zenith angle (VZA) and the actual abundance of water vapor, which was derived from ECMWF ERA-Interim reanalysis (Dee et al., 2011). The sensitivity of the threshold to water vapor concentration was determined by radiative transfer simulations. Cloud masks from both parameters were combined together with a noise mask obtained by applying a threshold to the signal-to-noise ratio of the SWIR camera. For larger SZA the camera frames are not affected by sunglint and the brightness cloud mask from fit parameter a yields better results. Therefore, simulations of the ocean's reflectance were conducted to derive a sunglint mask. According to the sunglint mask, the different cloud masks are merged to obtain the best estimate for the cloud mask. In a final step, a binary opening operation was applied to remove clear sky pixels, which were wrongly classified as cloudy.

The validation of the algorithm with model data reveals good performance. For a SZA of 10° and wind speed of 5 ms^{-1} the cloud fraction derived from the cloud mask of the water vapor approach is 23.45% and therefore only slightly below the benchmark cloud fraction of 24.55% derived from model data. For higher SZA the water vapor cloud mask loses accuracy due to shading effects on cloud edges, which enhances the water vapor absorption due to multiple scattering. The cloud fraction for a SZA of 30° and a wind speed of 5 ms^{-1} is 21.7% and therefore lower than for the SZA of 10°. For smaller wind speeds the sunglint becomes brighter and illuminates cloud edges from below. As the measured signal is a superposition of light reflected on the cloud and light reflected on the ocean's surface, which is subsequently transmitted through the cloud, the water vapor absorption for these pixels becomes larger and they are not detected as cloudy. Therefore, the cloud fraction reduces for a SZA of 10° and wind speed of 1 ms^{-1} compared to the simulation with same SZA but higher wind speed (5 ms^{-1}) to 22.37%. The performance

on measurement data also yields positive results, showing the same limitations found for the simulated measurement data. Additional inaccuracies arise from uncertainties in water vapor concentrations derived from ECMWF reanalysis data and high aerosol concentrations.

Even if the presented cloud detection algorithm shows a over all good performance, small improvements can still be made. Furthermore, the derived cloud mask can be used in future studies. Some ideas about the possibilities in this context are given in the following.

The loss in cloud mask performance for larger SZA can have two reasons. Shaded cloud regions, where the water vapor absorption is enhanced by multiple scattering and water vapor absorption above the the cruise altitude of the aircraft, which becomes too large to be neglected when the SZA rises. The shading effect could be parameterized for the threshold adaptation to some extent using 3D radiative transfer simulations to get an estimate for the magnitude of this effect. The water vapor absorption above the aircraft could also be considered by assigning a higher weight to the SZA adaptation in the threshold calculation. The weighting factor can be estimated using radiative transfer simulations. Another possibility to generate a more accurate threshold for the fit parameter x could be the use statistical techniques. In a histogram analysis of all x-values for a scene, a better threshold could be estimated. The uncertainty in water vapor concentrations derived from ECMWF reanalysis could reduced using additional information from the WALES LIDAR or dropsonde profiles, which both measure vertically resolved water vapor profiles. Beside the improvements in the threshold determination, the water vapor fit parameter could be used to derive cloud top heights. The higher the cloud, the smaller the absorption. For this purpose, multidimensional look-up-tables would need to be calculated. Another improvement could be made with respect to the computational time needed for the calculation of the cloud mask, by reducing the number of wavelengths considered in the least square fit. Thereby, it should be evaluated if the cloud mask is still accurate, when less wavelengths are used.

This thesis pointed out repeatedly, that the absence of a true cloud fraction for measurement data is a great issue. Additionally, the cloud mask derived for a specific instrument also depends on its sensitivity towards clouds, the spatial and temporal resolution, and the method used to detect the clouds. All these components act together and can lead to completely different results for different instruments. This high discrepancy was observed in the cloud fraction derived from the remote sensing instruments operated during NARVAL II. Therefore, it is important to investigate and understand how much and in which way parameters like resolution and instrument sensitivity influence the result of the cloud detection process. A first attempt in this field was made by Sabrina Pavicic in her Bachelor thesis, where the cloud mask derived from the SWIR camera is compared to LIDAR, Microwave Radiometer and the SMART instrument. There are still a lot of unresolved questions in the field of cloud detection, but at least one was answered in this thesis: it is possible to detect shallow cumulus clouds in the presence of sunglint using absorption by water vapor.

6 Appendix

6.1 Setups for libRadtran simulations

6.1.1 1D DISORT

The cloud detection algorithm developed in this thesis makes use of radiative transfer calculations with the library for radiative transfer (libRadtran) (Mayer and Kylling, 2005). Furthermore some figures presented in chapter 2 were created with the help of libRadtran simulations. Therefore all setups for the individual calculations are listed here in tabulated form.

Setup LWCRE	
solver	DISORT (Stamnes et al., 1988; Buras et al., 2011)
atmosphere	US standard atmosphere (afglus.dat) (Anderson et al., 1986)
molecular absorption	correlated-k, 12 bands, Fu and Liou (1992)
wavelength	3.7 μm - 70 μm
aerosol	default
sensor altitude	top of atmosphere (TOA)
viewing zenith angle (VZA)	0°
optical cloud properties	default (Hu and Stamnes, 1993)
cloud liquid water content (LWC)	1 $g\,m^{-3}$
cloud effective radius (r_{eff})	10 μm
cloud height above surface	1-2 km/ 4-5 km/ 7-8 km

Table 6.1: Setup for calculation of the longwave cloud radiative effect depending on the altitude of the cloud (see section 2.2.4).

Setup Reference Spectra	
solver	DISORT (Stamnes et al., 1988; Buras et al., 2011)
atmosphere	tropical standard atmosphere (afglt.dat) (Anderson et al., 1986)
molecular absorption	REPTRAN/no molecular absorption
resolution	coarse: $\Delta\tilde{\nu} = 15\ cm^{-1}$ ($\Delta\lambda =$ 1.5-9.5 nm for used wavelengths)
wavelength	1000 - 2500 nm
aerosol	default
sensor altitude	10 km
surface properties	ocean BRDF (Cox and Munk, 1954)
solar zenith angle (SZA)	0°
viewing zenith angle (VZA)	0°
optical cloud properties	default (Hu and Stamnes, 1993)
cloud liquid water content (LWC)	0.1 $g\,m^{-3}$
cloud effective radius (r_{eff})	10 μm
cloud height above surface	600 - 800 m

Table 6.2: Setup for calculation of reference spectra for water vapor cloud retrival (see section 3.4.2).

Setup Water Vapor Adaptation	
solver	DISORT (Stamnes et al., 1988; Buras et al., 2011)
atmosphere	tropical standard atmosphere (afglt.dat) with modified water vapor from ECMWF data (Dee et al., 2011; Anderson et al., 1986)
molecular absorption	REPTRAN/no molecular absorption
resolution	coarse: $\Delta\tilde{\nu} = 15\ cm^{-1}$ ($\Delta\lambda =$ 1.5-9.5 nm for used wavelengths)
wavelength	1000 - 2500 nm
aerosol	default
sensor altitude	10 km
surface properties	ocean BRDF (Cox and Munk, 1954)
solar zenith angle (SZA)	0°
viewing zenith angle (VZA)	0°
optical cloud properties	default (Hu and Stamnes, 1993)
cloud liquid water content (LWC)	1 $g\,m^{-3}$
cloud effective radius (r_{eff})	10 μm
cloud height above surface	600 - 800 m

Table 6.3: Setup for calculation of spectra for different water vapor concentrations to model threshold adaptation (see section 3.4.6).

6.1.2 3D MYSTIC

?? The scenes used for the validation of the cloud detection algorithm were performed with the 3D radiative transfer solver MYSTIC (Mayer, B., 2009). The specific options used for the simulation of these scenes are listed in the table below.

Setup Water Vapor Adaptation	
solver	MYSTIC (Mayer, B., 2009)
atmosphere	tropical standard atmosphere (afglt.dat) (Anderson et al., 1986)
molecular absorption	REPTRAN
resolution	medium: $\Delta\tilde{\nu} = 5\ cm^{-1}$ ($\Delta\lambda =$ 0.5-2 nm for used wavelengths)
wavelength	1000 - 2000 nm
aerosol	default
sensor altitude	10 km
surface properties	ocean BRDF (Cox and Munk, 1954)
solar zenith angle (SZA)	10°, 30°
viewing zenith angle (VZA)	±15°
optical cloud properties	interpolate mie
cloud liquid water content (LWC)	LES ouput
cloud effective radius (r_{eff})	LES output
photos per grid box	1000
further options	`mc_spectral_is 1500`, `mc_backward 0 0 149 0`, `mc_vroom on`, `mc_sensorposition 10 0 10000`, `mc_sample_grid 150 1 [] []`, `mc_panorama distr_photons_over_pixel`, `mc_panorama_view -15 15 90 90`, `mc_panorama_alignment mu`

Table 6.4: Setup for simulation of the validation scene conducted by Fabian Jakub (see section 3.8).

6.2 Additional results

6.2.1 Cloud mask example for RF3

To show that the cloud mask performs well for shallow cumulus environments in other research flights than RF6 a scene captured during RF3 is depicted in figure 6.1.

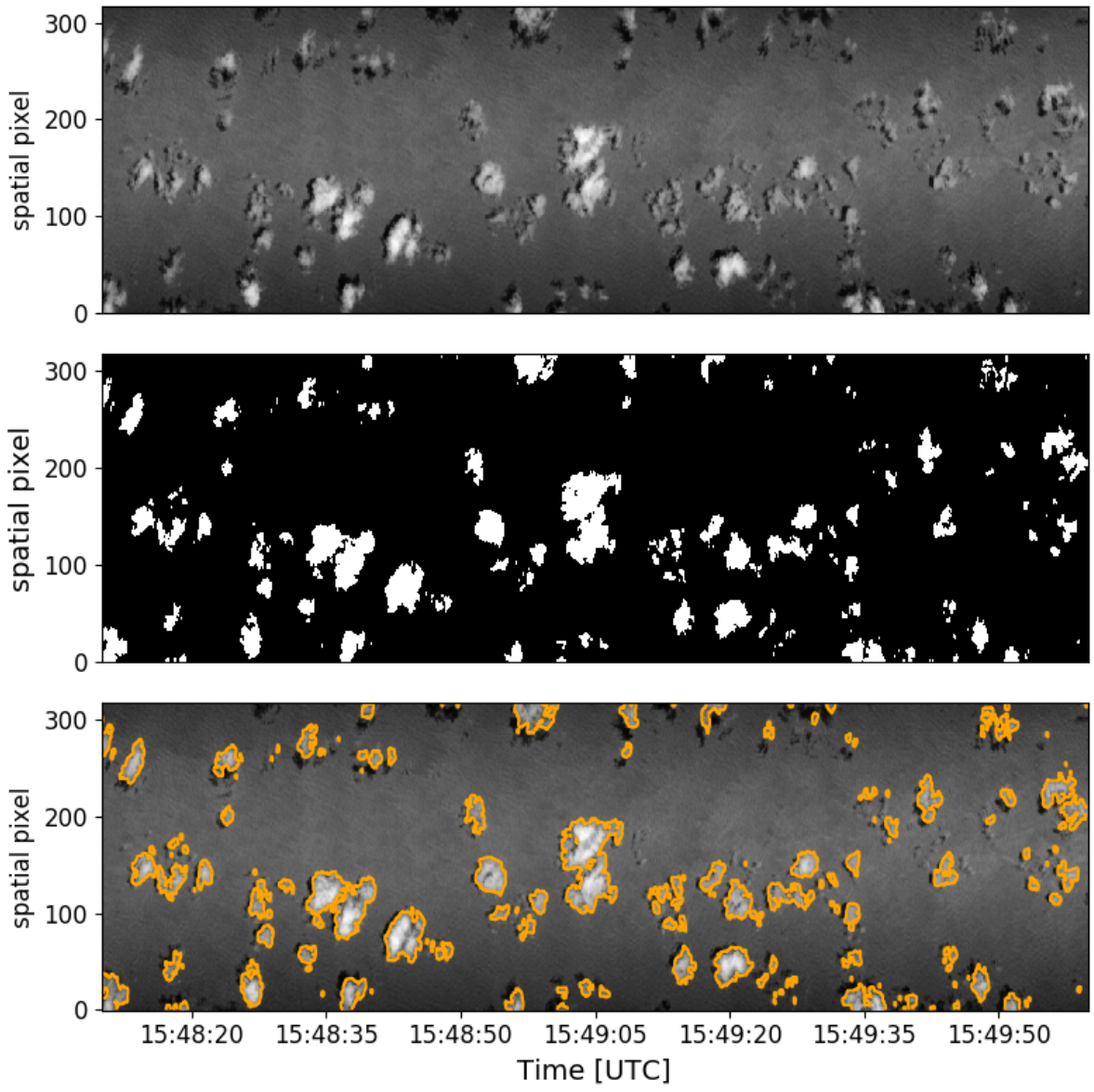

Figure 6.1: Cloud mask for a scene during research flight 3 at 15:49 UTC. Upper panel: SWIR camera image of measured radiance at 1600 nm. Center panel: cloud mask derived by the water vapor algorithm with a cloud fraction of 8.71%. Bottom panel: contours of the cloud mask mapped onto the SWIR camera image.

7 Acknowledgements

Zunächst möchte ich mich sehr herzlich bei Herrn Prof. Mayer bedanken, der bei Fragen immer zur Verfügung stand und es mir ermöglicht hat diese Arbeit über einen Monat später abzugeben, damit ich sie noch zu einem hoffentlich erfreulichen Ende bringen konnte. Einen großen Dank auch an Tobias Kölling, der vermutlich einer der schlausten Köpfe ist die mir je begegnet sind und mich mit seinem programmier-Fähigkeiten, seinem physilaisch-mathematischem und seinem technischen Verständnis immer wieder sehr unterstützt hat. Ein besonderer Dank geht natürlich an Carolin Klinger und Pascal Polonik, die so nett waren und diese Arbeit Korrektur gelesen haben. Vielen Dank auch an Fabian Jakub der die Modellrechungen zur Algorithmus Validierung durchgeführt hat.

Zum Schluss möchte ich mich noch bei allen bedanken die mir während dieser Arbeit und auch während dem Rest meines Studiums stehts mir Rat und Tat zur Seite gestanden sind.

Bibliography

Anderson, G., Clough, S., Kneizys, F., Chetwynd, J., and Shettle, E. (1986). AFGL Atmospheric Constituent Profiles (0-120 km). Technical Report AFGL-TR-86-0110, AFGL (OPI), Hanscom AFB, MA 01736.

Buras, R., Dowling, T., and Emde, C. (2011). New secondary-scattering correction in DISORT with increased efficiency for forward scattering. *Journal of Quantitative Spectroscopy and Radiative Transfer*, 112(12):2028–2034.

Chandrasekhar, S. (1950). Radiative transfer. clarendon.

Chen, T., Rossow, W. B., and Zhang, Y. (2000). Radiative effects of cloud-type variations. *Journal of climate*, 13(1):264–286.

Coakley, J. A. and Bretherton, F. P. (1982). Cloud cover from high-resolution scanner data: Detecting and allowing for partially filled fields of view. *Journal of Geophysical Research: Oceans*, 87(C7):4917–4932.

Cox, C. and Munk, W. (1954). Measurement of the roughness of the sea surface from photographs of the sun's glitter. *JOSA*, 44(11):838–850.

Dee, D. P., Uppala, S. M., Simmons, A. J., Berrisford, P., Poli, P., Kobayashi, S., Andrae, U., Balmaseda, M. A., Balsamo, G., Bauer, P., Bechtold, P., Beljaars, A. C. M., van de Berg, L., Bidlot, J., Bormann, N., Delsol, C., Dragani, R., Fuentes, M., Geer, A. J., Haimberger, L., Healy, S. B., Hersbach, H., Hólm, E. V., Isaksen, L., Kållberg, P., Köhler, M., Matricardi, M., McNally, A. P., Monge-Sanz, B. M., Morcrette, J.-J., Park, B.-K., Peubey, C., de Rosnay, P., Tavolato, C., Thépaut, J.-N., and Vitart, F. (2011). The era-interim reanalysis: configuration and performance of the data assimilation system. *Quarterly Journal of the Royal Meteorological Society*, 137(656):553–597.

Derrien, M. and Le Gléau, H. (2005). Msg/seviri cloud mask and type from safnwc. *International Journal of Remote Sensing*, 26(21):4707–4732.

Desbois, M., Seze, G., and Szejwach, G. (1982). Automatic classification of clouds on meteosat imagery: Application to high-level clouds. *Journal of Applied Meteorology*, 21(3):401–412.

Di Girolamo, L. and Davies, R. (1997). Cloud fraction errors caused by finite resolution measurements. *Journal of Geophysical Research: Atmospheres*, 102(D2):1739–1756.

Diday E., S. J. (1976). Clustering analysis. In Fu, K. S., editor, *Digital Pattern Recognition*, volume 10 of *Communication and Cybernetics*, chapter 3, pages 47–94. Springer, Berlin, Heidelberg.

Ewald, F., Kölling, T., Baumgartner, A., Zinner, T., and Mayer, B. (2016). Design and characterization of specmacs, a multipurpose hyperspectral cloud and sky imager. *Atmospheric Measurement Techniques*, (5):2015–2042.

Ewald, F., Zinner, T., and Mayer, B. (2013). Remote sensing of particle size profiles from cloud sides: Observables and retrievals in a 3d environment. In *AIP Conference Proceedings*, volume 1531, pages 83–86. AIP.

Fu, Q. and Liou, K. (1992). On the correlated k-distribution method for radiative transfer in nonhomogeneous atmospheres. *Journal of the Atmospheric Sciences*, 49:2139–2156.

Gao, B.-C. and Kaufman, Y. J. (1995). Selection of the 1.375-μm modis channel for remote sensing of cirrus clouds and stratospheric aerosols from space. *Journal of the atmospheric sciences*, 52(23):4231–4237.

Gödde, F. S. (2015). Einfluss thermischer strahlung auf das wachstum von wolkentröpfchen. Master's thesis, Ludwig-Maximilians-Universität Münchnen, Fakultät für Physik, Meteorologisches Institut.

Golaz, J.-C., Horowitz, L. W., and Levy, H. (2013). Cloud tuning in a coupled climate model: Impact on 20th century warming. *Geophysical Research Letters*, 40(10):2246–2251.

Goodman, A. and Henderson-Sellers, A. (1988). Cloud detection and analysis: A review of recent progress. *Atmospheric Research*, 21(3):203–228.

Gordon, I., Rothman, L., Hill, C., Kochanov, R., Tan, Y., Bernath, P., Birk, M., Boudon, V., Campargue, A., Chance, K., Drouin, B., Flaud, J.-M., Gamache, R., Hodges, J., Jacquemart, D., Perevalov, V., Perrin, A., Shine, K., Smith, M.-A., Tennyson, J., Toon, G., Tran, H., Tyuterev, V., Barbe, A., Császár, A., Devi, V., Furtenbacher, T., Harrison, J., Hartmann, J.-M., Jolly, A., Johnson, T., Karman, T., Kleiner, I., Kyuberis, A., Loos, J., Lyulin, O., Massie, S., Mikhailenko, S., Moazzen-Ahmadi, N., Müller, H., Naumenko, O., Nikitin, A., Polyansky, O., Rey, M., Rotger, M., Sharpe, S., Sung, K., Starikova, E., Tashkun, S., Auwera, J. V., Wagner, G., Wilzewski, J., Wcisło, P., Yu, S., and Zak, E. (2017). The hitran2016 molecular spectroscopic database. *Journal of Quantitative Spectroscopy and Radiative Transfer*, 203:3 – 69. HITRAN2016 Special Issue.

Henderson-Sellers, A. and McGuffie, K. (1990). Are cloud amounts estimated from satellite sensor and conventional surface-based observations related? *Remote Sensing*, 11(3):543–550.

Hu, Y. X. and Stamnes, K. (1993). An Accurate Parameterization of the Radiative Properties of Water Clouds Suitable for Use in Climate Models. *J. Climate*, 6(4):728–742.

JI, L., Piper, J., and Tang, J.-Y. (1989). Erosion and dilation of binary images by arbitrary structuring elements using interval coding. *Pattern Recognition Letters*, 9(3):201 – 209.

Köhler, H. (1936). The nucleus in and the growth of hygroscopic droplets. *Transactions of the Faraday Society*, 32:1152–1161.

Kopp, G. and Lean, J. L. (2011). A new, lower value of total solar irradiance: Evidence and climate significance. *Geophysical Research Letters*, 38(1).

Kurucz, R. (1992). Synthetic infrared spectra. In *Proceedings of the 154th Symposium of the International Astronomical Union (IAU), Tuscon, Arizona. Kluwer, Acad., Norwell, MA*, page 1365–1368.

Liou, K.-N. (2002). *An introduction to atmospheric radiation*, volume 84. Academic press.

Manolakis, D., Lockwood, R., and Cooley, T. (2016). *Hyperspectral Imaging Remote Sensing: Physics, Sensors, and Algorithms*. Cambridge University Press.

Marion, R., Michel, R., and Faye, C. (2004). Measuring trace gases in plumes from hyperspectral remotely sensed data. *IEEE transactions on geoscience and remote sensing*, 42(4):854–864.

Mayer, B. and Kylling, A. (2005). Technical note: The libRadtran software package for radiative transfer calculations - description and examples of use. *Atmospheric Chemistry and Physics*, 5(7):1855–1877.

Mayer, B. (2009). Radiative transfer in the cloudy atmosphere. *EPJ Web of Conferences*, 1:75–99.

Mie, G. (1908). Beiträge zur optik trüber medien, speziell kolloidaler metallösungen. *Annalen der physik*, 330(3):377–445.

Nakajima, T. and King, M. D. (1990). Determination of the optical thickness and effective particle radius of clouds from reflected solar radiation measurements. part i: Theory. *Journal of the atmospheric sciences*, 47(15):1878–1893.

NASA (2018). *New Zealand in Sunglint*. Image courtesy of the Earth Science and Remote Sensing Unit, NASA Johnson Space Center. Online; accessed 4 February 2018.

Planck, M. (1901). Ueber das Gesetz der Energieverteilung im Normalspectrum. *Annalen der physik*, 309(3):553–563.

Reynolds, D. W. and Vonder Haar, T. H. (1977). A bispectral method for cloud parameter determination. *Monthly Weather Review*, 105(4):446–457.

Rogers, R. (1975). *Short Course in Cloud Physics (Monographs in Natural Philosophy)*. Pergamon Press.

Rossow, W., Mosher, F., Kinsella, E., Arking, A., Desbois, M., Harrison, E., Minnis, P., Ruprecht, E., Seze, G., Simmer, C., et al. (1985). Isccp cloud algorithm intercomparison. *Journal of Climate and Applied Meteorology*, 24(9):877–903.

Segelstein, D. J. (1981). *The complex refractive index of water*. PhD thesis, University of Missouri–Kansas City.

Shante, V. K. and Kirkpatrick, S. (1971). An introduction to percolation theory. *Advances in Physics*, 20(85):325–357.

Siebesma, A. (1998). Shallow cumulus convection. In *Buoyant convection in geophysical flows*, page 441–486. Springer.

Siebesma, A. P., Bretherton, C. S., Brown, A., Chlond, A., Cuxart, J., Duynkerke, P. G., Jiang, H., Khairoutdinov, M., Lewellen, D., Moeng, C.-H., Sanchez, E., Stevens, B., and Stevens, D. E. (2003). A large eddy simulation intercomparison study of shallow cumulus convection. *Journal of the Atmospheric Sciences*, 60(10):1201–1219.

Simmer, C., Raschke, E., and Ruprecht, E. (1982). A method for determination of cloud properties from two-dimensional histograms. *Ann. Meteorol*, 18:130–132.

Snow, W., Bunting, J. T., d'Entremont, R. P., Grantham, D. D., Hardy, K. R., and Tomlinson, E. M. (1985). Space shuttle cloud photographs assist in correcting meteorological satellite data. *Eos, Transactions American Geophysical Union*, 66(24):489–490.

Stamnes, K., Tsay, S.-C., Wiscombe, W., Jayaweera, K., et al. (1988). Numerically stable algorithm for discrete-ordinate-method radiative transfer in multiple scattering and emitting layered media. *Applied optics*, 27(12):2502–2509.

Tiedtke, M. (1987). The parametrization of moist processes, part 2: The parametrization of cumulus convection. *ECMWF Lecture Series*.

Trenberth, K. E., Fasullo, J. T., and Kiehl, J. (2009). Earth's global energy budget. *Bulletin of the American Meteorological Society*, 90(3):311–323.

Tsang, L., Kong, J. A., and Shin, R. T. (1985). Theory of microwave remote sensing.

Wallace, J. M. and Hobbs, P. V. (2006). 10 - climate dynamics. In Wallace, J. M. and Hobbs, P. V., editors, *Atmospheric Science (Second Edition)*, pages 419 – 465. Academic Press, San Diego, second edition edition.

Windmiller, J. M. (2017). *Organization of Tropical Convection*. PhD thesis, Ludwig Maximilians Universität, München.

Zdunkowski, W., Trautmann, T., and Bott, A. (2007). *Radiation in the atmosphere: a course in theoretical meteorology*. Cambridge University Press.

Zhao, G. and Di Girolamo, L. (2007). Statistics on the macrophysical properties of trade wind cumuli over the tropical western atlantic. *Journal of Geophysical Research: Atmospheres*, 112(D10).

Erklärung

Ich erkläre hiermit, dass ich meine Masterarbeit mit dem Titel

Detecting Clouds in the Presence of Sunglint: An Approach Using Spectral Water Vapor Absorption

Wolkenerkennung im Sunglint mit Hilfe von Wasserdampfabsorption

selbstständig verfasst, sowie keine anderen als die angegebenen Quellen und Hilfsmittel benutzt habe.

München, den 5. Januar 2018

_____

(Felix Simon Gödde)